

Electronic Thesis and Dissertation Repository

12-16-2016 12:00 AM

Study of Mobile Robot Operations Related to Lunar Exploration

Matthew Cross, *The University of Western Ontario*

Supervisor: Kenneth McIsaac, *The University of Western Ontario*

A thesis submitted in partial fulfillment of the requirements for the Doctor of Philosophy degree
in Electrical and Computer Engineering

© Matthew Cross 2016

Follow this and additional works at: <https://ir.lib.uwo.ca/etd>



Part of the [Robotics Commons](#)

Recommended Citation

Cross, Matthew, "Study of Mobile Robot Operations Related to Lunar Exploration" (2016). *Electronic Thesis and Dissertation Repository*. 4331.

<https://ir.lib.uwo.ca/etd/4331>

This Dissertation/Thesis is brought to you for free and open access by Scholarship@Western. It has been accepted for inclusion in Electronic Thesis and Dissertation Repository by an authorized administrator of Scholarship@Western. For more information, please contact wlsadmin@uwo.ca.

Abstract

Mobile robots extend the reach of exploration in environments unsuitable, or unreachable, by humans. Far-reaching environments, such as the south lunar pole, exhibit lighting conditions that are challenging for optical imagery required for mobile robot navigation. Terrain conditions also impact the operation of mobile robots; distinguishing terrain types prior to physical contact can improve hazard avoidance.

This thesis presents the conclusions of a trade-off that uses the results from two studies related to operating mobile robots at the lunar south pole. The lunar south pole presents engineering design challenges for both tele-operation and lidar-based autonomous navigation in the context of a near-term, low-cost, short-duration lunar prospecting mission. The conclusion is that direct-drive tele-operation may result in improved science data return.

The first study is on demonstrating lidar reflectance intensity, and near-infrared spectroscopy, can improve terrain classification over optical imagery alone. Two classification techniques, Naive Bayes and multi-class SVM, were compared for classification errors. Eight terrain types, including aggregate, loose sand and compacted sand, are classified using wavelet-transformed optical images, and statistical values of lidar reflectance intensity. The addition of lidar reflectance intensity was shown to reduce classification errors for both classifiers. Four types of aggregate material are classified using statistical values of spectral reflectance. The addition of spectral reflectance was shown to reduce classification errors for both classifiers.

The second study is on human performance in tele-operating a mobile robot over time-delay and in lighting conditions analogous to the south lunar pole. Round-trip time delay between operator and mobile robot leads to an increase in time to turn the mobile robot around

obstacles or corners as operators tend to implement a ‘wait and see’ approach. A study on completion time for a cornering task through varying corridor widths shows that time-delayed performance fits a previously established cornering law, and that varying lighting conditions did not adversely affect human performance. The results of the cornering law are interpreted to quantify the additional time required to negotiate a corner under differing conditions, and this increase in time can be interpreted to be predictive when operating a mobile robot through a driving circuit.

Keywords: Mobile Robots, Tele-Operation, Fitts’ Law, Terrain Classification

For my Dad, who made pancakes at BC Hydro.

Acknowledgements

The work in this thesis could not have been completed without the financial support from NSERC PGS, Dr. Gordon Osinski's "Technologies and Techniques for Earth and Space Exploration" NSERC-CREATE program, and CANARIE.

I would first like to thank my supervisor and mentor Ken McIsaac for staying supportive through all of the ups and downs and 'crisis alerts'.

I would like to thank Peter Brown and Mike Debruyne for granting me access to the Elginfield Observatory, at which all of the data was collected. I would also like to thank Matt Bourassa, Will Choi, Shamus Duff, Taylor Haid, Justin Szoke-Sieswerda for their support and assistance with the various instruments and data collection.

This work could not have come together without the significant assistance from undergraduate students and volunteers. I would like to thank all of the students who worked on *LunaTron* and related projects over the years: Riley Bloomfield, Nicole Devos, Bryce Dudley, Daniel Horodniczy, Warren Moysey, Nick Reed, Andrew Simpson, Greg Thomas, and Emmett Wise. I would also like to thank the long list of volunteers who sat in a windowless room and remotely controlled the Husky at all hours of day and night, and for hours on end: Gareth Arnott, Lucas Brewster, Chris Briglio, Carolyn Cadogan, Eunice Chan, Matthew Davidson, Kelsey Doerksen, Raymond Francis, Jon Kissi-Ameyaw, Hilary Luo, Bobby Meagher, Lei Shu, Jai Sood, Haley Warshaw, Rob Wu, and Andrea Zagar.

The time spent on this work would have been a lot less enjoyable if not for colleagues and friends in ECE and CPSX.

And finally, I'd like to thank my family for their love and support through yet another

degree program.

Contents

Abstract	ii
Dedication	iv
Acknowledgements	v
List of Figures	xiii
List of Tables	xv
List of Abbreviations, Symbols, and Nomenclature	xxi
1 Introduction	1
1.1 Research Question	1
1.2 Motivation and Problem Statement	2
1.2.1 Abstraction of Problem Statement	3
1.3 Outline	5
2 A Short History of Planetary Exploration Rovers	6
2.1 Canadian Space Agency Activity	7
2.1.1 Mars Vehicles and CanMars	8
2.1.2 Lunar Vehicles and RESOLVE	10
2.2 Lunar Exploration Rovers	11
2.2.1 Prototypes and Mission Concepts for Lunar Exploration Rovers	12
2.3 Mars Exploration Rovers	18

2.4	Other Planetary Exploration Vehicles	20
3	Mobile Robot Terrain Traversability	22
3.1	Terramechanics	23
3.2	Traversability Prediction and Terrain Classification	26
3.2.1	Terramechanical Parameter Estimation	26
3.2.2	Wheel Sinkage Estimation	27
3.2.3	Slip Estimating	28
3.2.4	Proprioceptive and Exteroceptive Terrain Classification	29
3.3	Soil Inferencing and Proximal Soil Science	31
3.3.1	GIS and Mobile Robotics	33
3.4	Traversability on Other Planetary Surfaces	35
3.4.1	Mars Terrain Parameter Estimation	36
3.4.2	Lunar Regolith Parameters	37
4	Data Analysis and Classification	38
4.1	Wavelet Image Analysis	38
4.1.1	Haar Wavelet	38
4.1.2	Daubechies Wavelets	41
4.1.3	Two Dimensional Wavelet Transforms	42
4.2	Bayesian Probability	43
4.2.1	Frequentist Approach	46
4.2.2	Bayesian Approach	46
4.3	Classification	49
4.3.1	Naive Bayes Classification	50
4.4	Support Vector Machine classification	50
5	Human Performance in Tele-Operation	53
5.1	Tele-Operation	53

5.1.1	Earth-Based Applications	55
5.1.2	Space-Based Applications	57
5.2	Human Performance and Fitts' Law	57
5.2.1	Fitts' Law Formulation and HCI	57
5.2.2	Tele-Operation with Time Delay	60
5.2.3	Human Performance Studies and Mobile Robot Cornering	60
6	Terrain Classification	64
6.1	Experimental Equipment	64
6.1.1	Terrain Types and Terrain Box	65
6.1.2	The LunaTron Rover	67
6.1.3	Integrated Vision System	67
6.1.4	INO Hyperspectral Imager	69
6.2	Terrain Data Collection	70
6.3	Data Processing and Feature Vector Construction	70
6.3.1	Image Processing	71
6.3.2	Lidar Reflectance Intensity	72
6.3.3	Spectral Reflectance Features	76
6.3.4	Ensemble Feature Vectors	76
6.3.5	Data Comparison of Classifiers	77
6.3.6	<i>LunaTron</i> Data Feature Vectors	78
6.4	Results of Classification	78
6.4.1	Classifier Training with Matlab	78
	Classification of 8 Terrain Types	79
	Classification Between 4 Sand Types	79
	Classification Between 4 Aggregate Types	80
	Classification Between 3 Bulk Compositions	80
6.4.2	<i>LunaTron</i> Traversal Testing	81
6.5	Prediction Step	82

6.5.1	Aggragate to Loose Sand	82
6.5.2	Covered Aggregate to Flat Wet Sand	84
6.5.3	Gravel to Covered Aggregate	85
6.6	Discussion, Limitations, and Recommendations	87
7	Tele-Operation Over Time Delay	90
7.1	Experimental Equipment	91
7.1.1	The Robot Operating System	91
7.1.2	Husky A200 Mobile Robot	93
7.1.3	Tele-Operation User Interface	94
7.2	Outdoor Driving Course	95
7.2.1	Results	96
7.2.2	Interpretations of Results	101
7.3	Cornering Law Testing	101
7.3.1	Results	104
7.3.2	Cornering Law	105
	Interpretation and Comparison of Lighting Conditions	106
	Interpretation and Comparison of Time Delay	111
	Discussion	114
7.4	Limitations and Recommendations	115
8	Conclusions and Recommendations	118
8.1	Contributions	118
8.1.1	Terrain Classification	119
8.1.2	Tele-Operation Over Time Delay	119
8.1.3	Lunar South Pole Prospecting Operations Trade-Off	120
8.1.4	Summary of Contributions	120
8.2	Future Research Direction	121
8.2.1	Terrain Classification	121

8.2.2	Tele-Operation	122
Bibliography		124
A Comparison of Classification Confusion Matrices		139
A.1	Vehicle Data Classification	139
A.1.1	Aggregate vs Loose Sand vs Compact Sand	139
A.1.2	All 8 Classes	140
A.2	Classification of Aggregate and Sand Using Wavelet Transformed Images	141
A.2.1	Naive Bayes Classification	141
A.2.2	SVM Classification	142
A.3	Classification of Aggregate and Sand Using Image RGB Values	143
A.3.1	Naive Bayes Classification	143
A.3.2	SVM	144
A.4	Classification of Aggregate and Compact and Loose Sand Using Wavelet Transformed Images	145
A.4.1	Naive Bayes Classification	145
A.4.2	SVM Classification	146
A.5	Classification of Aggregate and Compact and Loose Sand Using RGB	147
A.5.1	Naive Bayes Classification	147
A.5.2	SVM Classification	148
A.6	Classification of Aggregates with Spectral Reflectance	149
A.6.1	Naive Bayes Classification	149
A.6.2	SVM Classification	151
A.7	Classification of Sands	153
A.7.1	Naive Bayes Classification	153
A.7.2	SVM Classification	154
A.8	Classification all Eight Terrain Types	155
A.8.1	Naive Bayes Classification	155

A.8.2 SVM	157
B Results of Cornering	159
B.1 Lighting Conditions	159
B.2 Time Delay	159
B.3 Blocks	162
Curriculum Vitae	167

List of Figures

2.1	<i>Kapvik</i> testing at CSA's Mars Yard	8
2.2	MESR at CSA's Mars Yard	10
2.3	<i>Scarab</i> rover	13
2.4	<i>Copernicus</i> was tele-operated by direct drive over 4 second time delay	14
2.5	Ames Research Center <i>K10</i>	15
2.6	<i>Opportunity</i> 's hazard identification camera image of embedded left-front wheel	20
3.1	The Mars Exploration Rover <i>Spirit</i>	23
3.2	Wheel-terrain contact model	25
3.3	An example of SINFERS	34
5.1	Teleoperation control scheme for remote manipulator	56
6.1	Terrain testing box	65
6.2	Terrain testing box at an incline	66
6.3	Integrated Vision System	68
6.4	RGB image acquired from IVS	71
6.5	Image strip of terrain class	71
6.6	Image patch for classifier training	72
6.7	Three strips of aggregate laying upon flattened wet sand in the terrain box	73
6.8	Visualization of reflectance intensity of aggregate strips	73
6.9	Flattened wet sand in the terrain box without the aggregate.	74
6.10	Visualization of reflectance intensity of flattened wet sand	74
6.11	Unprepared wet sand in the terrain box.	75

6.12	Visualization of reflectance intensity of unprepared wet sand	75
6.13	Traverse from aggregate to loose sand	84
6.14	Image strip featuring a transition from gravel to wet mixed sand.	84
6.15	Traverse from covered aggregate to flattened sand	85
6.16	Traverse from aggregate to covered aggregate	86
7.1	Tele-operation testing at Elginfield Observatory	92
7.2	The Husky A200 mobile robot shown outdoors for the tele-operation testing. . .	94
7.3	The user tele-operates the rover through an interface using a gamepad.	95
7.4	The tele-operated rover provides streaming video for the user.	96
7.5	180 <i>m</i> drive circuit	97
7.6	150 <i>m</i> complex drive circuit	98
7.7	Cornering through corridor apertures.	102
7.8	Cornering through corridors, shown with an aperture width of 95 <i>cm</i>	103
7.9	Cornering time versus ID without time delay	107
7.10	Cornering time versus ID with 2 second time delay	109
7.11	Cornering time versus ID with 4 second time delay	110
7.12	Cornering time versus ID with ambient lighting	111
7.13	Cornering time versus ID with bright spot light	112
7.14	Cornering time versus ID with headlights in darkness	113

List of Tables

2.1	Lunar Rovers and Prototypes Comparison	17
2.2	Computational capabilities of Mars rovers	18
3.1	Summary of proximal soil sensing techniques.	32
3.2	Summary of electromagnetic proximal soil sensing techniques.	32
3.3	Inferred soil values from MIR spectra	33
6.1	IVS instrument parameters	68
6.2	INO Hyperspectral imaging parameters	69
6.3	Classifier size comparison	77
6.4	Classification time comparison	78
6.5	Classification comparison for 8 terrain types	79
6.6	Classification comparison for 4 sand types	80
6.7	Classification comparison for 4 aggregate types	80
6.8	Classification comparison for 3 bulk compositions	81
6.9	Classification comparison for 3 bulk compositions	81
6.10	Mean current draw per wheel over terrain types.	82
6.11	Mean wheel speed wheel over terrain types.	83
6.12	Classification comparison for <i>LunaTron</i> data	83
6.13	Mean wheel speed wheel and current draw over LOO predicted terrain.	85
6.14	Mean wheel speed wheel and current draw over COM predicted terrain.	86
6.15	Mean wheel speed wheel and current draw over COM predicted terrain.	87
7.1	List of commonly used ROS Hydro packages.	93

7.2	Times for 180 <i>m</i> figure 8 circuit: Set 1.	99
7.3	Times for 150 <i>m</i> complex circuit: Set 2.	100
7.4	Summary of averaged speeds (<i>cm/s</i>) for all 6 trials.	100
7.5	Summary of errors for all 6 trials.	100
7.6	Indexes of Difficulty for corridor widths.	106
7.7	Linear Regression for 0 second time delay.	106
7.8	Linear Regression for 2 second time delay.	108
7.9	Linear Regression for 4 second time delay.	108
7.10	Linear Regression for Ambient Lighting Condition.	112
7.11	Linear Regression for Bright Spot Light Condition.	113
7.12	Linear Regression for Dark Condition.	113
A.1	Confusion matrix for Bayes classification of three bulk composition from vehicle data	139
A.2	Confusion matrix for SVM classification of three bulk composition from vehicle data	139
A.3	Confusion matrix for Bayes classification of all 8 terrain types from vehicle data	140
A.4	Confusion matrix for SVM classification of all 8 terrain types from vehicle data	140
A.5	Confusion matrix for Bayes classification of sand and aggregate types using transformed images	141
A.6	Confusion matrix for Bayes classification of sand and aggregate types using lidar reflectance	141
A.7	Confusion matrix for Bayes classification of sand and aggregate types using transformed images and lidar reflectance	141
A.8	Confusion matrix for SVM classification of sand and aggregate types using transformed images	142
A.9	Confusion matrix for SVM classification of sand and aggregate types using lidar reflectance	142

A.10 Confusion matrix for SVM classification of sand and aggregate types using transformed images and lidar reflectance	142
A.11 Confusion matrix for Bayes classification of sand and aggregate types using transformed images	143
A.12 Confusion matrix for Bayes classification of sand and aggregate types using transformed images and lidar reflectance	143
A.13 Confusion matrix for SVM classification of sand and aggregate types using transformed images	144
A.14 Confusion matrix for SVM classification of sand and aggregate types using transformed images and lidar reflectance	144
A.15 Confusion matrix for Bayes classification of three bulk composition using transformed images	145
A.16 Confusion matrix for Bayes classification of three bulk composition using lidar reflectance	145
A.17 Confusion matrix for Bayes classification of three bulk composition using transformed images and lidar reflectance	145
A.18 Confusion matrix for SVM classification of three bulk composition using transformed images	146
A.19 Confusion matrix for SVM classification of three bulk composition using lidar reflectance	146
A.20 Confusion matrix for SVM classification of three bulk composition using transformed images and lidar reflectance	146
A.21 Confusion matrix for Bayes classification of three bulk composition using RGB values	147
A.22 Confusion matrix for Bayes classification of three bulk composition using RGB values and lidar reflectance	147
A.23 Confusion Matrix Images	148
A.24 Confusion Matrix Images + Lidar	148

A.25	Confusion matrix for Bayes classification of aggregates using transformed images	149
A.26	Confusion matrix for Bayes classification of aggregates using lidar reflectance	149
A.27	Confusion matrix for Bayes classification of aggregates using spectral reflectance	149
A.28	Confusion matrix for Bayes classification of aggregates using transformed images and lidar reflectance	150
A.29	Confusion matrix for Bayes classification of aggregates using transformed images and spectral reflectance	150
A.30	Confusion matrix for Bayes classification of aggregates using lidar reflectance and spectral reflectance	150
A.31	Confusion matrix for Bayes classification of aggregates using transformed images, lidar reflectance, and spectral reflectance	150
A.32	Confusion matrix for SVM classification of aggregates using transformed images	151
A.33	Confusion matrix for SVM classification of aggregates using lidar reflectance	151
A.34	Confusion matrix for SVM classification of aggregates using spectral reflectance	151
A.35	Confusion matrix for SVM classification of aggregates using transformed images and lidar reflectance	152
A.36	Confusion matrix for SVM classification of aggregates using transformed images and spectral reflectance	152
A.37	Confusion matrix for SVM classification of aggregates using lidar reflectance and spectral reflectance	152
A.38	Confusion matrix for SVM classification of aggregates using transformed images, lidar reflectance, and spectral reflectance	152
A.39	Confusion matrix for Bayes classification of sands using transformed images	153
A.40	Confusion matrix for Bayes classification of aggregates using lidar reflectance	153
A.41	Confusion matrix for Bayes classification of aggregates using transformed images and lidar reflectance	153
A.42	Confusion matrix for SVM classification of sands using transformed images	154
A.43	Confusion matrix for SVM classification of aggregates using lidar reflectance	154

A.44	Confusion matrix for SVM classification of aggregates using transformed images and lidar reflectance	154
A.45	Confusion matrix for Bayes classification of all 8 terrain types using transformed images	155
A.46	Confusion matrix for Bayes classification of all 8 terrain types using lidar reflectance	155
A.47	Confusion matrix for Bayes classification of all 8 terrain types using transformed images and lidar reflectance	156
A.48	Confusion matrix for SVM classification of all 8 terrain types using transformed images	157
A.49	Confusion matrix for SVM classification of all 8 terrain types using lidar reflectance	157
A.50	Confusion matrix for SVM classification of all 8 terrain types using transformed images and lidar reflectance	158
B.1	Times, Errors and Scores for ambient lighting condition	159
B.2	Times, Errors and Scores for the spot light condition	160
B.3	Times, Errors and Scores for the dark condition	160
B.4	Times, Errors and Scores for 0 s time delay	160
B.5	Times, Errors and Scores for 2 s time delay	161
B.6	Times, Errors and Scores for 4 s time delay	161
B.7	Block Scores for 0.85 cm at Ambient Lighting	162
B.8	Block Scores for 0.95 cm at Ambient Lighting	162
B.9	Block Scores for 1.05 cm at Ambient Lighting	163
B.10	Block Scores for 1.15 cm at Ambient Lighting	163
B.11	Block Scores for 0.85 cm with Bright Spot Light	163
B.12	Block Scores for 0.95 cm with Bright Spot Light	164
B.13	Block Scores for 1.05 cm with Bright Spot Light	164
B.14	Block Scores for 1.15 cm with Bright Spot Light	164

B.15 Block Scores for 0.85 cm in Darkness 165
B.16 Block Scores for 0.95 cm in Darkness 165
B.17 Block Scores for 1.05 cm in Darkness 165
B.18 Block Scores for 1.15 cm in Darkness 166

List of Definitions

Acronyms	Definition
AGG	Aggregate
CAN	Controller Area Network
CLA	Crushed Clay Chips
COM	Compacted Sand
COTS	Commercially Available Off-The-Shelf
CPSX	Centre for Planetary Science and Exploration
CRT	Cathode Ray Tube
CSA	Canadian Space Agency
DEM	Digital Elevation Map
DCS	Dry Compact Sand
DLS	Dry Loose Sand
DSMM	Digital Soil Mapping and Modelling
DSMa	Digital Soil Mapping
DSMo	Digital Soil Modelling
ESA	European Space Agency
ESM	Exploration Surface Mobility
FPS	Frames Per Second
GIS	Geographical Information System
GPS	Global Positioning System
GRA	Gravel
HCI	Human-Computer Interaction
IMU	Inertial Measurement Unit
IVS	Integrated Vision System
JPL	Jet Propulsion Laboratory
JSON	JavaScript Object Notation
LIBS	Laser-Induced Breakdown Spectroscopy
LRV	Lunar Roving Vehicle

MIR	Mid Infrared
MIT	Massachusetts Institute for Technology
MDA	MacDonald Dettwiler and Associates
MER	Mars Exploration Rover
MESR	Mars Exploration Science Rover
MSE	Mean Square Error
MSL	Mars Science Laboratory
NASA	National Aeronautics and Space Administration
NIR	Near Infrared
NMEA	National Marine Electronics Association
PQU	Pink Quartz
PSS	Proximal Soil Sensing
PTF	Pedotransfer Function
RGB	Red, Green, Blue
ROS	Robot Operating System
ROV	Remotely Operated Vehicle
RSD	Relative Standard Deviation
SAN	Sand
SINFERS	Soil Inference Systems
SLAM	Simultaneous Localization and Mapping
SVM	Support Vector Machine
UTIAS	University of Toronto Institute for Aerospace Studies
UGV	Unmanned Ground Vehicle
UUV	Unmanned Underwater Vehicle
VSE	Visual Sinkage Estimation
WFS	Wet Flat Sand
WMS	Wet Mixed Sand
WQU	White Quartz

Chapter 1

Introduction

This thesis presents two studies on mobile robotic operations with an intended focus on lunar south pole exploration. A mobile robot is considered to be an off-road vehicle operating either autonomously or under human tele-operative control. The terms ‘rover’, vehicle, and mobile robot are used interchangeably. The first study is on the application of non-contact, proximal lidar reflectance and near infrared spectroscopic measurements to improve classification of terrain over optical imagery alone. Lidar is an active sensor that is invariant to lighting conditions, and near infrared spectroscopy can aid in distinguishing mineral composition between materials. The second study is on human performance in tele-operating a mobile robot in non-ideal lighting conditions over a time delay. Non-ideal conditions, such as bright low-angled lighting, provide challenges to the human operator that become exacerbated with the introduction of video transmission delay. The remainder of this chapter presents the overall research theme and questions, the motivation and problem statement for this research, and an outline for the remaining chapters.

1.1 Research Question

The theme for this thesis is an engineering design trade-off study to consider:

Which operating mode, direct-drive tele-operation or supervisory controlled

lidar-based autonomy, leads to improved scientific return in the context of a near-term, low-cost, short-duration lunar prospecting mission?

This thesis provides evidence to support the following research questions:

Can lidar reflectance intensity and non-contact spectroscopic measurements improve classification of terrain for rover traverse performance prediction

and

Can the degradation in human performance for tele-operating a rover in non-ideal lighting conditions over time delay fit into Cornering Law?

1.2 Motivation and Problem Statement

The rationale for these two studies is based on a system engineering trade-off study for operating a lunar south pole prospecting rover. Proposals for lunar prospecting, which is further described in Chapter 2, have focused on a near-term, low-cost, short-duration mission utilizing either direct-drive tele-operation from Earth or autonomous navigation. The implied constraints of near-term and low-cost are to reuse existing technologies. The implied constraint for short-duration is to maximize the amount of science data return without needing the complexity of lunar night survival. Therefore, a proposed solution involving autonomy must utilize the existing low-computational speed radiation hardened computers. Lidar has been proposed to be used for autonomous navigation, but has yet to be used on a planetary rover and is computationally intensive. A proposed solution with tele-operation must tolerate limited bandwidth data transfer and a 4 second round trip time delay. Furthermore, the lunar south pole will exhibit low-angled lighting that will result in extreme contrasts between light and dark.

Lunar and planetary exploration rovers operate, regardless of level of autonomy, in unstructured environments of uneven terrain, varying soils, and dynamically changing conditions.

Safe and effective operations requires knowledge of the terrain over which the rover traverses. Detecting geometric obstacles, which are defined by their geometric properties, such large boulders or steep cliffs can be readily achieved using sensing techniques such as vision and lidar. Non-geometric obstacles, which are defined by their mechanical properties such as terrain type, require different instruments or analysis to sense [1]. The mechanical properties of loose and compact sand dictate the tractive performance of an off-road vehicle, and loose sand may result in insufficient traction and immobilization, such as what was experienced by the Mars Exploration Rovers *Opportunity* and *Spirit*.

Tele-operated exploration rovers also operate in unstructured environments. The remote human must have sufficient spatial awareness in order to safely and effectively operate the vehicle. A vehicle tele-operated on the moon, such as the early *Lunakhod* rovers, introduces restrictions on data transmission and time-of-light transmission delays that lead to degradation of human performance. A vehicle operated at the lunar poles introduces new challenges from the low-angle lighting. Recent interest in prospecting at the south Lunar pole has renewed interests in the design and operation of Lunar rovers [2, 3].

1.2.1 Abstraction of Problem Statement

Let us first consider a abstraction of mobility prediction for an off-road vehicle with an objective to travel an unfamiliar path from point A to C. In this abstraction it is assumed that a path has already been generated to avoid geometric obstacles. The off-road vehicle travelling from point A to C risks immobilization through non-traversable terrain. Immobilization may be recoverable from external assistance in some cases, or may result in objective failure if assistance is not available.

The vehicle could simply traverse the path to assess whether or not the path was traversable. The vehicle may reach point C and its path AC is *a posteriori* determined to be traversable. Alternatively, the vehicle may be immobilized at point B that is then *a posteriori* determined to be non-traversable. This approach does not provide any context to the terrain at any point along the path other than that fact it was traversable or not. However, this binary response does not

lend itself to future paths. The vehicle may then have a path to point D and would be required to make a similar attempt that could result in immobilization.

A deterministic approach for assessing the traversability would be to measure the terramechanical properties of the terrain at all points along the path between points A and C. This *a priori* knowledge of the terrain along the path provides a high degree of confidence of its traversability. However, this approach has obvious setbacks. It is resource and time intensive to measure the terramechanical properties at all points along the path. There is also the risk that, given the terrain properties are unknown before they are measured, the measuring equipment may become immobilized at a location along the path before knowing the results. It is thus considered impractical to fully characterize through direct measurements the traversability of the path.

A frequentist approach would be to traverse the path several times and record the number of times the traverse was successful or not. The success rate represents the frequency at which successful traverses over that path occur, and that frequency can then be used to assess the probability the traverse will be successful. A Bayesian approach would consider prior experience and knowledge of traversing known paths and use present data to assess the probability of traversing an unknown path.

Let us now consider the case where a human is operating the off-road vehicle from point A to C. A human operator relies on past experience with the vehicle traversing over familiar terrain and terrain conditions such as visual appearance. The operator can then assess the probability that a region is traversable or not, and determine how much tractive effort will be required. In this case the human is using proximal visual appearance of the terrain a few metres in front of the vehicle, and can then feel the response of the vehicle as it traverses it. The human operator can use that experience for future driving events to make probable assessments of traversability. In the event the operator was incorrect in their prediction and the vehicle becomes immobilized, external assistant can free the vehicle.

Finally, let us consider the case where the human is tele-operating the off-road vehicle from A to C. The human relies upon the data transmitted from the vehicle in order to operate it.

When the data transmitted is of lesser quality, or the transmission is delayed, the task becomes more difficult. The human compensates for the increase in task difficulty by reducing the speed at which the vehicle will travel from A to C. The presence of transmission delay or low quality data may also increase the risk of the human immobilizing the vehicle.

1.3 Outline

This thesis is presented in an additional 7 chapters. Chapter 2 provides a review of planetary exploration rovers, and their terrestrial analogues. Chapter 3 provides a review of terramechanical theory, which is the study of wheel-terrain interaction, and terrain classification. Related work in traversability prediction, non-geometric obstacle detection, and proximal soil sensing is also included in Chapter 3. Chapter 4 provides a brief background review of the wavelength transforms and classification techniques in the chapters 6 and 7. Chapter 5 reviews Fitts' Law and its application to tele-operating a mobile robot. Chapter 6 presents the experimental description, results and analysis for the terrain traversability testing, and a discussion of how they can be applied to planetary exploration and terrestrial off-road vehicles. Chapter 7 presents the experimental description, results and analysis for the tele-operation testing, and a discussion of how they can be applied to planetary exploration and terrestrial off-road vehicles. Chapter 8 presents the conclusions and recommendations for future work.

Chapter 2

A Short History of Planetary Exploration

Rovers

An objective of this thesis is to demonstrate technological and operational concepts relevant to the extent of the Canadian Space Agency (CSA)'s potential involvement in future planetary exploration missions. This chapter provides a review of planetary exploration rovers and terrestrial analogues developed for testing rover technology, and also provides context for CSA's activities.

The first remotely operated rover was the Soviet *Lunokhod 1* in 1970. Technology development in communications, robotics, and autonomy has advanced since then, and landers and rovers have successfully operated on Venus, Titan, and Mars. Future missions have been planned or proposed to further explore these planetary locations. Prototypes for robotic explorers have been developed to support both the technology development, and simulated mission operations are conducted in terrestrial analogue environments to feed back into the mission technology development and mission architecture. CSA has increased its involvement in both technology development and analogue operations to support Lunar and Mars exploration.

There are two dominant control architectures when discussing rovers in this thesis: direct-drive (DD) and supervisory control (SC). A third, shared control, is not discussed in this thesis however is included for completeness. These terms are used throughout this report and are

summarized here:

Direct drive The operator directly controls the output of the robot; the robot only responds to the user input. There are no autonomous actions taken on the part of the robot. For a rover, the operator would provide all acceleration and steering commands based on feedback.

Shared Control The operator provides gross commands which are finely tuned autonomously by the robot. For a rover, the operator would assign way-points to an end-point and allow the rover to drive itself along the path whilst avoiding detected obstacles. The operator could also provide all acceleration and steering commands, with the rover reacting to local obstacles.

Supervisory Control The operator assigns high-level tasks to the robot; the robot can then autonomously complete those tasks without intervention. For a rover, the operator would assign an endpoint allow the rover to autonomously plan its own path to that endpoint.

This chapter is divided into five sections: Canada's recent development work in robotic exploration, lunar exploration rovers with their associated operation concepts, Mars exploration rovers and their operation concepts, and concepts for exploration vehicles on other planetary bodies.

2.1 Canadian Space Agency Activity

The Canadian Space Agency, through their Exploration Surface Mobility (ESM) program, developed a number of prototypes to further Canada's planetary exploration capabilities. The targets for these prototypes are both lunar and Mars exploration. These prototype developments include rover systems, science instrumentation, data analysis, and operations. The following section highlights those activities as they pertain to this thesis.

2.1.1 Mars Vehicles and CanMars

Kapvik, as shown in Figure 2.1, is a micro-rover prototype was designed with a view to achieving flight qualification and to help assess potential exploration missions to which Canada may contribute, such as a planetary scout rover. *Kapvik* has a mass of approximately 30 kg. It has an instrumented six-wheeled rocker-bogie system with differential drive similar to NASA's fleet of exploration rovers: *Sojourner* [4], *Spirit* [5], *Opportunity* [6] and *Curiosity* [7]. The rocker-bogie allows all six wheels to maintain ground contact to enhance mobility while allowing the rover to climb over rocks [8, 9].



Figure 2.1: *Kapvik* in its final configuration during final testing at CSA's Mars Yard.

An instrumented chassis with individually throttleable wheel motors was an early design objective for *Kapvik*'s mobility system. The instrumented chassis allows for the mobility system to adapt to changing terrain conditions. Each motor can be individually throttled to provide traction control on Mars micro-rovers. Each of the six wheels is driven by a Maxon Motor RE25 motor with planetary gearing and harmonic drive. The wheel motor assemblies include planetary gearing and a harmonic drive for a gear ratio of 1400:1, and are contained at the wheel base inside an enclosure to protect against weathering and dust. Each of the motor assemblies is powered and driven by a Maxon Motor EPOS 24/1 motor controller. Wheel odometry is provided by incremental encoders attached to each motor. Single axis load cells are mounted on top of each wheel to measure the vertical force. Potentiometers provide the rotational angles of the differential drive and the rockers. When calibrated, the potentiometers provide an orientation of each of the wheels relative to the body frame of the rover. The potentiometers, load cells and incremental encoders all connect to the motor controller; all of the motor controllers are connected via a controller area network (CAN) bus to a central computer on a Xiphos Q6 card, which is located within an avionics enclosure on the rover. *Kapvik* was used to demonstrate on-line terramechanical parameter estimation using the instrumented chassis and a trained neural network [10].

Kapvik was envisioned to accompany a larger rover as a scout. One such large rover is the Mars Exploration Science Rover (MESR) developed by MacDonald, Dettwiler and Associates Ltd. (MDA) for CSA. MESR is a 250 kg six-wheeled rover equipped with a robotic arm to characterize and acquire samples in situ. Characterizing, acquiring, and caching samples for a potential return to Earth is stated mission concept for the Mars 2020 mission [11]. MESR was used in two analogue operations campaigns to test the daily science activity and operations planning required for remote science exploration.

The 2015 CanMars MSR Analogue Mission [12] was a high-fidelity, 11 command-cycle Mars Sample Return (MSR) analogue mission carried out in partnership between CSA, MDA, and the Centre for Planetary Science and Exploration (CPSX) at Western University, as part of the NSERC CREATE project "Technologies and Techniques for Earth and Space Explo-



Figure 2.2: MESR at CSA's Mars Yard. Image credit: CSA.

ration". MESR, 'landed' in mid-November 2015 in a remote location in Utah, USA unknown to the science operations team. The daily science activity planning took place at a mission control centre [13, 14, 15, 16] located at Western University. This analogue campaign included the proximal sensors to incorporate into the decision making process, as an analogue to the SuperCam instrument to be flown on the Mars 2020. A hand-held Raman spectrometer and XRF were modelled as proximal sensors for the purposes of the analogue operations [14].

2.1.2 Lunar Vehicles and RESOLVE

In addition to Mars rovers, CSA developed lunar prototypes with a view to participating in a south lunar pole lunar prospecting mission. Prospecting for, and eventually harvesting, lunar resources is required for establishing bases on the moon and possibly required for sending humans to Mars. Sending humans to Mars will require vast amounts of water and oxygen. Sending those humans back to Earth will require fuel to propel the ascent vehicle from the surface. Being able to produce fuel, water, and oxygen from the resources available on those surfaces saves the equivalent mass needed to be launched from Earth. In-situ resource utilization (ISRU) is therefore a key technology development needed to reduce overall mission costs and expand space and planetary exploration.

The lunar regolith must first be studied in greater detail in order to characterize the resources available for lunar ISRU. Results from data analysis of *Clementine* and *Lunar Prospector* showed the south polar regions contains 1700 ± 900 ppm of hydrogen. Depending on the source of that hydrogen, it could be accompanied by other volatiles such as methane; also, the hydrogen could be in the form of ice. Oxygen is also present in lunar regolith in the form of minerals. However, the composition and concentration of these materials is still only an estimate [17].

Knowing the characterization of lunar regolith at the south pole is only the first problem to solve. The next is processing the regolith to extract useful products. The Regolith and Environment Science and Oxygen and Lunar Volatile Extraction (RESOLVE) mission has been proposed to study the resources available at the lunar south pole and the technologies needed to process the regolith. For such a mission, a rover would carry the RESOLVE payload suite that consists of hardware to excavate regolith, characterize bulk regolith and physical properties, characterize the volatiles, and extract oxygen and water resources from regolith [17, 18]. A current baseline reference mission [2] relies on operating the prospecting rover during one lunar sol of about 10-14 Earth days.

2.2 Lunar Exploration Rovers

The Soviet space program landed several probes onto the lunar surface in the 1960s and 70s, including the first two planetary rovers *Lunokhod 1* and *2*. Both *Lunokhod 1* and *2* were tele-operated by direct-drive from Earth. Two teams of five took turns operating the rovers: a commander, a driver, a navigator, an engineer, and the radio controller. The operators reported high levels of fatigue after short operating periods due to the low-quality imagery and time delay. *Lunokhod 1* operators were reported to have heart rates of up to 130-140 beats/min during early manoeuvres [19, 20]. Images were sent back from *Lunokhod 1* at 1 frame per 20 seconds requiring the drivers to memorize features ahead of the rover while still driving and waiting for the next update. For *Lunokhod 2* this was improved to 1 frame per 3.2 seconds.

The drivers also had to cope with extreme light contrasts, from shadows to glare. After 11 months and 10.54 *km* of traverse, *Lunokhod 1*'s mission ended. One year later the same teams of operators controlled *Lunokhod 2*. By the end of *Lunokhod 2*, the operators had a 47 *km* worth of time-delayed tele-operations experience [19].

The 1973 *Lunokhod 2* was the most recent mobile robotic mission to the moon until the Chinese National Space Agency landed its Chang'e 3 *Yutu* rover in 2013 [21]. *Yutu* traversed approximately 110 *m* from the Chang'e 3 lander [22]. NASA had also landed several probes onto the lunar surface, including the manned Apollo missions. Later Apollo missions included a lunar roving system, however this vehicle was remotely operated. NASA has never operated a rover on the moon, however the recent interest in lunar prospecting has resulted in a several studies and terrestrial prototypes.

2.2.1 Prototypes and Mission Concepts for Lunar Exploration Rovers

The *Scarab* rover, shown in Figure 2.3, was developed at Carnegie Mellon University (CMU) to carry a RESOLVE payload in simulated lunar environments. It was designed for repeated coring over several kilometres of traverse, and for navigating in darkness. The simulated environments include Glenn Research Centre (GRC) Simulated Lunar Operations (SLOPE), Moses Lake Dunes, Washington, and Pacific International Space Center for Exploration Systems (PISCES) at Mauna Kea, Hawaii. The deployment at Mauna Kea in November 2008 included the RESOLVE drilling system development by the Northern Centre for Advanced Technology (NORCAT).

The *Scarab* operator specified a target, or multiple targets, within a 3 or 10 *m* radius and the rover autonomously navigated to those targets. *Scarab* used Neptec's TriDAR¹ laser range scanners for obstacle detection and terrain modelling in the dark; stationary laser scans were taken after 3 *m* of traverse, after 10 degrees of rotation, or after 100 s of elapsed time. The resulting point cloud data was merged into the world terrain model. An underside optical velocimeter provides estimates of the rover velocity. The rationale for using active sensing was

¹Neptec's TriDAR system combines a laser camera (based on triangulation) with lidar

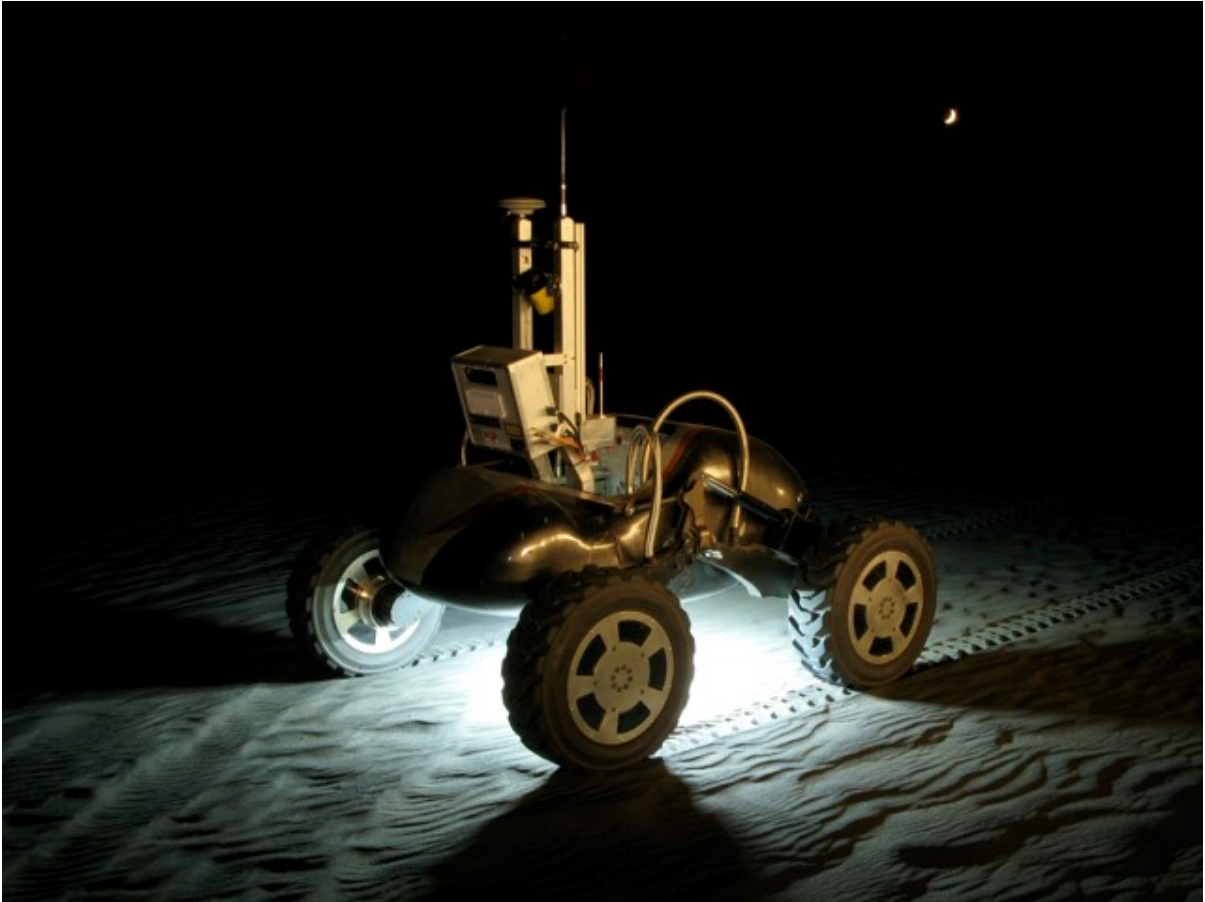


Figure 2.3: *Scarab* rover in dark lighting condition illumination the surface below itself.
© Field Robotics Centre, Carnegie Mellon University.

to facilitate operations in the harsh lighting conditions of the south lunar polar environment. The field tests were conducted for 8 hours overnight, during which the rover was operated for more a kilometre worth of traverses. These distances were reached despite minor systemic, though remotely recoverable, errors with the rover that occurred during the 8 hour operations window [23, 24].

The University of Oklahoma designed the *Copernicus* rover [25, 26], shown in Figure 2.4 to test a lunar rover mobility system concept and conducted field trials in the lava fields of the Mojave desert under lunar-like operating conditions. Their concept was based on a goal to traverse several kilometres per day on the lunar surface with a direct-drive tele-operator, a



Figure 2.4: *Copernicus* was tele-operated by direct drive over 4 second time delay. © IRL, University of Oklahoma.

distance greater than the sub-kilometre traverses of similarly operated *Lunokhod*. The mobility system was designed to be robust to occasional shocks due to falls from 30 cm off of a rock due to occasional operator error.

During six days of field tests, the driving conditions were adjusted to be closer to be lunar-like: a 4 s time delay over a 100 kbit/s communication link and low resolution video streamed back at 1.5 - 2 FPS. The operator drove the rover with a joystick using the video feedback from the rover. By the sixth day the rover operated its full traverse speed of 35.5 cm/s. The total drive, including stops for panoramic imaging and driver rest, was 1.9 km over 170 min, for an average speed of 18.6 cm/s. At that speed the rover could traverse 16 km per day with several

operators in rotation.



Figure 2.5: Ames Research Center *K10*. Image credit: NASA/Ames Research Center.

NASA has tested a fleet of lunar rover test platforms and prototypes: the *Lunar Electric Rover (LER)*, now called *Space Exploration Vehicle* [27] (*SEV*), the NASA/ARC *K10* rover [27] (shown in Figure 2.5), NASA/JSC *Centaur2* rover [28] and NASA/ARC *KRex* [28]. Each of these rovers were driven in analogue environments to assess lidar-based navigation.

The on-board computing power of these rovers is greater than what would be seen on a typical planetary rover. *K10* and *LER* were provided with dual core 2.33 GHz processors and 2 GB of RAM [27]. Similarly, *Centaur2*'s navigation computer ran an Intel i7-620M at 2.66 GHz with 4GB DDR3 RAM [28]. The current computational effort available on flight hardware make autonomous navigation impractical for a short duration mission.

Table 2.1 provides a comparison of the lunar rover systems. It is worth noting that the semi-autonomous systems navigating using Lidar systems had either low operational speeds (*Scarab*,

2.9 *cm/s*) or high CPU rate (*KRex*, 2.66 *GHz*). The tele-operated *Copernicus* rover had a speed of 35.5 *cm/s* while using an Apple G3 (233–500 *MHz*), which is similar to the 200 *MHz* RAD 750 Rover Compute Element (RCE) of the Mars Science Laboratory *Curiosity* [29].

Table 2.1: Lunar Rovers and Prototypes [23, 24, 25, 26, 27, 28]. The operation scenarios are listed as either direct drive (DD) or supervisory control (SC). The average speed takes into account time that the rover was stationary; the average speed can be used to determine total distance covered over an operational period accounting for pauses, troubleshooting, and sampling.

Specification	<i>Lunokhod 1</i>	<i>Lunokhod 2</i>	<i>Scarab</i>	<i>Centaur2 & KRex</i>	<i>K10</i>	<i>LER / SEV</i>	<i>Copernicus</i>
Mass (kg)	756	840	280	-	-	-	60
Design Speed (cm/s)	55	55	3-6	-	60	300	35.5
Avg Speed (cm/s)	0.13	0.43	2.9	15-25	-	-	18.6
Number of Wheels	8	8	4	4	4	4	4
Wheel Dia (cm)	51	51	71	-	-	-	74
Power	-	-	120 W	-	-	-	Solar
Sensors							
Lidar	No	No	TriDAR	10 Hz	40 Hz	75 Hz	No
Cameras	Yes	Yes	No	Stereo	Stereo	Stereo	Stereo
Frame Rate (FPS)	0.05	0.3	-	-	-	-	1.5 - 2
IMU	No	No	Yes	Yes	Yes	Yes	Yes
GPS	No	No	Yes	Yes	Yes	Yes	Yes
Velocimeter	-	-	Yes	-	-	-	-
Computing							
CPU	-	-	800 MHz	2.66 GHz	-	-	Apple G3
RAM	-	-	256 MB	4 GB	-	-	-
Operations	DD	DD	SC	SC	SC	SC	DD
Time Delay (s)	> 4	> 4	-	-	10	-	4
Date Rate	low	low	-	1 Mbps	-	-	100 kbit/s

2.3 Mars Exploration Rovers

High-latency, low-bandwidth, non-persistent communication between Earth and Mars requires robotic activity to be supervisory controlled. Operators on Earth utilize data sent back from the rover to formulate an activity plan that is uploaded via the Deep Space Network (DSN). Robotic instrument deployment requires lower-level instructions for precise implementation, whereas rover traverses are typically provided as high-level way-points. The rover's on-board autonomy then provides for hazard avoidance. Rover autonomy has improved with each successive mission. However, it is important to note that the speed with which the rovers could execute autonomous navigation is limited by the on-board computation. Space qualified radiation hardened computers are slower than their terrestrial contemporaries. A summary of Mars rover computational capabilities is provided here:

Table 2.2: Computational capabilities of Mars rovers [29].

Year	Mission / Rover	CPU Speed	RAM	Rover Speed
1997	<i>Sojourner</i>	0.1 MHz	512 KB	0.6 cm/s
2004	MER	20 MHz	128 MB	3.6 cm/s
2012	<i>Curiosity</i>	200 MHz	256 MB	4 cm/s
2021	ExoMars	-	-	0.78 cm/s

The first attempt to land a rover on Mars was the Soviet Mars2 mission, which reached orbit in 1971. However, its PROP-M rover was never deployed after the descent module failed on entry [30]. The first successful landing of a rover was NASA's 1997 Mars Pathfinder mission and its *Sojourner* rover. *Sojourner* operated on a reactive system and did not maintain a permanent terrain map [29]. *Sojourner* operated with a top speed of approximately 0.6 cm/s [4] for 30 sols [31].

Following the success of Pathfinder was the Mars Exploration Rover (MER) mission. The twin MER rovers *Spirit* and *Opportunity* landed in January 2004. They utilized stereo cameras to identify terrain features for navigation. The operator would select way-points and the rovers would then identify paths absent of geometric obstacles to reach subsequent way-points. The MER rovers had a top travel speed of 5 cm/s. Under autonomous driving conditions, the

rovers could achieve an averaged speed of 3.6 cm/s without obstacle avoidance, or 1 cm/s with obstacle detection in benign conditions [32], or as low as 0.1 cm/s with full AutoNav [33].

However, as stated in Chapter 1, *Spirit's* mission ended due to permanent immobilization in loose terrain. *Spirit* wasn't the only MER to be impeded by loose terrain. *Opportunity* encountered 30 cm of loose aeolian deposits at Meridiani Plains in which all six wheels became embedded. The rover required 23 Sols and 150 m of commanded wheel movements to move 26 cm and free itself from the "Purgatory Ripple" [6]. *Spirit* and *Opportunity* became immobilized due to the presence of a non-geometric obstacle not identified by their on-board hazard avoidance autonomy: loose terrain. The loose terrain that trapped *Spirit* was believed to be a weakly cohesive mixture of sulfate and basaltic sands that caused the rover to experience greater wheel slip and wheel sinkage. The tractive force generated by the wheel-terrain interaction was not enough to overcome the terrain resistance. Classical terramechanics theory, with previously estimated terrain parameters, validated this conclusion [5]. *Opportunity* continues to operate at time of writing.

The Mars Science Laboratory (MSL) *Curiosity* rover landed in Gale Crater in August 2012. Its original mission life was one Mars year (687 Earth days), which has since been exceeded and continues to operate at time of writing. *Curiosity* has a drive speed of 4 cm/s that reduces to 1.5 cm/s under autonomous control [34].

Following *Curiosity* is the joint ESA-Roscosmos mission ExoMars that includes both a lander and a rover in addition to the trace-gas orbiter [35]. The ExoMars rover will carry scientific payload to perform exobiology and geology studies of samples collected from up to 2 m below the surface. The rover will operate for a baseline of 220 sols, and can travel at 0.39 cm/s in full autonomy mode, or up to 0.78 cm/s with reduced safeguards [36].

NASA's yet-to-be-named Mars 2020 mission, which would launch in 2020 and land on Mars in 2021, is planned to feature a rover largely similar to *Curiosity* to reduce mission development costs. The planned objective for Mars 2020 is to acquire a diverse collection of returnable samples including those that may contain bio-signatures [11]. Mars 2020 will contain a new suite of instruments to meet those objectives, including the SuperCam remote micro-

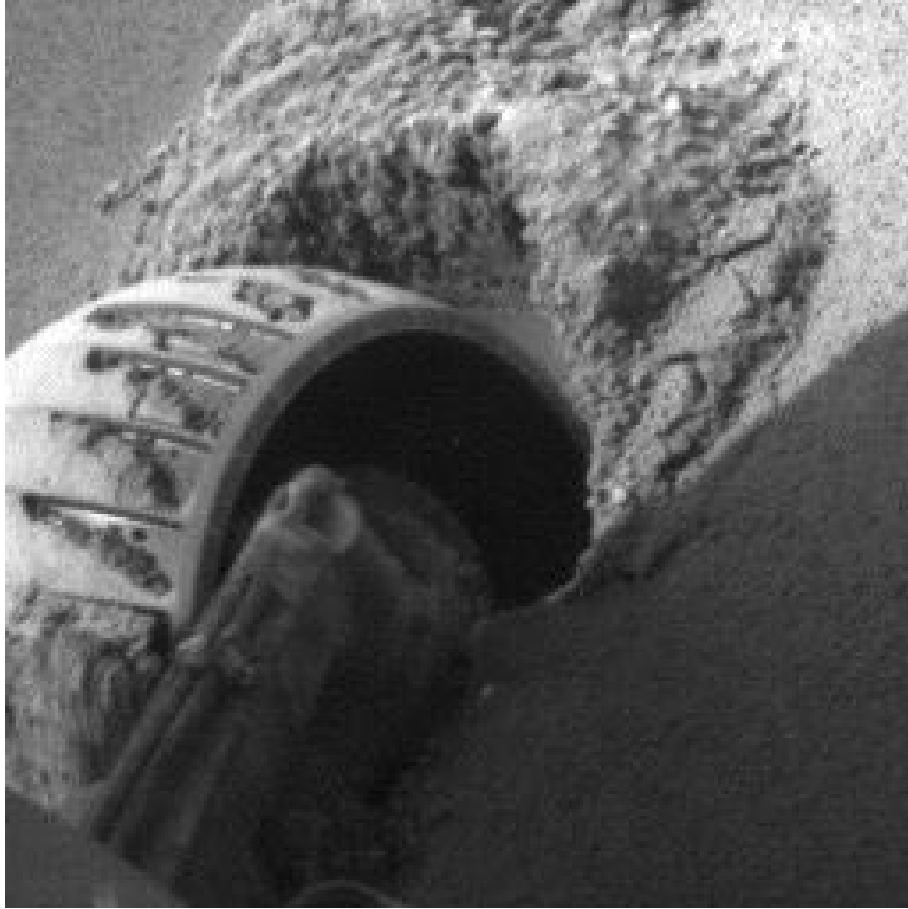


Figure 2.6: *Opportunity*'s hazard identification camera image of embedded left-front wheel. Image credit: NASA/JPL-Caltech.

imager. SuperCam will comprise of a Laser Induced Breakdown Spectrometer (LIBS), Raman Spectrometer, time-resolved fluorescence (TRF) spectrometer, visible and infrared (VISIR) reflectance spectrometer, and colour remote micro-imager (RMI) [37].

2.4 Other Planetary Exploration Vehicles

Planetary exploration missions with mobile robotic vehicles are under conceptual development. Proposed targets for new exploration missions outside the Moon and Mars include Venus [38, 39], Titan [40] and Europa, although a lander was not included in the most recent Europa Clipper mission concept [41, 42].

Venus, which has surface temperatures of 454°C and pressures of 92 bars, has not seen a landed mission since 1985. The Soviet Venera program landed several probes on the surface, though surface operations were limited by the environment; Venera 13, the longest lived lander, operated for 127 minutes. Significant technology development is required for designing a rover that can operate on Venus for longer duration. NASA has studied Venus rover concepts and technology development for a 2040 reference mission [38, 39], and Roscosmos has conceived a new mission called Venera-D that would include a robotic lander[43].

The Saturnian moon of Titan was first visited by the Cassini-Huygens probe in 2005 [44]. Titan is the only other object in the solar system that exhibits evidence of surface-level liquid lakes. Mission concepts to Titan have included robotic platforms such as a short-lived lake lander, a lake boat, and a submarine. The submarine is proposed to have a baseline mission of 90 days, with extension to 300 days, in 2047 to ensure adequate communication with Earth [40].

Chapter 3

Mobile Robot Terrain Traversability

This chapter provides a review of terrain traversability prediction, and its relation to mobile robot performance. The underlying wheel-terrain interaction theory, terramechanics, is first presented. The terramechanical properties of terrain determine the tractive force that can be developed by the mobile robot's wheels. Different types of terrain have differing terramechanical properties and resultant wheel-terrain interaction conditions. Therefore, the traction developed by the wheels will vary by terrain type. The remainder of this chapter presents past studies on terrain estimation and classification, soil science and geographic techniques for identifying terrain, and the terramechanical properties of planetary terrain.

The Mars Exploration Rover (MER) *Spirit*, shown in Figure 3.1, landed on the plains of Gusev Crater on 4 January 2004. Its original mission life was 90 Martian solar days, otherwise known as sols. *Spirit* continued to operate until sol 2210 when communication with Earth ended. Its right front wheel drive actuator failed during its extended mission. This failure caused the front right wheel to be pushed through the terrain instead of being actively driven. *Spirit* continued its extended exploration mission with five active wheels until it became embedded in loose terrain on sol 1871. Several attempts were made to extract *Spirit* from the loose soil. However, on sol 2104 the right rear wheel also failed which furthered impeded *Spirit's* mobility. With only four functioning wheels, *Spirit* was unable to overcome the terrain resistance and continued to function merely as a stationary research base [5].

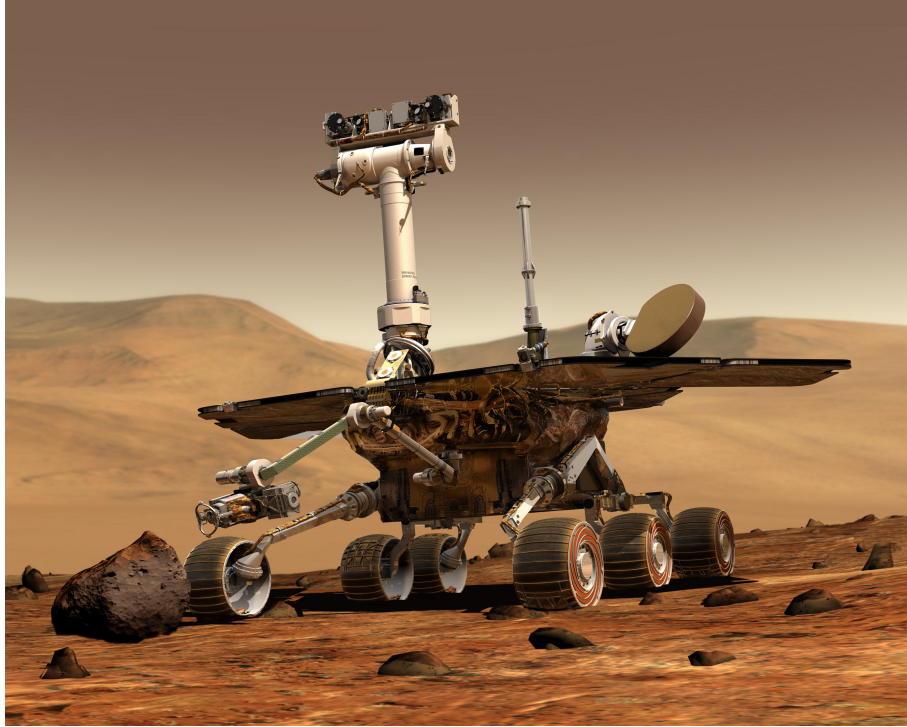


Figure 3.1: The Mars Exploration Rover *Spirit* became a stationary research base after becoming immobilized by a non-geometric obstacle: loose terrain. Image credit: NASA/JPL-Caltech.

3.1 Terramechanics

Terramechanics is the study of vehicle-terrain interaction mechanics. Vehicle-terrain interaction models developed by Bekker [45] and Wong [46, 47] use parameters specific to particular soils. The objective of these models is to predict with reasonable certainty how the vehicle will perform on a given terrain. Previous work by Bekker and Wong studied vehicle-terrain interaction using a variety of terrains: mineral terrains, organic terrains and snow. Mineral terrains include sand, sandy loam, clayey loam, and loam. Organic terrain and snow exhibit greater compressibility and do not conform to the plastic material model presented later. Bekker and Wong also studied vehicle-terrain interaction using a variety of vehicle running gears: rigid wheels, flexible wheels, rigid tracks and flexible tracks, amongst others. Rigid wheels have been used on past, current and planned Mars exploration rovers (*Sojourner*, *Spirit*, *Opportunity* and *Curiosity*); rigid wheels were included on the *LunaTron* micro rover.

Classical terramechanics theory developed by Bekker [45] has been applied to planetary vehicles since the Apollo program [48, 49]. Much of the recent research on applying terramechanics to planetary rovers has been led by the Massachusetts Institute of Technology (MIT) Field and Space Robotics Laboratory and MIT Robotic Mobility Group [50, 51, 52].

Vehicle-terrain interaction models require knowledge of how the terrain responds to forces applied by the vehicle. Terrain can be modelled as either an elastic or plastic material; both models have their advantages and disadvantages. Modelling terrain as an elastic material allows for classical elasticity theory to be applied to analysis: the strain, or deformation, of the material is proportional to the stress applied. The wheel weight is modelled to be a point mass acting on the terrain. The stresses within the terrain are a function of the distance from the point mass. The elastic model estimates the stress distribution pattern that radiates from the point load through the terrain. Usage of the elastic model is limited to vehicle loads within the elastic behaviour region of dense terrain. When the vehicle load reaches the limit of elastic behaviour, the terrain is at the critical state between elastic and plastic behaviour; the terrain is in plastic equilibrium. The terrain material transitions from plastic equilibrium to a plastic flow state when the load continues to increase. Wong states that the terrain has failed at this point. The Mohr-Coulomb failure criterion is widely used to define the failure of soil:

$$\tau = c + \sigma \tan \phi \quad (3.1)$$

where τ and σ are the shear stress and radial stress, respectively, at the wheel-terrain interface; the terrain cohesion c and shearing resistance angle ϕ are the two terrain parameters to be estimated. The Mohr-Coulomb criterion is limited to static loads on terrain as it does not take into account the shear deformation at the wheel-terrain interface. The plastic terrain model can only be accurately applied to dense terrains, such as sand, subjected to high vehicle loads. The model does not apply well to highly compressible terrains such as snow and organic terrain.

The mechanics of wheel-terrain interaction can be determined with knowledge of the terrain. Bekker [45] and Wong [46, 47] developed rigid wheel-terrain interaction models for wheels that are stationary, driven, towed, pushed, and breaking. The wheels on planetary rovers are individually powered and controllable to allow for throttling and enhanced traction control.

Therefore, the *LunaTron* rover, described in Chapter 6, uses individually powered motors.

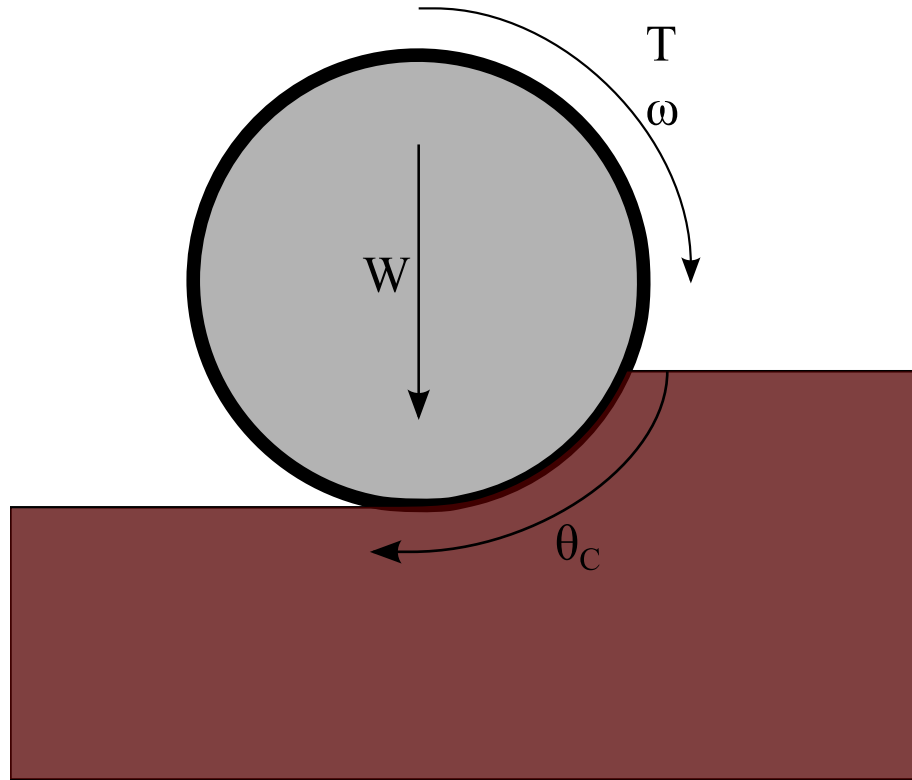


Figure 3.2: Diagram of rigid wheel in contact with terrain. W is the weight on the wheels; T is the torque driving the wheel; ω is the rotational velocity of the wheel; and θ_C is the wheel-terrain contact angle

The mechanics of a rigid wheel in motion can be studied by examining the free body diagram in Figure 3.2 and the following equation for the shear stress distribution along the wheel-terrain interface [47]:

$$\tau = (c + \sigma \tan \phi) \left(1 - e^{-\frac{d}{K}}\right) \quad (3.2)$$

where

- The shear deformation parameter K is experimentally derived for a particular terrain;

- c is the terrain cohesion and one of the parameters to be estimated;
- ϕ is angle of shearing resistance and is the other parameter to be estimated;
- The amount of slippage $J = f(i, \theta_C)$ is determined by the slip ratio $i = 1 - V/r_W \omega$ from the measurable rover velocity V and the motor shaft rotational speed ω ;
- The shear stress $\tau = f(I, \theta_C)$ over the contact area $A = r_W w_W \theta_C$ is determined from the torque T applied by the motor, which draws a measurable current I ;
- The normal stress $\sigma = f(W, \theta_C)$ is determined by the measurable wheel load W acting over the contact area $A = r_W w_W \theta_C$; and
- The wheel radius r_W and width w_W are known values.

The shear stress τ in Equation 3.2 determines the maximum allowable thrust available to propel the wheel. The terrain cohesion and shearing resistance angle therefore influence a rover's thrust $F = f(\tau)$. A decrease in either cohesion or shearing resistance angle will result in a decrease in the maximum thrust available at the wheel. When the thrust available is less than the resisting force of the terrain, the wheel becomes immobilized.

3.2 Traversability Prediction and Terrain Classification

This section provides a review of traversability prediction for mobile robots (unmanned ground vehicles). The general approach to traversability prediction is to compare exteroceptive and proprioceptive data to classify robot traversal performance against terrain features. Further approaches estimate wheel-terrain interaction parameters such as wheel slip, wheel sinkage, and terrain cohesion c and shearing angle ϕ .

3.2.1 Terramechanical Parameter Estimation

Previous work has focused on estimating the terramechanical terrain properties, c and ϕ as those parameters are used to determine traction. Tan [53] and Yousefi Moghaddam [54] each

proposed a method for estimating terrain parameters online; however their application was for excavation and not based on wheel-terrain interaction. Iagnemma used a simplified wheel-terrain interaction model [50, 51, 52] for estimating the two terrain parameters online for an exploration rover. He solved for c and ϕ using linear least squares with a set of sensor data (V, ω, z, I) and assumed values (K). His laboratory experiments, using an instrumented testbed, showed that the least squares estimates for the c and ϕ values of the sand were within range of the bevameter measurements. An *a priori* value for the shear deformation parameter was needed to solve the least squares estimate. He also estimated the terrain parameters for a six-wheeled rover in a Matlab simulation using simulated noisy sensor data. His simulation results showed that the least squares estimates of sand were within error. Iagnemma's simulation did not describe how the wheel sinkage, or wheel-terrain contact area, was measured; only a simulated value was used for the estimation of the terrain parameters. Cross [10] trained an artificial neural network to map sensed rover parameters to terrain parameters as a means of estimating instantaneous changes in terrain conditions.

3.2.2 Wheel Sinkage Estimation

Wilcox [1] describes a method to detect sinkage on a six-wheeled articulated rover. The rover with which this was tested was functionally equivalent to the Mars Pathfinder rover *Sojourner*. The rover's rocker-bogie linkages allowed all six wheels to remain in contact with the terrain. These linkages were passive but instrumented to sense the pitch and articulation. Wilcox presents a simple model of a rover driving over undisturbed terrain. The elevation differences between the front and rear wheels are calculated based on the pitch and articulation values. Forward looking lasers sense the elevation of terrain ahead of the rover. The elevation difference from the rear wheel to the points ahead of the rover are also computed. He assumes that the front wheels will sink into the undisturbed terrain. He further assumes that the rear wheels will not sink further into the soil when driven over the same terrain. Wilcox notes that if this assumption is not approximately correct it will lead to a general failure of the entire method. The elevation difference between the front wheel and rear wheel, as estimated with the rocker-

bogie pitch and articulation angles, is the basis of the sinkage estimate; the forward elevation difference is the basis for the future sinkage prediction. Wilcox's results with the rover showed that his method worked well to indicate sinkage; however due to large sensor noise it was not able to provide a good estimate of the sinkage. He also noted that the computer resources were already burdened with navigation and mobility calculations and this sinkage estimate could only be performed once per wheel radius of traverse.

Reina [55] proposed a visual sinkage estimation (VSE) algorithm to estimate the wheel-terrain contact angle and the wheel sinkage. Their proposal required a pattern of concentric black circles on a white background be attached to the inside of the wheel. This proposal also assumes a camera will be in visual contact with the wheel-terrain interface. They tested their VSE algorithm on a 16 *cm* diameter wheel in a variety of lighting and terrain conditions. Images were captured and processed at 5 *Hz*. The average estimation error was 8% and did not exceed 15%. The estimation error could be reduced with better cameras and finer wheel patterns. The advantage to VSE is its simple implementation: a patterned wheel cover, a camera, and an image processor. Its disadvantage is the mass, power and computation required to implement. Estimating sinkage on more than one wheel would require more cameras, more wheel covers and more image processing.

3.2.3 Slip Estimating

Reina [55] proposed combining three indicators to detect linear slip or skid: comparing encoder readings with each other; comparing encoder readings with z-axis gyro readings; and monitoring the motor currents. The encoder indicator uses fuzzy logic to compare the differences in longitudinal velocity between wheel pairs. The gyro indicator determines if there is any z-axis rotation compared to the wheel commands. The current indicator uses measured motor current and classical terramechanics theory. The torque applied to the wheel is a function of the current drawn by the motor. An estimation of the current required to overcome rolling resistance can be made for known terrain conditions. Slip is detected when the actual current drawn differs from the required current by a predefined percentage. They tested their

slip detection indicators in a laboratory setting. Their rover was driven over both a sandy slope and two sand mounds. When logically OR-ed the indicators correctly detected slippage 94% of the time on the sandy slope and 61% of the time on the two sand mounds. The slip indicators are useful to indicate if the wheels are slipping beyond a specific threshold. These indicators are not able to quantify slip, however the current indicator does present a simple metric to flag loose soil or drift material.

3.2.4 Proprioceptive and Exteroceptive Terrain Classification

Angelova [56] used stereo imaging, IMUs, and wheel encoders of a mobile robot to measure and predict slip over a variety of terrain types: sand, soil, grass, gravel, asphalt, and wood-chips. The acquired images only considered the image plane corresponding to where the mobile robot would traverse, and the images were subdivided into image patches. Each image patch formed a 75-dimension feature vector of a local pixel neighbourhood. The features are clustered with a k-means algorithm with cluster centres belonging to defined ‘textons’. A texton represents a textural feature, such as spots, grooves, or ridges [57]. histogram of texton occurrence forms the basis of classification: two image patches with similar texton histograms are interpreted to be of similar terrain. The terrain classifier had overall success rate of 76.4%. The classifier degraded in performance the further the image was taken from the mobile robot. Vehicle data, namely wheel slip and orientation, was collected as mobile robot drove over the terrain. A receptive field regression algorithm was used to learn slip from terrain geometry obtain from stereo imagery.

Brooks [58] classified three terrain types, sand, dirt, and gravel, using vehicle vibrations. The power spectral density of the vibration signal was classified using linear discriminate analysis and voting system. The results showed that the three terrain types could be classified with greater than 90% success.

Brooks [59] and Halatci [60] present vision- and vibration-based methods for classifying between rock, sand and beach grass. Vision-based classification compared features derived from RGB colour values, wavelet transform texture features, and stereo-image based surface

geometry. Vehicle vibrations were measured as the mobile robot drove over the three terrain types. These features were trained on mixture of Gaussians (MoG) modelling and support vector machines. The geometry-based features performed poorly due to the resolution of the stereo camera. The RGB colour based MoG classifier performed better than the texture-based MoG classifier. A fusion of vehicle vibrations and image features resulted in an overall accuracy of 84%.

Kleiner [61] furthered this classification method by incorporating laser-range data. Statistics of the height information of reflected points of laser scans are used to derived feature vectors for each terrain class. A trained SVM with laser-based information achieved 85% accuracy when classifying grass, asphalt, gravel, pavement, and indoor flooring. A Bayesian classifier incorporating both image features and laser features resulted in accuracy greater than 90%.

Brooks [62] later used vehicle vibrations and traction in combination with imaging to classify terrain classified bentonite, clay, orange sand, topsoil and wet topsoil using support vector machine (SVM) classification. A traction coefficient was derived from terramechanical theory and Iagnemma's [52] simplified wheel-terrain interaction model for each of the terrain types. Vibrations were shown to be suitable for trained classification, while traction coefficients were suitable for self-supervised classification.

Libby [63] used acoustics from vehicle-terrain interaction to classify grass, pavement, gravel, water, hard objects, and loss of traction with SVM. Acoustic features were compared for classification accuracy. A 9-dimensional vector combined temporal and spectral characteristic, and spectral moments. The overall accuracy of the SVM classifier was shown to be 92%.

Michel [64] used an artificial neural network to classify gravel, crusty soil, and sand with images. Each image was transformed using 2-level Daubechies wavelets for a resultant 24-dimensional feature vector. The ANN was trained with 1050 samples, and the classifier resulted in 84% accuracy.

3.3 Soil Inferencing and Proximal Soil Science

This section provides a review of proximal soil science with a focus on proximal sensing techniques and applications.

Proximal soil sensing (PSS) differs from remote sensing in that remote sensing instruments are typically deployed on airborne vehicles or low-Earth orbiting satellites. PSS is the act of taking local soil measurements with instruments deployed within approximately 2 m from the soil [65], and instruments may be rover-mounted for mobile applications [66]. Proximal soil sensing (PSS) differs from remote sensing in that remote sensing instruments are typically deployed on airborne vehicles or low-Earth orbiting satellites. PSS instruments are deployed within 2 m of the soil surface and may be rover-mounted for mobile applications [66]. PSS also differs from contact sensing in which instruments directly interact with the soil. Adamchuck [66] notes that conventional soil science uses time and resource intensive soil sampling and laboratory analysis to measure soil properties, and McBratney [67] has demonstrated that proximal soil sensing techniques can produce results with only mild loss of accuracy.

Adamchuck [66] provides a summary of research and development of proximal soil sensors to be used on-the-go in situ. Optical and radiometric sensors cover a wide range of instrument types and soil properties that can be measured. Subsurface soil reflectance / absorption sensors use the visual and infrared electromagnetic spectrum to detect energy levels reflected / absorbed by soil particles. These sensors can be used to measure the following: carbon content, soil texture, cation exchange capacity, soil water content, soil pH, and some mineral content. Other radiometric sensors include microwave sensors can measure water content, gamma radiometers can measure mineralogy, and ground penetrating radar can measure water content and the geophysical soil structure [66].

Laser-induced breakdown spectroscopy (LIBS) uses an optically focused solid-state laser to generate a high-temperature plasma from a target surface. The constituent material in the plasma then emits radiation upon cooling. The emitted radiation is delivered to a spectrometer via an optical collector such as fibre optic cable. [68]. LIBS is being used as a proximal soil

Table 3.1: Summary of proximal soil sensing techniques.

Sensing Method	Measured values
Electromagnetic	Organic matter content, soil texture, cation exchange capacity, soil water content, soil pH, mineral nitrogen, carbon and phosphorus
Radiometric	Water content, mineralogy, geophysical structure
Electric	Soil type, texture, water content, organic matter content, depth variability, soil pH
Electrochemical	Soil pH, potassium nitrogen, and sodium content
Acoustic	Soil structure, soil compaction
Pneumatic	Soil structure, water content, soil type.

Table 3.2: Summary of electromagnetic proximal soil sensing techniques.

Sensing Method	Measured values
VNIR < 1000 <i>nm</i>	Iron minerals
SWIR 1000 - 2500 <i>nm</i>	Clays, some carbonates, micas, sulfates
LWIR 8000 - 14,000 <i>nm</i>	Silicates, some carbonates

sensor because of its rapid and dense collection of soil data [69], its lack of sample preparation [68], and its potential for use at a distance up to 90 *m* distance [70].

A number of other sensors types have been deployed to measure other soil properties. These types include electrical and electromagnetic, acoustic, pneumatic, electrochemical and mechanical [66]. Cunningham [71] used a continuous-wave laser to estimate the thermal diffusivity of terrain; the thermal diffusivity was then used to estimate the bulk density of the terrain. Burton [72] demonstrated that lidar reflectance intensity correlated to weight percent clay, and weight percent combined quartz, feldspar and plagioclase. The wheel-terrain interaction of an instrumented vehicle has been used to estimate soil mechanical resistance, or rolling resistance from a terramechanics perspective [73, 74].

Soil inference systems (SINFERS) have been demonstrated to infer soil properties from existing or sensed data, specifically spectral data [75, 67]. Pedotransfer functions (PTFs) are qualitative soil properties expressions to “translate data we have into what we need” [76].

McBratney [67] used PTFs to infer clay, sand, and organic carbon content from MIR spectral data. McBratney notes that inferred values are not as accurate as laboratory values, with R^2 values for inferred values using partial least squares regression shown in Table 3.3. From these inferred values further soil properties were inferred using additional PTFs. The available water capacity of soil was inferred from MIR spectra and PTFs to within 10%. The accuracy of

Table 3.3: Inferred soil values from MIR spectra

Inferred Value	R^2
Clay Content	0.79
Sand Content	0.82
Organic Carbon Content	0.77

inferred values is less than laboratory values. However, the efficiency of deriving many values from a single measurement is useful for rapid in-situ analysis, so long as the error values are understood. In McBratney's example, a single MIR data set can infer numerous soil properties. An example of SINFERS adapted from McBratney [67] is presented in Figure 3.3.

SINFERS, when combined with on-the-go PSS, offer the potential to predict the desired soil properties from the available sensor data [77].

3.3.1 GIS and Mobile Robotics

Geographic information systems (GIS) are databases that spatially register a wide variety of data products. Airborne and spaceborne remote sensing instruments feed data products, such as high-resolution imagery, digital elevation models, and spectral data into maps registered to GPS locations. GIS outputs allow users to extract that data for specific locations.

Digital soil mapping and modelling (DSMM) is the combination two practices: digital soil mapping (DSMa) and digital soil modelling (DSMo). DSMa is the collection of spatial and temporal soil data compiled into a map [77]. DSMo takes the spatial and temporal data to formulate a soil model that can be used for both prediction and simulations [78].

Hyperspectral imaging provide data for input into surface mineralogy maps at spatial resolutions of 2-4 m for low-altitude aircraft, 20 m for high-altitude aircraft, and 30 m for low-

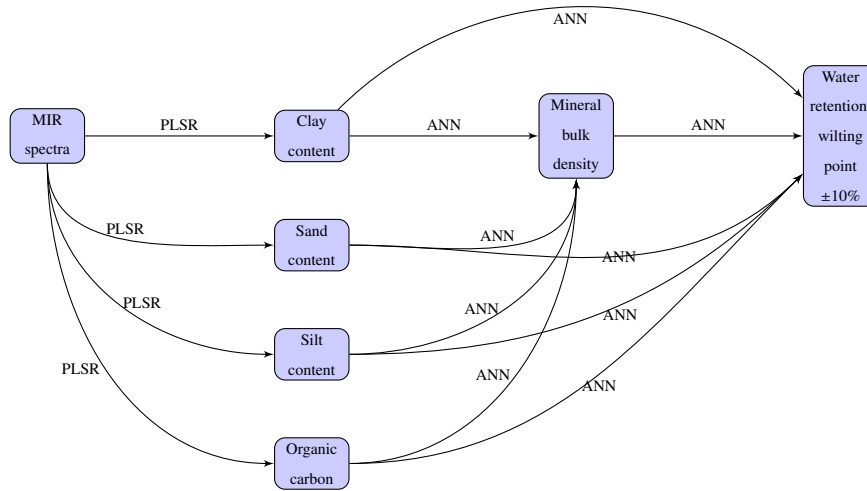


Figure 3.3: An example of SINFERS in which water retention is inferred from MIR spectra. The MIR spectra is the sensed soil values from which clay, sand, silt, and organic carbon content are derived through partial least squares regression. A trained artificial neural network takes in those contents and infers the mineral bulk density. A second ANN then takes the five intermediate values to infer water retention.

Earth-orbiting spacecraft [79]. The spectral resolution for these imagers is 10 *nm* over the 400-2500 *nm* spectral range, which corresponds to visible-near infrared (VNIR) and short-wave infrared (SWIR) ranges. The spectral reflectance within these ranges correspond to iron minerals (Fe^{+2} and Fe^{+3}) such as hematite, goethite, jarosite, and minerals containing anion groups Al-OH, Mg-OH, Fe-OH, Si-OH, CO_3 , NH_4 and SO_4 , such as clays, carbonates, micas, and sulfates. Quartz, and other silicates, appear in the 8000-14,000 *nm* long-wave infrared (LWIR) spectral range [79].

Suvinen [80] applied *a priori* GIS data to a terramechanics model to simulate mobility maps for manned forestry vehicles. The GIS data included digital road maps, topographic and elevation maps, land cover and forest classification maps, land use maps, soil type data, and tree data. The resolution of the maps varied from 10×10 *m* for the land use maps up to the 2 *ha* for the soil type maps. Suvinen [73] also used vehicle data, along with GPS data, to create an on-the-go estimates of vehicle mobility. He suggests that mobility mapping can thus be

improved by linking the *a priori* digital maps with on-the-go mobility estimates.

Hohmann [81] estimated the performance of manned ground vehicles using GIS data such as soil and vegetation maps, geographic maps, and digital elevation maps, as well as meteorological data, which would influence the soil moisture over time. The GIS data fed into a vehicle mobility estimator to create a speed map for various vehicles. The speed map provided the maximum likely speeds attainable for the vehicle across the mapped region.

Park [82] used *a priori* GIS data for path planning of autonomous ground vehicles (UGV). The data contains a set of features, such as roads, vegetation, and topography, which were assigned costs. These costs did not explicitly consider the vehicle's terramechanics model, other than that 'paved roads' were preferred to 'grass land', which was itself preferred to 'marsh swamp area'.

Lichtenberg compared spectral data obtained in orbit from Mars Express to surface data collected locally from *Spirit* to conclude that the data sets are self-consistent [83]. The locally collected data thus improves the confidence of the *a priori* GIS data. Lichtenberg later states in regards to *Spirit*'s immobilization "... that despite careful analysis of orbital data over future landing sites, the surface below the top few centimetres must be treated as an unknown quantity when attempting to forecast a rover's drive performance [84]". This statement implies that rover mobility cannot rely solely on remote sensing. Proximal terrain assessment may be considered.

3.4 Traversability on Other Planetary Surfaces

The motivation of this thesis is derived from planetary exploration. Wong [85] showed that the tractive performance of a rigid wheeled rover on extraterrestrial terrain could be predicted from analysis of the same rover on terrestrial terrain. Past landed missions to both the moon and Mars have made efforts to characterize the local terrain in terms of terramechanical properties. Results from the Mars Pathfinder *Sojourner* in-situ regolith tests characterized Martian regolith to be similar to clayey silt with embedded sands, granules, and pebbles [86, 87]. Lunar regolith

is characterized as a mixture of rock fragments, mineral fragments, breccias, agglutinates, and glass. The proportion of each varies across the surface.

3.4.1 Mars Terrain Parameter Estimation

Past Mars exploration missions have conducted experiments to estimate the cohesion and shearing resistance angle. However, those experiments were conducted while the rover was stationary. Results from the Mars Pathfinder *Sojourner* in-situ regolith tests characterized Martian regolith to be similar to clayey silt with embedded sands, granules, and pebbles [86, 87]. *Sojourner* was used as a test platform to conduct in-situ experiments to determine the cohesion and friction angle of the regolith. The tractive force for a single wheel was determined from the wheel torque that was taken as a function of drawn motor current and no-load current. The rover team took the currents to be a function of temperature. The shearing resistance angle ϕ was assumed to be the same as the angle of repose Ψ that was estimated from camera images. They estimated the cohesion c from the Mohr-Coulomb criteria using the least squares method; wheel slip was not taken into account.

The MER team conducted in-situ experiments to estimate the local cohesion and shearing angle with both *Spirit*, at Gusev Crater, and *Opportunity* at Meridiani Plains. The engineering data used for the estimation included temperature, motor voltages, motor currents, vehicle orientation, and the rocker-bogie positions. Data was recorded at 8 *Hz* during the wheel's commanded rotation of 0.3 *rad/s*. The collected data was used to solve the Mohr-Coulomb criteria $\tau = c + \sigma \tan \phi$. The friction angle was estimated from wheel-digs into the tailings; the tailings are loose terrain that has its cohesiveness destroyed from prior wheel action.

In addition to rovers, Mars regolith parameters have been estimated in-situ by the *Viking* and *Phoenix* landers using narrow blades [88] and robotic scoops [89] for digging trenches. For both landers, camera images and motor feedback were required for estimating the parameters [88, 89].

Mars terrain was given labels for different conditions that were encountered. *Viking* [88] measured different terrain values that were labelled 'Drift material', 'Crusty to Cloddy Ma-

terial', and 'Blocky Material'. *Spirit* and *Opportunity* encountered terrain during traverses that were labelled 'Fine-grained', 'Sandy', 'Rocky', 'Smooth Plains', 'Plains', and 'Aerolian Ripples' [90].

3.4.2 Lunar Regolith Parameters

Both NASA and Soviet Lunar programs, including Luna, Surveyor, and Apollo, studied the physical properties of Lunar regolith in-situ. Additional returned samples were studied on Earth however those samples had limitations due to the manner in which they were transported back to Earth. The geotechnical properties studied were particle size and shapes, density, porosity, compressibility, permeability and diffusivity, bearing capacity, shear strength slope stability and traversability [91].

Traversability over lunar regolith was studied from the eight-wheeled *Lunokhod* rover and the four-wheeled Apollo Lunar Roving Vehicle (LRV). The LRV cruised at an average speed of 6-7 *km/hr* with a total load of over 700 *kg*. Wheel-slip was estimated to be 2-3%. The soil compaction resistance was estimated by comparing the actual and estimated energy consumption of the LRV [91]. Costes [48] studied lunar regolith simulants to estimate pressure-sinkage and shear parameters. The parameters of the simulants are in the same range as terrestrial sand.

The surface the LRV and *Lunokhod* traversed was classified as medium - dense a few centimetres below the surface. The *Lunokhod* wheels were observed to sink only a few centimetres in these conditions. However, both the LRV and *Lunokhod* encountered patches of loose, soft regolith. *Lunokhod* was observed to sink 20 *cm* in this regolith [91].

Chapter 4

Data Analysis and Classification

This chapter provides a brief background on the data analysis and classification methods that are used in Chapter 6. These methods are used for creating feature vectors from acquired data that are used by the classifiers. The background includes wavelet image analysis, Bayesian probability and Naive Bayes classification, and Support Vector Machine (SVM) classification.

4.1 Wavelet Image Analysis

This section provides a brief review of discrete wavelet analysis used for creating feature vectors. The general approach is to decompose signals into subcomponents by means of mathematical transforms. The basis of these transforms are wavelets, which consist of fluctuating non-zero values that sum to zero. This thesis uses discrete Daubechies wavelet transforms to decompose 2-D signals into both running average and running difference signals which are then used as feature vectors for classification. The Haar wavelet is the simplest waveform to introduce, and the Daubechies wavelets are similarly formulated.

4.1.1 Haar Wavelet

The Haar wavelet decomposes a discrete signal into two sub-signals: trend and fluctuations. The trend signal represents the running average of successive pairs of values within the sig-

nal, and is also a low-pass filter. The fluctuation signal represents the running difference of successive pairs, and is also a high-pass filter. A discrete signal f of N values is given as

$$f = f_1, f_2, \dots, f_N \quad (4.1)$$

where N is an even number. The trend signal a is the mean of successive pairs multiplied by $\sqrt{2}$:

$$a = \frac{f_1 + f_2}{\sqrt{2}}, \frac{f_3 + f_4}{\sqrt{2}}, \dots, \frac{f_{N-1} + f_N}{\sqrt{2}}, \quad (4.2)$$

and the fluctuation signal d is the half difference of successive pairs multiplied by $\sqrt{2}$:

$$d = \frac{f_1 - f_2}{\sqrt{2}}, \frac{f_3 - f_4}{\sqrt{2}}, \dots, \frac{f_{N-1} - f_N}{\sqrt{2}}, \quad (4.3)$$

A first level Haar transform maps a discrete input signal into output first trend and first fluctuation sub-signals through the mapping

$$\mathbf{f} \xrightarrow{\mathbf{H}_1} (\mathbf{a}^1 | \mathbf{d}^1) \quad (4.4)$$

and an inverse transform reconstructs the original signal.

The Haar transform conserves the energy ε_f of the signal f , where the energy is sum of the squared values

$$\varepsilon_f = f_1^2 + f_2^2 + \dots + f_N^2 \quad (4.5)$$

$$\varepsilon_a = a_1^2 + a_2^2 + \dots + a_M^2 \quad (4.6)$$

$$\varepsilon_d = d_1^2 + d_2^2 + \dots + d_M^2 \quad (4.7)$$

where M is the length of the sub-signal, and $\varepsilon_f = \varepsilon_{(a^1 | d^1)}$. Energy in the trend ε_a can be dominant when compared to the energy in the fluctuations ε_d .

Successive levels of transforms can be performed on the trend values. The first trend is decomposed into the second trend and second fluctuation sub-signals.

$$\mathbf{f} \xrightarrow{H_2} (\mathbf{a}^2 | \mathbf{d}^2 | \mathbf{d}^1) \quad (4.8)$$

The first trend can be reconstructed through an inverse transform of the second trend and fluctuation, and then the original signal f can be reconstructed from the first trend first fluctuation.

The Haar wavelets ($\pm 1/\sqrt{2}$) are the operators that decompose the signal into fluctuations, with the first level wavelets shown as:

$$\begin{aligned} W_1^1 &= \left(\frac{1}{\sqrt{2}}, \frac{-1}{\sqrt{2}}, 0, 0, \dots, 0, 0 \right) \\ W_2^1 &= \left(0, 0, \frac{1}{\sqrt{2}}, \frac{-1}{\sqrt{2}}, \dots, 0, 0 \right) \\ W_3^1 &= \left(0, 0, 0, 0, \frac{1}{\sqrt{2}}, \frac{-1}{\sqrt{2}}, \dots, 0, 0 \right) \\ &\vdots \\ W_{N/2}^1 &= \left(0, 0, \dots, \frac{1}{\sqrt{2}}, \frac{-1}{\sqrt{2}} \right) \end{aligned}$$

and the compact expression for the fluctuations is given as

$$d_m = \mathbf{f} \cdot \mathbf{W}_m^1 \quad (4.9)$$

The Haar scaling signals are the operators that decompose the signal into trends, with the first level operation shown as:

$$\begin{aligned} V_1^1 &= \left(\frac{1}{\sqrt{2}}, \frac{1}{\sqrt{2}}, 0, 0, \dots, 0, 0 \right) \\ V_2^1 &= \left(0, 0, \frac{1}{\sqrt{2}}, \frac{1}{\sqrt{2}}, \dots, 0, 0 \right) \\ V_3^1 &= \left(0, 0, 0, 0, \frac{1}{\sqrt{2}}, \frac{1}{\sqrt{2}}, \dots, 0, 0 \right) \\ &\vdots \\ V_{N/2}^1 &= \left(0, 0, \dots, \frac{1}{\sqrt{2}}, \frac{1}{\sqrt{2}} \right) \end{aligned}$$

and the compact expression for the trend is given as

$$a_m = \mathbf{f} \cdot \mathbf{V}_m^1 \quad (4.10)$$

4.1.2 Daubechies Wavelets

Daubechies transforms are similarly formulated to the Haar transforms with differing scaling signals and wavelets. They provide mapping from signal to trend and fluctuation sub-signals, and the transform can be repeated over successive levels. Energy is also conserved following transformation.

$$\mathbf{D}_1 \mapsto (\mathbf{a}^1 | \mathbf{d}^1) \quad (4.11)$$

The family of Daubechies transforms vary with the number of coefficients within the scaling signal and wavelet. The db1 wavelet is the same as the Haar wavelet ($\pm 1/\sqrt{2}$). The db2 wavelets have 4 fluctuating non-zero coefficients that sum to zero, given as

$$\begin{aligned} W_1^1 &= (\beta_1, \beta_2, \beta_3, \beta_4, 0, 0, \dots, 0, 0) \\ W_2^1 &= (0, 0, \beta_1, \beta_2, \beta_3, \beta_4, \dots, 0, 0) \\ W_3^1 &= (0, 0, 0, 0, \beta_1, \beta_2, \beta_3, \beta_4, \dots, 0, 0) \\ &\vdots \\ W_{N/2-1}^1 &= (0, 0, \dots, \beta_1, \beta_2, \beta_3, \beta_4) \\ W_{N/2}^1 &= (\beta_3, \beta_4, 0, 0, \dots, \beta_1, \beta_2) \end{aligned}$$

where

$$\beta_1 = \frac{1 - \sqrt{3}}{4\sqrt{2}}, \beta_2 = \frac{\sqrt{3} - 3}{4\sqrt{2}}, \beta_3 = \frac{3 + \sqrt{3}}{4\sqrt{2}}, \beta_4 = \frac{-1 - \sqrt{3}}{4\sqrt{2}} \quad (4.12)$$

and the compact expression for the fluctuations is given as

$$d_m = \mathbf{f} \cdot \mathbf{W}_m^1 \quad (4.13)$$

Similarly, the db2 scaling signal has 4 coefficients given as

$$\begin{aligned} V_1^1 &= (\alpha_1, \alpha_2, \alpha_3, \alpha_4, 0, 0, \dots, 0, 0) \\ V_2^1 &= (0, 0, \alpha_1, \alpha_2, \alpha_3, \alpha_4, \dots, 0, 0) \\ V_3^1 &= (0, 0, 0, 0, \alpha_1, \alpha_2, \alpha_3, \alpha_4, \dots, 0, 0) \\ &\vdots \\ V_{N/2-1}^1 &= (0, 0, \dots, \alpha_1, \alpha_2, \alpha_3, \alpha_4) \\ V_{N/2}^1 &= (\alpha_3, \alpha_4, 0, 0, \dots, \alpha_1, \alpha_2) \end{aligned}$$

where

$$\alpha_1 = \frac{1 + \sqrt{3}}{4\sqrt{2}}, \alpha_2 = \frac{3 + \sqrt{3}}{4\sqrt{2}}, \alpha_3 = \frac{3 - \sqrt{3}}{4\sqrt{2}}, \alpha_4 = \frac{1 - \sqrt{3}}{4\sqrt{2}} \quad (4.14)$$

and the compact expression for the trend is given as

$$a_m = \mathbf{f} \cdot \mathbf{V}_m^1 \quad (4.15)$$

Higher-order Daubechies wavelets have increasing number of coefficients, however the structure remains similar to the db1 and db2 formulations.

4.1.3 Two Dimensional Wavelet Transforms

The preceding sections showed wavelet transform on a 1-D signal. Wavelet transforms can be extended to perform analysis on 2-D signals, such as an $M \times N$ image:

$$\mathbf{f} = \begin{pmatrix} f_{1,M} & f_{2,M} & \dots & f_{N,M} \\ \vdots & \vdots & \ddots & \vdots \\ f_{1,2} & f_{2,2} & \dots & f_{N,2} \\ f_{1,1} & f_{2,1} & \dots & f_{N,1} \end{pmatrix} \quad (4.16)$$

A transform on a 2-D signal is performed by a series of 1-D transforms. A 1-D transform is performed on each row of \mathbf{f} that results in an intermediate 2-D signal. Then 1-D transforms are performed on each column of the intermediate signal. The result is four 2-D sub-signals; in the case of an image the result is four sub-images:

$$\mathbf{f} \mapsto \begin{pmatrix} \mathbf{h}^1 & \mathbf{d}^1 \\ \mathbf{a}^1 & \mathbf{v}^1 \end{pmatrix} \quad (4.17)$$

where \mathbf{a}^1 represents the trend of the image, which is a lower resolution version of the original; \mathbf{v}^1 represents the vertical fluctuations of the image; \mathbf{h}^1 represents the horizontal fluctuations of the image; and \mathbf{d}^1 represents the diagonal fluctuations.

As in the 1-D case, a 2-D trend signal can undergo a transformation to successive levels. The first trend transforms to the second trend and fluctuations:

$$\mathbf{a}^1 \mapsto \begin{pmatrix} \mathbf{h}^2 & \mathbf{d}^2 \\ \mathbf{a}^2 & \mathbf{v}^2 \end{pmatrix} \quad (4.18)$$

As in the 1-D case, a 2-D signal has energy equal to the sum of the square of the values, and that energy is conserved following transformation.

4.2 Bayesian Probability

For this thesis probability is separated into relative frequency and Bayesian approaches. Probability theory is concerned with the outcomes of events within a sample space. This section provides a brief review of probability theory with a focus on Bayesian probability.

Let us take a set of sixty numbered and coloured tiles. The colours are red (R), orange (O), yellow (Y), green (G), blue (B), and purple (P). There are ten tiles for each of the six colours. Within each set the tiles are numbered from one to ten. There are sixty unique tiles in total, six different coloured tiles for each number, and ten different numbered tiles for each colour.

The set of tiles represents a sample space Ω , with each tile representing an element e in that sample space. Here,

$$\Omega = \{e_1, e_2, \dots, e_n\} \quad (4.19)$$

where in the case of the set of tiles $n = 60$. Selecting a tile at random represents a single event. The probability of a specific outcome to that event is denoted as $P(e_i)$ where:

$$0 \leq P(e_i) \leq 1 \text{ for } 1 \leq i \leq n \quad (4.20)$$

Selecting a tile at random has 60 possible outcomes as there are 60 distinct tiles. The probability of selecting a specific tile is 1 outcome out of a possible 60, given as:

$$P(e = B5) = \frac{1}{60} \quad (4.21)$$

where $B5$ is the Blue-5 tile, which is 1 specific outcome within a set of 60 possible outcomes for a single event. The probability of selecting any tile is the sum of the individual probabilities of each outcome:

$$P(E) = P(e_1) + P(e_2) + \dots + P(e_n) = 1 \quad (4.22)$$

In other words, there will always be some outcome given this event. The probability of other outcomes follow a similar relation. The probability that the selected tile will be blue is $P(e = B) = \frac{1}{6}$, and the probability that the selected tile will be any '5' is $P(e = 5) = \frac{1}{10}$ for this set of tiles. The probability of selecting either the Blue-5 or Red-5 is the sum of the two probabilities:

$$P(e = B5 \cup R5) = P(e = B5) + P(e = R5) = \frac{1}{30} \quad (4.23)$$

where $B5 \cap R5 = \emptyset$, as there is no 5 tile that is both a red and blue. However, the probability of selecting either a blue or a 5 tile:

$$P(e = B \cup 5) = P(e = B) + P(e = 5) - P(e = B5) = \frac{1}{6} + \frac{1}{10} - \frac{1}{60} = \frac{1}{4} \quad (4.24)$$

as $P(e = B5)$ is already contained in $P(e = B)$ and $P(e = 5)$.

In this set of 60 tiles there are 30 odd-numbered tiles. The probability of selecting an odd-numbered tile O is then $P(e = O) = \frac{30}{60} = \frac{1}{2}$. The 5-tiles are contained within the odd-numbered set, and $P(e = 5 \cap O) = \frac{1}{10}$. If the selected tile is an odd number, then the probability of that tile being a 5 conditioned on that tile being an odd number is given as:

$$P(e = 5|O) = \frac{P(e = 5 \cap O)}{P(e = O)} = \frac{\frac{1}{10}}{\frac{1}{2}} = \frac{1}{5} \quad (4.25)$$

which is the probability that a 5 is selected from a set of odd-numbered tiles. If the selected tile is blue, then the probability of that card being a 5 conditioned on that tile being blue is given as:

$$P(e = 5|B) = \frac{P(e = 5 \cap B)}{P(e = B)} = \frac{\frac{1}{60}}{\frac{1}{6}} = \frac{1}{10} \quad (4.26)$$

which is the same probability that a 5 is selected independent of that tile being blue. The knowledge that the tile is odd-numbered increases the probability that the tile is a 5, however the knowledge that the tile is blue does not, which means 5 and blue are independent events.

Selecting any one from a subset of tiles, $E = \{R5, B5, R2\}$ has probability $P(E) = \frac{3}{60}$ and another subset of tiles, $F = \{R5, P5, R2\}$ has probability $P(F) = \frac{3}{60}$. E and F share two of the sixty tiles: $P(E \cap F) = \frac{2}{60}$. The probability of selecting one of the tiles in the subset E after knowing that the tiles of F have been selected is given as:

$$P(E|F) = \frac{P(E \cap F)}{P(F)} = \frac{\frac{2}{60}}{\frac{3}{60}} = \frac{2}{3} \quad (4.27)$$

Here, knowing that the tiles of F have been selected increases the probability that a tile from E is selected, which means that E and F are not independent. Another subset of tiles $G = \{R5, B5, P5, Y5\}$ had probability $P(G) = \frac{4}{60}$ that any one that subset is selected. If the tiles of G are selected, then the probability that a tile from E is selected is given as:

$$P(E|G) = \frac{P(E \cap G)}{P(G)} = \frac{\frac{2}{60}}{\frac{4}{60}} = \frac{1}{2} \quad (4.28)$$

Similarly, E and G are not independent. Taking the common tiles from both F and G gives $(F \cap G) = \{R5, P5\}$ with $P(F \cap G) = \frac{2}{60}$. If have selected the common tiles from E and G , $(F \cap G)$, then the probability of selecting a tile from E knowing $(F \cap G)$ is given as:

$$P(E|F \cap G) = \frac{P(E \cap F \cap G)}{P(F \cap G)} = \frac{\frac{1}{60}}{\frac{2}{60}} = \frac{1}{2} \quad (4.29)$$

where there is only 1 common tile amongst E , F and G . Thus, knowing F and G does not improve the probability from just knowing G , which means that E and F are independent conditioned on G .

4.2.1 Frequentist Approach

In the set of numbered coloured tiles, the probability of a specific tile $R5$ being selected was given as $P(e - R5) = \frac{1}{60}$ which is based on the knowledge that there were 60 distinct tiles in the sample space Ω . If Ω was not known, a random tile selection test could be repeated many times to find the frequency at which $R5$ was selected. In other words, the frequentist approach to finding the probability of a specific outcome to an event is to repeat an event many times. If the tile selection event is performed 10,000 times, and the outcome $R5$ occurs 160 times, then the frequency at which $R5$ occurs on the unknown sample space Ω is 0.016. The probability that the outcome $R5$ occurs on the next event is then 0.016, which is similar to $P(e - R5) = \frac{1}{60}$ when the size of the sample space is known. Furthermore, the frequency of all possible outcomes, and thus sets of outcomes, can also be determined through repetition.

This approach is useful when it is possible to repeat an event to come up with the frequency at which a specific outcome occurs. However, this approach is not useful when repeating an event many times, or at all, is not possible.

4.2.2 Bayesian Approach

The Bayesian approach is to assign the probability of an outcome given some knowledge that is based on the probability of that knowledge for a given outcome. The basic Bayesian formu-

lation is given as:

$$P(E|F) = \frac{P(F|E)P(E)}{P(F)} \quad (4.30)$$

Using the coloured tile analogy, if F is a blue tile, and E is a five tile, then $P(E|F)$ is the probability of getting a 5 conditioned on knowing that the tile is blue. $P(F|E)$ is then the probability of a blue tile conditioned on knowing that it is a 5. There are six different 5 tiles, so $P(F|E) = \frac{1}{6}$. The probability of a 5 $P(E)$ is the prior belief in the probability that a 5 tile is selected.

Here, finding $P(F)$ is the sum of possible conditional outcomes:

$$P(F = B) = P(F = B|E = 1)P(E = 1) + P(F = B|E = 2)P(E = 2) + \dots + P(F = B|E = 10)P(E = 10) \quad (4.31)$$

If the prior beliefs are $P(E = 1, 2, \dots, 10) = \frac{1}{10}$, then:

$$P(F = B) = \frac{1}{6} \frac{1}{10} + \frac{1}{6} \frac{1}{10} + \dots + \frac{1}{6} \frac{1}{10} = \frac{1}{6} \quad (4.32)$$

which is the probability that a tile is blue. Then the Bayesian formulation becomes:

$$P(E|F) = \frac{P(F|E)P(E)}{P(F)} = \frac{\frac{1}{6} \frac{1}{10}}{\frac{1}{6}} = \frac{1}{10} \quad (4.33)$$

which is the probability of a tile being 5 if blue is selected. This is a trivial solution as there are exact prior beliefs.

The basic Bayesian approach in Equation 4.30 is useful when considering sensed data. As stated before, the basic formulation is to assign the probability of an outcome given some knowledge that is based on the probability of that knowledge for a given outcome. For example, the probability of an obstacle existing given lidar data is based on the probability that the lidar would show a obstacle if it indeed existed. It also requires prior belief that an obstacle would exist in the first place. The Bayesian formulation therefore relies on the quality of the collected data and any prior beliefs.

Let us say we have a mobile robot equipped with a lidar for detecting geometric obstacles at a distance. The mobile robot is operating in the desert and the prior belief that there will be such obstacles in this location is 0.05. The lidar data provides a binary response of ‘obstacle’ or ‘no obstacle’. This particular lidar has a false negative rate of 0.1, and a false positive rate of 0.01. The probabilities for obstacle detection are given as:

$$P(L = pos|O = pres) = 0.9 \quad (4.34)$$

$$P(L = pos|O = abs) = 0.01 \quad (4.35)$$

$$P(L = neg|O = pres) = 0.1 \quad (4.36)$$

$$P(L = neg|O = abs) = 0.99 \quad (4.37)$$

If the lidar indicates that an obstacle is detected, the Bayesian formulation allows for the probability that the obstacle is actually there:

$$P(O = pres|L = pos) = \frac{P(L = pos|O = pres)P(O = pres)}{P(L = pos|O = pres)P(O = pres) + P(L = pos|O = abs)P(O = abs)} \quad (4.38)$$

$$P(O = pres|L = pos) = \frac{0.9 \times 0.05}{0.9 \times 0.05 + 0.01 \times 0.95} \quad (4.39)$$

$$P(O = pres|L = pos) = \frac{0.045}{0.045 + 0.0095} = 0.83 \quad (4.40)$$

Based on the single lidar data point and prior beliefs, the probability that the obstacle is really there is 0.83. If a new lidar measurement from the same distance obstacle comes back positive again, the prior probability of 0.83 becomes the new belief that an obstacle is present, and the update to the probability is given as:

$$P(O = pres|L = pos) = \frac{P(L = pos|O = pres)P(O = pres)}{P(L = pos|O = pres)P(O = pres) + P(L = pos|O = abs)P(O = abs)} \quad (4.41)$$

$$P(O = pres|L = pos) = \frac{0.9 \times 0.83}{0.9 \times 0.83 + 0.01 \times 0.17} \quad (4.42)$$

$$P(O = pres|L = pos) = \frac{0.747}{0.749} = 0.997 \quad (4.43)$$

and the probability of there being an obstacle given another positive lidar measurement has now increased to 0.997. Conversely, if the second measurement came back as there being no obstacle, the probability can be updated:

$$P(O = pres|L = neg) = \frac{P(L = neg|O = pres)P(O = pres)}{P(L = neg|O = pres)P(O = pres) + P(L = neg|O = abs)P(O = abs)} \quad (4.44)$$

$$P(O = pres|L = neg) = \frac{0.1 \times 0.83}{0.1 \times 0.83 + 0.99 \times 0.17} \quad (4.45)$$

$$P(O = pres|L = pos) = \frac{0.083}{0.251} = 0.33 \quad (4.46)$$

which reduces the belief that the obstacle exists.

4.3 Classification

Classification problems are often assigned one of two types: discrimination and clustering. Discrimination seeks to assign a feature vector \mathbf{x} to one of C classes. Clustering seeks to group similar feature vectors \mathbf{x} together without prior classes. For this thesis the objective is to assess the addition of lidar reflectance and spectral features to optical image features when classifying known terrain types. Two methods of discrimination, or supervised learning, are presented here: Naive Bayes (NB) and Support Vector Machines (SVM). NB classifiers assume an underlying probability density function of a feature vector for a given class. SVM classifiers develop discriminant boundaries between given classes [92].

4.3.1 Naive Bayes Classification

One application for Bayesian probability is supervised classification. The basis for the Naive Bayes classifier is Equation 4.30, where E is a set of possible classes and F is a vector of observed features. $P(E|F)$ becomes the *a posteriori* probability of a class $E = e_c$ for a given vector of feature F . The classifier finds the class that results in the maximum *a posteriori* probability from a given vector of features. To find $P(E|F)$, $P(F|E)$ must first be estimated for every class

$$P(F|e_c) = \prod_{j=1}^d P(f_j|e_c) \quad (4.47)$$

where the *naive* assumption is that a particular feature f_j in vector f is independent of the occurrence of other features f_j for a particular class. $P(E = e_c)$ is the prior probability of a given class. $P(F)$ is typically ignored as it will be the same for all classes [93, 94].

4.4 Support Vector Machine classification

Support Vector Machines (SVM) are a type of discriminant function, which seek to separate classes by a function $g(x)$. For the two-class data problem, SVM classifiers construct a maximal margin hyperplane to separate both classes of data. A simple example of SVM classification is the two-class data problem, with n sets of training patterns $x_i, i = 1, \dots, n$. Each training pattern or feature is assigned a class w_1 or w_2 with a corresponding value, $y_i = \pm 1$. The discriminant boundary between the two classes of data is:

$$g(\mathbf{x}) = \mathbf{w}^T \mathbf{x} + w_0 \quad (4.48)$$

where \mathbf{w} is a weight vector and w_0 is a threshold. The decision rule for this function is given as:

$$\mathbf{w}^T \mathbf{x} + w_0 \begin{cases} > 0 \\ < 0 \end{cases} \Rightarrow \mathbf{x} \in \begin{cases} w_1, y_i = +1 \\ w_2, y_i = -1 \end{cases} \quad (4.49)$$

If $y_i(\mathbf{w}^T \mathbf{x} + w_0) > 0$ for all i , then all training patterns are correctly classified as w_1 (with value $y_i = +1$) or w_2 (with value $y_i = -1$).

Hyperplane function $g(x)$ separates the two classes of patterns, and it is desired to have a maximal margin between the two classes. The two canonical hyperplanes $H_1 : \mathbf{w}^T \mathbf{x} + w_0 = +1$ and $H_2 : \mathbf{w}^T \mathbf{x} + w_0 = -1$ are separated from the hyperplane function $g(x)$ by $1/|\mathbf{w}|$, and the margin between the two hyperplanes is $2/|\mathbf{w}|$. Maximizing the margin results in patterns x_i that lie on the canonical hyperplanes, which are called the support vectors (SV). To maximize the margin between the two classes of patterns requires a minimization of $|\mathbf{w}|$:

$$y_i(\mathbf{w}^T \mathbf{x} + w_0) \geq 1 \quad (4.50)$$

which can be solved as an optimization problem. The primal form of the objective function L_p :

$$L_p = \frac{1}{2} \mathbf{w}^T \mathbf{w} - \sum_{i=1}^n \alpha_i (y_i (\mathbf{w}^T \mathbf{x}_i + w_0) - 1) \quad (4.51)$$

where $\alpha_i, i = 1, \dots, n; \alpha_i \geq 0$ are Lagrange multipliers. Differentiating L_p with respect to w_0 and \mathbf{w}

$$\frac{\partial L_p}{\partial w_0} = 0 \quad (4.52)$$

$$\frac{\partial L_p}{\partial \mathbf{w}} = 0 \quad (4.53)$$

$$L_D = \sum_{i=1}^n \alpha_i - \frac{1}{2} \sum_{i=1}^n \sum_{j=1}^n \alpha_i \alpha_j y_i y_j \mathbf{x}_i^T \mathbf{x}_j \quad (4.54)$$

which is the dual form of the Lagrangian. Support vectors have nonzero Lagrange multipliers. When α_i have been obtained, w_0 can also be obtained using one of the n_{SV} support vectors. With \mathbf{w} and w_0 , new patterns \mathbf{x} can be assigned a class given by the sign of:

$$\mathbf{w}^T \mathbf{x} + w_0 \quad (4.55)$$

The above process works when the two classes of patterns can be linearly separated. Slack variables ξ are introduced to relax the separation conditions when patterns are linearly non-separable. Alternatively, nonlinear SVM can be used that introduce discriminant functions that are nonlinear:

$$g(\mathbf{x}) = \mathbf{w}^T \phi(\mathbf{x}) + w_0 \quad (4.56)$$

and new patterns \mathbf{x} can be assigned a class given by the sign of:

$$g(\mathbf{x}) = \sum_{i \in SV} \alpha_i y_i \phi^T(x_i) \phi + w_0 \quad (4.57)$$

The transformed feature space $\phi(x)$ can be avoided using a kernel function $K(x, y) = \phi^T(x)\phi(y)$, which results in a discriminant function:

$$g(\mathbf{x}) = \sum_{i \in SV} \alpha_i y_i K(x_i, x) + w_0 \quad (4.58)$$

where the kernel may be one of many types depending on the non-linearity.

In many cases there are more than two classes to discriminate. Multi-class SVMs can be constructed from one of the following frameworks:

- One-against-all where there are C binary classifiers for C classes, which can lead to patterns belonging to more than 1, or 0, classes;
- One-against-one where there are $C(C - 1)/2$ binary classifiers, and each classifier discriminates between two classes. A new pattern is passed through each classifier and voting system determines the class, which can lead to no clear decision; and
- Define C discriminant functions $g_1(\mathbf{x}), \dots, g_C(\mathbf{x})$ where \mathbf{x} is assigned to a class whose discriminant function is the largest value at \mathbf{x} .

Chapter 5

Human Performance in Tele-Operation

This chapter provides a review of previous works in tele-operation, tele-operation over time delay, and human performance in tele-operation. An objective of this thesis is to assess the human performance in remotely operating a mobile robot in poor lighting conditions over time delay. This chapter is divided into a general background on tele-operation over time-delay, Fitts' Law and its use in human performance studies, and past works in tele-operation of mobile robots and tele-operation over time delay.

5.1 Tele-Operation

Tele-operation is broadly defined as 'doing work at a distance'. The scope can encompass a wide range of applications, from a remote controlled toy car to collecting interstellar science data with *Voyager 1*. The former involves the human operator providing real-time commands via radio signals that are received and implemented by the device. The later involves the human operator providing an instruction set, which is uploaded to the device via an interplanetary communication network. The instruction sets are constructed off-line and sent when possible, and the device is able to function autonomously in between instruction sets. These two examples are scenarios in which the operator is not dependent upon real-time feedback along the communication path. The remote controlled car is typically in the visual range of the op-

erator. *Voyager 1*'s operations are not real-time; after the instruction set is sent to *Voyager 1* confirmation feedback takes at least 34 hours due to the round-trip time delay.

A closed system is one in which the control input to the system is dependent upon the feedback from the output of the system. The output signal is generally assumed to instantaneously feed back to the controller, either a human operator or computer. For many applications this can be an acceptable assumption when controllers, actuators and sensors are all connected together. When the actuators and sensors are separated from the controller and the signals are transmitted over the separated distance, round-trip delays creep into the closed system. The observed system state, as provided by sensors, when received by the controller no longer corresponds to the true system state. In other words, the controller receives system state $x(t)$ when it is now $x(t+n)$. The controller develops an input $u(t+n)$ based on this system state. The actuator receives control input $u(t+n)$, which is based on observed state $x(t)$, for the system that is now at $x(t+n+m)$. In reality, this time delay always occurs though often does not result in control issues; the system is stable enough to accept slight variations in control input relative to the system state. For this thesis, time-delayed tele-operation refers to the control of a robotic or mechatronic system by a human operator who is physically and spatially separated from that system, the operation is dependent upon feedback being received along the same communication path, and the round-trip time delay is considered to be non-trivial.

For this thesis, time-delayed tele-operation refers to the control of a robotic or mechatronic system by a human operator who is physically and spatially separated from that system, the operation is dependent upon feedback being received along the same communication path, and the round-trip time delay is considered to be non-trivial. Examples of this scenario, both Earth-based and space-based, are provided in the following sections. Earth-based applications include remotely operated robotic surgical tools and unmanned underwater vehicles (UUVs). Space-based applications, discussed in Chapter 2, are focused on the operation of robotic systems on the moon including past lunar missions, and recent analogue operations concepts.

5.1.1 Earth-Based Applications

The scope of this thesis has been narrowed to the control of a robotic or mechatronic system by a human operator who is physically and spatially separated from that system. For Earth-based application this is still a wide ranging field. Remote systems are typically operated in environments that pose risks to humans, such as underground mining [95], explosive disarmament [96], and indoor search and rescue [97]. Remote systems are also deployed to environments that are difficult for humans to operate in, such as underwater [98, 99, 100]. Remotely operated manipulators that require fine control, such as tele-operated surgical instruments, are examples of systems that are particularly sensitive to, and require techniques to compensate for, time delays [96].

Underwater vehicles experience time delays in their tele-operation due to acoustics underwater and are thus an analogue to tele-operating a lunar rover. Underwater vehicles use acoustic telemetry when towing long, heavy cables is impractical. The speed-of-sound through water is 1700 m/s so a vehicle operating 2 km beneath the surface will experience more than 2 s of round-trip time delay [20]. When additional communication relays are considered, this delay increases. Acoustic modems have limited available bandwidth and thus restrict the amount of telemetry sent back to the operator to 10 kbits/s [100], though that bandwidth decreases with depth. At the depths to which underwater vehicles are deployed, the lighting and visibility is poor and requires an active light source [98].

Lin [98] demonstrated that for underwater remotely operated vehicles (ROV) a virtual 3D environment aided in the safe-guarded tele-operations. The virtual reality (VR) interface interpreted feedback from the ROV and the 3D rendered environment was updated, based on the known model of the ROV and prior data points. This interface scheme was also useful for scenarios in which the communication link was a fixed cable instead; the 3D VR interface would allow the operator to know the location of the tether to avoid entanglement. For the time-delayed scenario, the VR model interface projected the predicted pose of the ROV in the 3D rendered environment to assist the operator. The ROV itself could detect obstacles to stop itself from crashing into them. Sayers [100] further studies the effect of time-delayed

operations of a ROV with a manipulator arm. Similarly the tele-operator is provided with sufficient representation of the environment to aid the operation, however the operations themselves are safe-guarded. Although Lin [98] did not specify a bandwidth, Sayers [100] reported the successful safe-guarded tele-operations of their ROV at 0.5 FPS to meet the 10 *kbits/s* limit. Sayers [100] recommendations for undersea ROV tele-operations was to avoid the direct-drive approach as time delays magnify the costs of errors, and that the system must be able to cope with unexpected losses in transmission.

The remotely operated robotic arms mentioned above face latencies of 5 s or greater. More common are robotic arms that require stable closed-loop control in a master-slave configuration with lower latency [101]. The remote operator perceives the manipulator to be responding in real-time as if they were physically present with it. However, the latency is great enough to cause instability in the control, which is particularly hazardous in the case of tele-surgery.

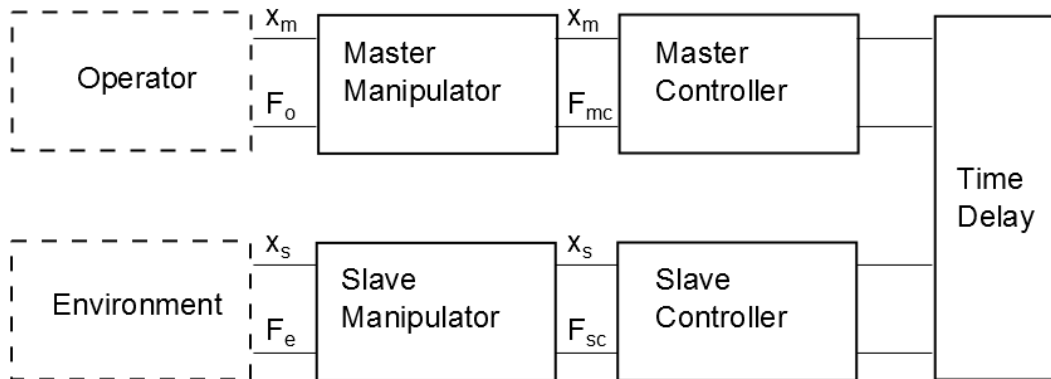


Figure 5.1: Teleoperation control scheme for remote manipulator. The operator applies a force (F_o) to a local master manipulator; the pose of the manipulator is determined through the forward kinematics of the joint positions by the master controller (F_{mc}) and sent to the slave controller. The slave controller applies forces (F_{sc}) to assign the joint positions the slave manipulator such that it can interact with its environment (F_e). State feedback (x_s) of the slave manipulator is transmitted back to through the master manipulator (x_m) to the operator. Adapted from [101].

5.1.2 Space-Based Applications

Space-based applications, discussed in Chapter 2, are focused on tele-operating a rover on the moon from Earth in this thesis. It is imagined that at some time mobile robots, and any robotic hardware, on planetary surfaces will be autonomous. In the near term, humans will remain in the control loop and remain in direct control of the robotic hardware. The European Space Agency has developed the multipurpose end-to-end robotic operations network (METERON) [102] as a means of remotely operating robotic hardware from orbit. It has been tested from the International Space Agency, where a user remotely controlled a mobile robot in a test yard. The intention is to use such a network in future missions where humans will operate landed robotic hardware from an orbiting facility, such as remotely controlling operating robotic equipment on the Moon from lunar orbit. The METERON development can be inferred to mean that when humans return to the moon or go to Mars, it is believed that humans will remain in the control loop as autonomy will not yet overtake human control.

5.2 Human Performance and Fitts' Law

This section reviews Fitts' Law and its use in human performance evaluation. Fitts' Law is a human psycho-motion model based on Shannon's communication theory [103], which has since been applied to human-computer interaction (HCI) [104]. Fitts' Law was first studied in human-computer interaction with the evaluation of different text selection schemes on a computer display [105]. It has since been applied to a wide range of HCI scenarios, including tele-operation of remote manipulators under time-delayed target selection [106].

5.2.1 Fitts' Law Formulation and HCI

Fitts' Law is based on Shannon's communication theory of information capacity [104]. An information channel is a medium, subject to perturbation, through which a signal passes, and the information capacity, C , is the rate at which that signal can pass. Shannon's information

capacity of a channel is a function of the strength of the signal S , the strength of the perturbing noise N , and the channel's bandwidth B :

$$C = B \log_2 \frac{S + N}{N} \quad (5.1)$$

where C has units of bits/s, and B has units of Hz .

Fitts' work attempted to model human psycho-motion in terms of information capacity. The model states that the information capacity, or index of performance IP , is the ratio of an index of difficulty ID of a task to the movement time MT to complete the task. For a task of given difficulty, the performance is better when completed in lesser time. For a given movement time, the performance is worse when the difficulty of the task increases. ID is analogous to the \log_2 term with units of bits, MT has units of seconds, and IP is analogous to information capacity with units of bits/s.

$$IP = \frac{ID}{MT} \quad (5.2)$$

Fitts psycho-motor task had human subjects tapping between two targets of varying difficulty indexes. For the tapping task ID was a function of target width W , and the target separation distance, or amplitude A . Here, target width is analogous to noise and target separation is analogous to signal. Fitts formulated ID based on Shannon's \log_2 term:

$$ID = \log_2 \frac{2A}{W} \quad (5.3)$$

where both A and W are both distances. For the tapping task, ID increases when the targets are further separated, or the width of the target narrows. The greater the difficulty of the tapping task, the more 'information', in bits, the psycho-motor system must transmit. The faster the movement time MT , the greater the 'information capacity', in bits/s, the psycho-motor system and the greater its performance.

Fitts recorded MT for various A and W values with a number of human subjects. Regressing MT on ID , the expression for MT becomes:

$$MT = a + b \log_2 \frac{2A}{W} \quad (5.4)$$

where a and b are regression coefficients and $\frac{1}{b}$ corresponds to IP .

The index of difficulty formulation has been reevaluated since Fitts' original work. The \log_2 term in Equation 5.3 is not directly analogous to Shannon's \log_2 term. A direct analogy is then to state ID as:

$$ID = \log_2 \frac{A + W}{W} = \log_2 \frac{A}{W} + 1 \quad (5.5)$$

The formulations for ID have all shown utility depending on the values of A and W . Equation 5.5 does not result in negative ID values as $A \rightarrow 0$. Equation 5.4 only shows high correlation when the ratio of A to W is large.

Welford's formulation, shown in Equation 5.6, has shown higher correlation between ID and MT [104] and was used in the first HCI studies [105].

$$ID = \log_2 \left(\frac{A}{W} + 0.5 \right) \quad (5.6)$$

The study was able to formulate a Fitts' Law relationship, using Welford's ID , between the movement time to selecting the text, to the distance from the starting position to the text and the size of the text. This formulation applied to the rate-controlled devices, the mouse and joystick, for the text selection task. For the keyboard methods, the movement time was a function of the number of keystrokes. The study quantified, using Fitts' Law, that the mouse was superior to the joystick in the human performance of text selection on a display using Fitts' Law. The study also showed that the movement time for the mouse was superior to all text selection devices. Mackenzie [107] later reexamined Card's study [105] with the Shannon Formulation to remove the negative index of difficulty values. The results of this reanalysis shows the performance to be closer to current studies using a computer mouse.

5.2.2 Tele-Operation with Time Delay

Sheridan and Ferrel [108, 109] studied remote manipulation with time delay. A single human tester used a master controller to move a slave hand from an initial position to grip a block with transmission delays of 0, 1, 2.1, and 3.2 seconds between the master and the slave [108]. An index of difficulty for the task was established to be

$$ID = \log_2 \frac{2A}{B - C} \quad (5.7)$$

where B was the width of the gripper, C was the variable width of the target blocks, and A was the movement distance between initial gripper position and the target block.

The results showed that the tester adopted a move and wait strategy to cope with the delay. The results of this study showed that the time to complete a task of a given index of difficulty could be predicted for a given time delay t_d :

$$t(ID) = t_o(ID) + (t_r + t_d)N(ID) + t_d \quad (5.8)$$

where $t_o(ID)$ was the task completion time without delay, t_r was a reaction time taken to be 0.2 seconds, and $N(ID)$ was the number of recorded corrective movements.

This experiment was performed again with seven human testers [109] who similarly performed a move and wait strategy which confirmed the previous result. Four human testers then completed a more difficult remote manipulation task over time delay: remotely grasping, moving and manipulating tools. For this task, no index of difficulty was established, and the time to complete the task was recorded for varying time delays. The results from this more complex task showed that the more difficult task with delays could be completed accurately at the expense of completion time.

5.2.3 Human Performance Studies and Mobile Robot Cornering

Fitts' Law studies extended to assessing human performance with different input devices for a text selection task on a computer monitor [105]. Five human subjects were provided four

devices for the task of selecting text on a display. Two devices, a mouse and a joystick, were rate-controlled in that the spatial movement of the device corresponded with the cursor motion on the display. The other two devices, using keyboard keys, were a function of keyboard strokes rather than eye-device coordination. A Fitts' Law-like formulation for movement time for each input method was based on the distance to the target text, and the size of the target text. The mouse resulted in both the lowest movement time and lowest error rate.

Fitts' Law predicts the movement time between two targets assuming a straightforward trajectory. HCI tasks often require a trajectory to be followed, such as navigating through nested menus on graphical user interfaces [110]. A generalized steering law was developed to predict task completion through non-uniform trajectories. Human testers used a stylus on a tablet as an input for drawing on a computer monitor to follow various trajectories: simple goal passing (similar to Fitts' tapping test), goal passing through a tunnel, goal passing through a narrowing tunnel, goal passing through a spiralling tunnel. The generic expression for the index of difficulty for a path C was established as

$$ID = \int_C \frac{ds}{W(s)} \quad (5.9)$$

where $W(s)$ is the width of the tunnel as a function of position s along the path.

The study of negotiating a trajectory was extended to a negotiating a virtual hovercraft around corners in a first-person-shooter gaming environment [111]. Nine human testers steered the virtual hovercraft through corridors of varying widths over successive trial blocks to demonstrate both task learning and to develop a task index of difficulty. In this study the hovercraft passed through one corridor, around a 90° corner into a corridor of equal width to the first. The human tester had a third-person trailing view of the vehicle as they controlled it through the task. The index of difficult was established as a function of the vehicle width p and corridor width w :

$$ID = \frac{p}{(w - p)} \quad (5.10)$$

Examining the limiting cases of Equation 5.10, when the vehicle width is equal the the

corridor width, the task is infinitely difficult, and when vehicle width approaches zero the task becomes trivial. A second trial involving ten human testers and more corridor widths showed that mean completion times increased with decreasing corridor widths, and task errors decreased with increasing corridor width.

The index of difficulty was also derived considering information theory. Pastel [111] assumed the task to be recognizing that the vehicle was sufficiently centred within the corridor to avoid collision. The information gain was presented as a difference of logarithms of the uncertainties before and after the vehicle was centred within the corridor, $\log_2(w) - \log_2(w - p)$. This index of difficulty was thus

$$ID = \log_2 \left(\frac{p}{w - p} + 1 \right) \quad (5.11)$$

where Equation 5.11 above is closely analogous to the Shannon information theory formulation of Fitts' Law in Equation 5.5. The results from Pastel's study showed the cornering times fit the model through linear regression with R^2 values greater than 0.85.

The virtual cornering task was replicated with a real world mobile robot using first-person view [112]. Eighteen human testers tele-operated the mobile robot through a cornering task with three corridor widths. The three corridor widths were repeated three times within a trial block; each human tester performed 5 trial blocks. However, the fifth trial block was removed from analysis. The results showed that the cornering time increased as the corridor width decreased, and the task errors decreased over trial blocks as the human testers learnt the task. A cornering law for UGVs, given in Equation 5.12 is a formulation similar to Fitts' Law, predicts the cornering time for tele-operated mobile robot based on the aperture width and the mobile robot width.

$$CT = a + b \log_2 \left(\frac{p}{w - p} + 1 \right) \quad (5.12)$$

Helton's results showed that the mean cornering times for three difficulty values fit the model given by Equation 5.11 with Pearson r values greater than 0.95.

A tele-operation under time-delay study with a mobile robot [113] showed that deviations

from a fixed path increased with the increase in delay in a simulation environment. The delays varied between 0 and 0.75 second. This increase in deviations was represented by a scoring function given:

$$S_i = \max(0, 1 - |y_i|) \quad (5.13)$$

S_i is the score based on lateral deviation from centreline y_i at step i . Here, the width of the track was $2 m$, therefore the maximum lateral deviation without leaving the track is $1 m$. The average score over all steps n is then:

$$S = \frac{1}{n} \sum_{i=1}^n S_i \quad (5.14)$$

Chapter 6

Terrain Classification

This chapter presents the experimental outcomes of the terrain traversal and classification testing. The objective of this testing is to demonstrate a proof-of-concept in using proximal sensing techniques to assess terrain traversability. The intention is to demonstrate that the combination of visual images, spectral response and lidar reflectance intensity improves terrain classification over just visual classification. The chapter describes the collection process for both the proprioceptive mobile robot data and the proximal terrain data, results of data classification, utilization of classifier for prediction, and an interpretation of the results.

6.1 Experimental Equipment

This section describes the equipment and setup for the terrain traversing testing. Most data collection took place inside the Coudé room of the Elginfield Observatory, and the hyperspectral images were taken off-site. Testing at the observatory included a small mobile robot test platform traversing over various terrain types contained within a box, and lidar reflectance measurements and images were taken of the terrain types.

6.1.1 Terrain Types and Terrain Box

For this thesis a set of terrain types was considered: sand, gravel, crushed clay pottery chips, white quartz aggregate, and pink quartz aggregate. The sand and gravel were derived from the same material. The terrain types were selected based on availability at a garden centre, and the belief that the gravel, clay chips and quartz would spectrally appear different.

A terrain box, shown in Figure 6.1, was constructed in the Coudé room to a size of 122 *cm* by 244 *cm* with a height of 10 *cm*. The various terrain types were filled to a depth of approximately 5 *cm*. The box itself rested upon jacks that could lift one end of the box to increase the inclination of the terrain. The sand was added to the box, and the differing aggregate material was added on top of and removed from the sand.



Figure 6.1: The terrain box contained a layer of sand and additional material was added and removed from it. The box rested on two jacks (right side, not shown) to raise and lower the box to create a 5°incline, shown in Figure 6.2. In this image, the gravel covered the bed with the left side covered in wet sand.

The following list is the set of terrain conditions for which complete, and viable, data was collected for classification purposes:

DLS Dry loose sand

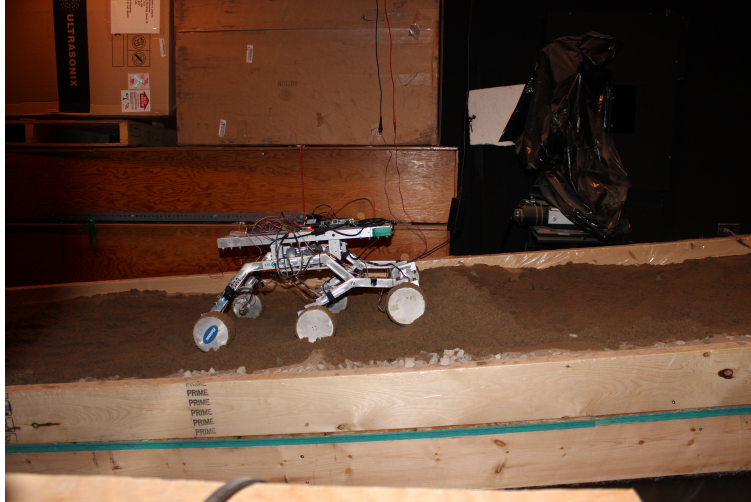


Figure 6.2: One side of the terrain box was raised to create an incline for the *LunaTron* to climb. In this image, a small mound of gravel mixed into loose wet sand resulted in the *LunaTron* becoming immobilized.

DCS Dry compact sand

WFS Wet flat sand

WMS Wet mixed sand

CLA Crushed clay chips on top of packed sand

GRA Gravel on top of packed sand

PQU Pink quartz rock on top of packed sand

WQU White quartz rock on top of packed sand

and these types were binned into the following bulk composition sets:

AGG Aggregates consisted of CLA, GRA, PQU, and WQU

COM Compacted sand consisted of DCS and WFS

LOO Loose sand consisted of DLS and WMS

SAN Sand consisted of both COM and LOO

6.1.2 The LunaTron Rover

The *LunaTron* rover was initially assigned as a Capstone Design Project for the 2013-2014 Mechatronic Systems Engineering program at Western University. The initial requirements were to design a 10 kg lunar scout micro-rover with an instrumented chassis. *LunaTron* continued as a development project and was later became a required platform for this research.

LunaTron has an instrumented rocker-bogie chassis to collect proprioceptive measurement data. Load cells on each wheel provide the vertical loading on each wheel. Motor encoders provide the rotational position of the motor shaft, which is used to estimate the commanded rover speed. An optical mouse was used as an optic flow sensor to provide an estimate of the true rover speed. Wheel slip is then derived from the true speed and commanded speed. Current sensors measure the current draw of each motor, which provides an inferred measure of the torque delivered by the wheel. *LunaTron* has an Intel NUC computer running Linux Ubuntu 12.04 and ROS Hydro (described in Section 7.1.1). A websocket allows an external connection to ROS over port 9090. An Internet browser Javascript-based user interface allowed a user to control *LunaTron* over a WiFi connection to enable a wireless, mobile robot platform. For testing purposes, *LunaTron* was powered by an external power supply.

6.1.3 Integrated Vision System

The Integrated Vision System (IVS), shown in Figure 6.3, was developed by Optech Inc as part of CSA's ESM program to be an advanced vision system for planetary rovers, and was targeted for integration onto CSA's MESR rover [114]. IVS contains a lidar, spectrometer and visible camera for co-registration of spatial, RGB, and NIR data. The instrument parameters are provided in Table 6.1.

IVS was setup on a table next to the terrain box such that it would approximately be near the 3 m optimized range of the spectrometer. Space limitations within the Coudé room prevented



Figure 6.3: The Integrated Vision System (IVS) features a lidar head on a pan-tilt unit

Table 6.1: IVS instrument parameters.

Parameter	Value	Notes
Lidar	Perseus fibre laser	Class IV
Lidar wavelength	1541 <i>nm</i>	
Lidar avg Power	1.2 <i>W</i> at 450 <i>kHz</i>	
Lidar pulse	2.74 <i>ns</i> at 400 <i>kHz</i>	
Spectrometer	Ocean Optics NIRQuest	3 <i>m</i> optimized range
Spectral range	850 - 2500 <i>nm</i>	
Visible camera	Sony FCB-H11	

the table from being placed any further away from the box. However, a further distance from the would result in oblique lidar return.

IVS provided colour RGB images in .TIF file format. The lidar point cloud data included the lidar reflectance intensity values in the resultant .LAS files. The IVS user software enabled data fusion of the RGB values onto the point cloud. However, the fused data was saved as a .LAS file that could not be read by LAS viewers, nor was the data structure in a recognizable format. It was later decided that having coincident lidar and RGB images was ideal but not required. Lidar point clouds containing reflectance intensity and RGB images were collected for all terrain types.

The intention was to use IVS as a singular instrument for data collection to demonstrate its utility in terrain assessment. However, the spectrometer did not provide useful data. A Spectralon® reference tile was required for calibration purposes before each target sample was acquired. However, under both outdoor lighting and indoor quartz halogen lighting, IVS did not measure consistent reference spectra from the reference tile. The reflectance values changed based on the position of the quartz-halogen source, however overall the different configuration of integration times and light positioning did not result in consistent reference spectra. After several attempts to get meaning values from the spectrometer it was decided to not use IVS for measuring spectral response.

6.1.4 INO Hyperspectral Imager

A hyperspectral imaging platform from INO was used for collecting spectra of five different terrain types. Both visible and short wave infrared (SWIR) images were collected. The hyperspectral imaging took place separately from the terrain traversing testing at a different facility. Hyperspectral images of sand were taken, however only at one condition of moisture content. The terrain traversing testing included conditions of both wet and dry sand. The difference in water content would be evident in the spectra, therefore the hyperspectral images were only used for classification of the different aggregate types.

Table 6.2: INO Hyperspectral imaging platform parameters for both visible and SWIR ranges.

Parameter	Visible Range	SWIR Range
Detector	CCD (1392 x 1040- λ pixels)	HgCdTe (320 x 256- λ pixels)
Spectral Range	400 - 1000 <i>nm</i>	1000 - 2500 <i>nm</i>
Spectral Resolution	2.8 <i>nm</i>	6.8 <i>nm</i>
Spatial Resolution	down to 0.3 <i>mm</i>	down to 0.05 <i>mm</i>
Spatial Pixels	1392	320
Acquisition Rate	60 <i>Hz</i>	60 <i>Hz</i>
Sample dimensions	Up to 60 <i>cm</i> (W) along FOV, 40 <i>cm</i> (H)	Up to 60 <i>cm</i> (W) along FOV, 40 <i>cm</i> (H)

6.2 Terrain Data Collection

This section describes the data collection process for obtaining the IVS and *LunaTron* measured values of the terrain and terrain traversal. All data was collected over two days.

The terrain box was filled and configured to the desired terrain condition. A minimum of three IVS images and lidar point clouds were obtained for each terrain condition. *LunaTron* was then tele-operated to drive forward across the terrain box. The motors were driven with a pulse width modulation of 50%, which was the default set by the user interface. The load cells, current sensors and encoders were polled at 5 Hz and the data was sent to the tele-operator user interface where the data was saved as a .CSV file. During the testing phase, only the right side *LunaTron* sensors provided a complete data set and 1 load cell and 1 current sensor on the left side had failed. It was assumed that left side data would have been similar to the right side as *LunaTron* was only being driven forwards over homogeneous terrain, and therefore one side of data was deemed acceptable. A failed motor gear prevented *LunaTron* from being driven backwards, and thus it had to be physically reset after each traversal. Mid-way through the traversal testing the right side load cells also failed. However the load cell data prior to failure did not vary significantly between the terrain types that had been tested.

6.3 Data Processing and Feature Vector Construction

For this thesis, the objective was to process proximal data of terrain for classification against terrain labels. The proximal data sets include the images and lidar point clouds collected from IVS, and hyperspectral data cubes collected from the INO hyperspectral imager. *LunaTron* proprioceptive data sets include wheel speed and motor current draw. This section describes the steps to process the collected data and assembling feature vectors for training the classifiers.

6.3.1 Image Processing

Images of the terrain were captured from the IVS imager, as shown in Figure 6.4. For each terrain type, image strips of just the terrain were extracted from the IVS image, as shown in Figure 6.5. The image strip was then sub-divided into 50×50 pixel images patches, as shown in Figure 6.6 to be used for classification training. This process is repeated until there are 100 image patches for each of the terrain types. The size of the IVS image puts a limit on the number of image patches available for training.



Figure 6.4: Example of an RGB image acquired from IVS. In this scene the terrain box has a layer of crushed clay chips.

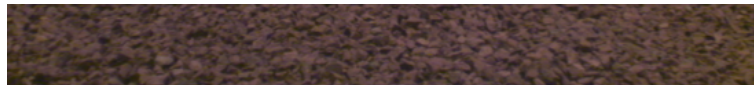


Figure 6.5: Example of a 550×60 pixel image strip used for creating training images for the terrain class.

A level 2 db2 wavelet transform is performed on each of the image patches. The transform results in a feature vector of 8436 coefficients, which includes the level 2 trend image and the 2-levels of fluctuations. The full image feature vector includes the trend, fluctuations, and the energy terms for the trend and fluctuations for a total of 8446 coefficients. The number of coefficients is greater than the number of available training sets, and requires greater computational



Figure 6.6: Example of a 50 x 50 pixel image patch used for classifier training.

effort to train a classifier. The 7 energy terms approximately capture the texture of the terrain, which is deemed to be appropriate for classifying the terrain types. The feature vector for the images are then the 7 energy terms from the wavelet transform: energy of the level 2 trend, 2 energy terms for each level of the diagonal, horizontal and vertical fluctuations. Image feature vectors containing the mean R, G, and B values for each image patch were also constructed for comparison purposes.

6.3.2 Lidar Reflectance Intensity

Lidar point returns were captured and converted to point clouds with IVS. Figure 6.12 shows an example of the reflectance intensity of the point cloud for a scene that contains the terrain box shown in Figure 6.11. The scene consists of three strips of aggregate resting on dry sand in the terrain box, and the surroundings of the Coudé room. In this example, the black walls

of the Coudé room poorly reflect the laser beam, and the dry wooden crate stacked beyond the terrain box reflects the laser beam well. Within the terrain box, the strips of aggregate reflect laser better in comparison to the sand on which they lay.



Figure 6.7: Three strips of aggregate laying upon flattened wet sand in the terrain box.

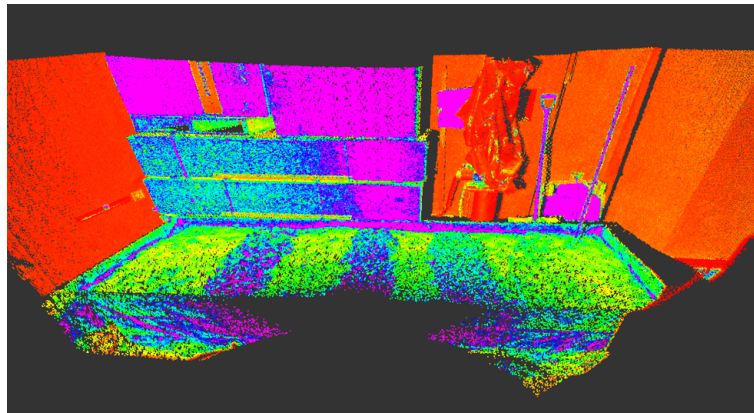


Figure 6.8: Example of a visualization of the reflectance intensity value for the point cloud. The point cloud corresponds to the greater scene shown in Figure 6.7. The colourization represents the reflectance intensity: red indicates a low (0%) intensity and violet indicates a high (100%) intensity.

The image and lidar reflectance can be compared to the that of flattened wet sand without the aggregate, shown in Figures 6.10 and 6.9. Here, the reflectance intensity of the flattened wet sand has low variability.



Figure 6.9: Flattened wet sand in the terrain box without the aggregate.

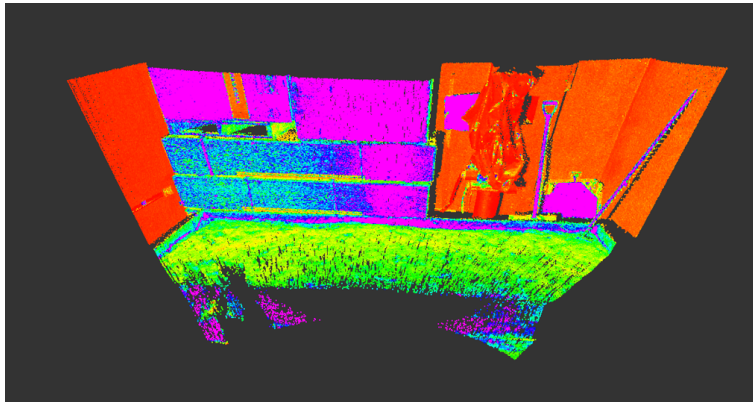


Figure 6.10: Example of a visualization of the reflectance intensity value for the point cloud. The point cloud corresponds to the scene in Figure 6.9. The colourization represents the reflectance intensity: red indicates a low (0%) intensity and violet indicates a high (100%) intensity.

The image and lidar reflectance can be compared to the that of unprepared wet sand, shown in Figures 6.12 and 6.11. Here, the reflectance intensity of the unprepared wet sand has a higher variability when compared to the flattened wet sand.

Point clouds containing reflectance intensity were obtained for each of the terrain types. The reflectance value of points within a 10 cm^3 cube were extracted from the lidar point cloud within the region corresponding to the terrain box. The reflectance values of 100 cubes centred



Figure 6.11: Unprepared wet sand in the terrain box.

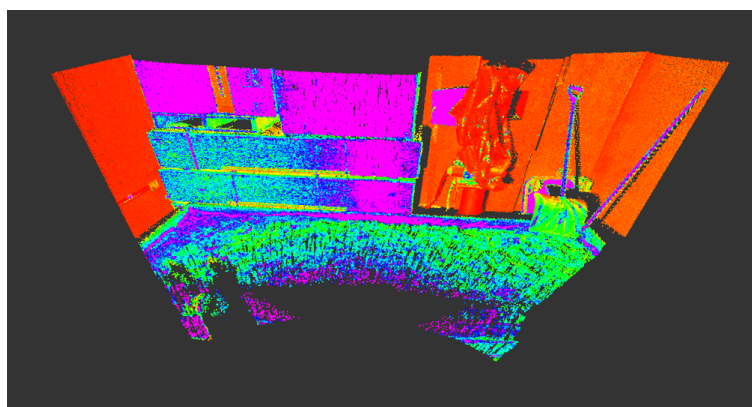


Figure 6.12: Example of a visualization of the reflectance intensity value for the point cloud. The point cloud corresponds to the scene in Figure 6.11. The colourization represents the reflectance intensity: red indicates a low (0%) intensity and violet indicates a high (100%) intensity.

approximately 5 *cm* apart from each other were obtained. The mean, and standard deviation, of the reflectance intensity within the cube were paired to form a feature vector to represent the average reflectance value and the variability within a region.

6.3.3 Spectral Reflectance Features

The hyperspectral imager produces a data-cube containing the spectral reflectance at 256 discrete wavelengths. A single point on an image contains the line spectra over those 256 wavelengths. Each hyperspectral image scene contains two terrain samples; 100 points within each terrain sample provide 100 spectral responses. The spectral responses were smoothed and processed to extract the number of peaks and the maximum peak value. These two parameters formed the spectral feature vector. The spectral feature vectors are only available for four of the aggregates: crushed clay chips, gravel, white quartz, and pink quartz.

6.3.4 Ensemble Feature Vectors

For each of the 8 terrain types there are 100 training samples of feature vectors of wavelet transformed images, and lidar reflectance intensities; for 4 of the terrain types there is also 100 training samples of feature vectors of the line spectra. For the 8 terrain types, sets of training feature vectors were created for comparison:

- Wavelet transformed images
- Image RGB values
- Lidar reflectance
- Transformed images concatenated with lidar reflectance
- RGB values concatenated with lidar reflectance

For the 4 aggregate types, the spectral features were also included for the following additional sets:

- Spectral features
- Transformed images concatenated with spectral features
- Lidar reflectance concatenated with spectral features

- Transformed images concatenated with lidar reflectance and spectral features

The sets of feature vectors were then used for training classifiers for performance comparison. All eight terrain types were used for comparison between the feature sets involving images and lidar; four aggregate types were used for comparison between feature sets involving images, lidar and line spectra. The bulk terrain compositions, aggregates, loose, and compacted sands were also compared for classification.

6.3.5 Data Comparison of Classifiers

The size of the classifiers is an important consideration in the context of planetary exploration rovers with limited storage memory and computational effort. Table 6.3 provides a comparison of the size of the trained classifiers, noting that the reduction in size by reducing the feature vector length. Table 6.4 provides a comparison of classification time, noting that training would likely be performed on higher performance computing than a planetary rover. However, in the case that a new classifier must be trained in situ, it is therefore worth noting the reduction in training time with the reduced feature vector length, and the reduced training time for Naive Bayes compared to SVM.

Table 6.3: Comparison of Matlab-trained classifier size for Naive Bayes and SVM classifiers using different feature vector lengths

Feature Vector Combination	NB Class. Size (KB)	SVM Class. Size (KB)
Images (reduced FV)	62	82
Lidar Intensity	13	32
Images (reduced FV) and Lidar Intensity	72	92
Images (full FV) and Lidar Intensity	45033	45700

It is also worth noting the time to run test data through the classifier. The test sets in Section 6.5 consisted of 40 feature vectors. The Naive Bayes classifier processed this test set in 0.5 s, whereas the SVM processed the set in 1.2 s.

Table 6.4: Comparison of Matlab-trained classification time for Naive Bayes and SVM classifiers using different feature vector lengths

Feature Vector Combination	NB Class. Time (s)	SVM Class. Time (s)
Images (reduced FV) and Lidar Intensity	1	260
Images (full FV) and Lidar Intensity	264	725

6.3.6 *LunaTron* Data Feature Vectors

A feature vector of *LunaTron* data for each terrain type were also constructed for classification purposes. Each feature vector consisted of mean and standard deviation of wheel speed for each wheel, and the mean and standard deviation of motor current draw for each wheel.

6.4 Results of Classification

This section describes the process of training and assessing the terrain classifiers. Appendix A contains the complete set of classification results and confusion matrices. Two classification methods, Naive Bayes and multi-class SVM, are compared. The following conditions were assessed and compared:

- 8 terrain types
- 4 aggregates including spectral features
- Bulk composition of aggregate, loose and compacted sand

and within each condition the performance of the classifiers were compared between the ensemble feature vectors.

6.4.1 Classifier Training with Matlab

All classification was performed using that Matlab Statistic and Machine Learning toolbox. The toolbox provides functions for training Naive Bayes and multi-class SVM classifiers, performing k-fold cross-validation of the trained classifiers, and producing confusion matrices.

Furthermore, the trained classifiers can be fed new test data for class prediction. The following results show the cross-validation classification errors for the set of classification conditions.

Classification of 8 Terrain Types

Table 6.5 shows the classification error following cross-validation of the two classifiers and three sets of feature vectors. The results show that transformed images alone are misclassified at a rate of 29% for Naive Bayes, and 36% for SVM, and lidar intensity alone is misclassified at a rate of 38% for both. The confusion matrices show that Naive Bayes poorly classifies PQU, WQU and WFS with just transformed images, whereas DCS is well-classified. These results are compared to the lidar reflectance, which poorly classifies DCS and DLS and correctly classifies WFS. The combination of the two feature vectors results in an error rate of 10%, with improvements to classification of the poorly classified types. Similar improvements to classification are shown with SVM.

Table 6.5: Comparison of classification errors feature vectors with Naive Bayes and SVM classifiers for all 8 terrain types.

Feature Vector Combination	NB Class. Error (%)	SVM Class. Error (%)
Images	29	36
Lidar Intensity	38	38
Images and Lidar Intensity	10	14

Classification Between 4 Sand Types

Table 6.6 shows the classification error following cross-validation of the two classifiers and three sets of feature vectors. The Naive Bayes classifier poorly classifies WFS with just transformed images, and poorly classifies DCS with just lidar intensity. The combination of features significantly improves classification, with only 1 misclassification in 400. The SVM classifier also poorly classifies WFS with just transformed images, and the addition of lidar intensity improves classification.

Table 6.6: Comparison of classification errors feature vectors with Naive Bayes and SVM classifiers for the 4 sand types.

Feature Vector Combination	NB Class. Error (%)	SVM Class. Error (%)
Images	15	24
Lidar Intensity	20	20
Images and Lidar Intensity	3	9

Classification Between 4 Aggregate Types

Table 6.7 shows the classification error following cross-validation of the two classifiers and three sets of feature vectors. Here, the addition of the spectral features improves the classification of the 4 types of aggregate material. Both the Naive Bayes and SVM classifiers poorly classify PQU with images alone, and classification improves for all classes with the addition of both lidar and spectral features.

Table 6.7: Comparison of classification errors feature vectors with Naive Bayes and SVM classifiers for the 4 aggregate types.

Feature Vector Combination	NB Class. Error (%)	SVM Class. Error (%)
Images	37	45
Lidar Intensity	23	24
Spectral Features	23	47
Images and Lidar Intensity	14	15
Images and Spectral Features	13	42
Lidar Intensity, and Spectral Features	9	18
Images, Lidar Intensity, and Spectral Features	6	13

Classification Between 3 Bulk Compositions

Tables 6.8 and 6.9 show the classification error following cross-validation of the two classifiers and three sets of feature vectors. For comparison, the transformed image energy terms provide an improved classification compared to using colour terms. The multi-class SVM performs better than the Naive Bayes when classifying the 3 bulk compositions, whereas the Naive Bayes classifier performed better when classifying the individual types. The Naive Bayes

poorly classifies loose sand regardless of feature vector, however there is an improvement with the combination of transformed images and lidar intensity. The SVM similarly poorly classifies loose sand with either transformed images or lidar intensity, however the combination of the two features significantly improves the classification.

Table 6.8: Comparison of classification errors feature vectors with Naive Bayes and SVM classifiers for the 3 bulk compositions with transformed images.

Feature Vector Combination	NB Class. Error (%)	SVM Class. Error (%)
Images	15	15
Lidar Intensity	43	42
Images and Lidar Intensity	15	7

Table 6.9: Comparison of classification errors feature vectors with Naive Bayes and SVM classifiers for the 3 bulk compositions with image colour terms.

Feature Vector Combination	NB Class. Error (%)	SVM Class. Error (%)
Images	48	35
Lidar Intensity	43	42
Images and Lidar Intensity	22	19

6.4.2 *LunaTron* Traversal Testing

Tables 6.10 and 6.11 provide a summary of the *LunaTron* traversal data for each of the 8 terrain types and the binned 3 bulk composition types. The summary shows the current draw and wheel speed to be similar within all types. From the perspective of vehicle performance and prediction, there is a greater distinction in current draw and wheel speed when comparing the bulk compositions. Loose sand, whether it is wet or not, will require greater current draw and has a lower speed compared to aggregate materials. Similarly, compacted sand, whether it is wet or not, results in the lowest current draw.

Table 6.12 shows the classification error following cross-validation of the two classifiers for the *LunaTron* data sets. The SVM miss-classifies all of the compacted sand sets as aggregates,

Table 6.10: Mean current draw per wheel over terrain types.

Terrain Type	Right Front Wheel		Right Middle Wheel		Right Rear Wheel	
	Mean (A)	Std (A)	Mean (A)	Std (A)	Mean (A)	Std (A)
CLA	0.571	0.131	0.666	0.182	0.479	0.102
DCS	0.565	0.066	0.642	0.102	0.475	0.067
DLS	0.606	0.081	0.713	0.113	0.546	0.080
GRA	0.598	0.158	0.693	0.182	0.456	0.101
PQU	0.609	0.141	0.629	0.163	0.467	0.079
WFS	0.573	0.093	0.672	0.099	0.476	0.067
WMS	0.692	0.097	0.815	0.134	0.622	0.078
WQU	0.604	0.205	0.708	0.170	0.490	0.096
AGG	0.597	0.051	0.671	0.067	0.472	0.043
COM	0.565	0.021	0.661	0.030	0.473	0.027
LOO	0.648	0.057	0.762	0.062	0.587	0.047

whereas the Naive Bayes correctly classifies most of the compacted and loose sand sets, and miss-classifies some aggregate as compacted sand.

6.5 Prediction Step

This section presents the results of providing the classifiers with previously untrained data to assess their performance. There are three cases that are examined in which the terrain transitions from one type to another. The classifiers predict a terrain class, and that class has an associated vehicle performance as given in Section 6.4.2 which is compared to the measured vehicle performance. For this stage, the bulk composition of terrain is considered.

6.5.1 Aggregate to Loose Sand

The first prediction is for a transition from GRA to WMS, as shown in Figure 6.13, with an image strip shown in Figure 6.14. For terrain and vehicle purposes this is considered to be AGG to LOO. As *LunaTron* is accelerating for most of the first section, the prediction step is

Table 6.11: Mean wheel speed wheel over terrain types.

Terrain Type	Right Front Wheel		Right Middle Wheel		Right Rear Wheel	
	Mean (m/s)	Std (m/s)	Mean (m/s)	Std (m/s)	Mean (m/s)	Std (m/s)
CLA	0.267	0.041	0.270	0.048	0.272	0.049
DCS	0.270	0.047	0.276	0.051	0.273	0.051
DLS	0.225	0.063	0.235	0.064	0.233	0.065
GRA	0.264	0.063	0.267	0.061	0.262	0.060
PQU	0.275	0.039	0.281	0.047	0.274	0.050
WFS	0.269	0.052	0.275	0.052	0.269	0.054
WMS	0.219	0.038	0.226	0.040	0.223	0.038
WQU	0.254	0.060	0.260	0.057	0.259	0.057
AGG	0.267	0.017	0.270	0.019	0.266	0.018
COM	0.268	0.015	0.278	0.017	0.272	0.014
LOO	0.222	0.014	0.233	0.017	0.230	0.014

Table 6.12: Comparison of classification errors for *LunaTron* data with Naive Bayes and SVM classifiers for the 8 terrain types and 3 bulk compositions.

Feature Vector Combination	NB Class. Error (%)	SVM Class. Error (%)
Wheel Speed and Current, 8 Terrain Types	21	39
Wheel Speed and Current, 3 Bulk Compositions	14	36

only taken on the second terrain type.

A set transformed image features and lidar intensity are created to be supplied to the Naive Bayes and SVM classifiers. Both classifiers correctly identify the first section as aggregate and the second section as loose sand. The difference between classifiers occurred at the transition between sections, where images contained portions of both types. For the second section of loose sand, the predicted *LunaTron* wheel speed and current draw is compared to the measured values as given in Table 6.13. In this case the measured values were greater than 1 standard deviation from the predicted value. This is attributed to the likelihood that the sand was not as loosely mixed as it was during the homogeneous terrain testing.



Figure 6.13: In this scene the terrain box has a section of gravel and a section of wet mixed sand, with the *LunaTron* traversing from left to right.

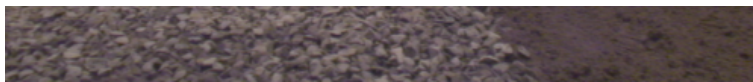


Figure 6.14: Image strip featuring a transition from gravel to wet mixed sand.

6.5.2 Covered Aggregate to Flat Wet Sand

The second prediction is for a transition from gravel dusted with loose sand to the flat wet sand, as shown in Figure 6.15. This set is to assess how the classifiers predict a set of features from a hybrid terrain type not previously seen. For terrain and vehicle purposes this is considered to be transitioning to COM.

The Naive Bayes misclassified most of the second section as LOO when using both transformed image and lidar features, whereas the SVM is correct in classifying most of the second section as COM. Both the Naive Bayes and SVM classify the first section of hybrid terrain as loose terrain using the combine feature vector. Using only the lidar intensity, both the Naive Bayes and SVM correctly classify the second section as COM. Both the Naive Bayes and SVM classify the first section of hybrid terrain as AGG using only the lidar features.

For the second section of compact sand, the predicted *LunaTron* wheel speed and current draw is compared to the measured values as given in Table 6.14. In this case the measured

Table 6.13: Mean wheel speed wheel and current draw over LOO predicted terrain.

	Right Front Wheel		Right Middle Wheel		Right Rear Wheel	
	Mean (m/s)	Std (m/s)	Mean (m/s)	Std (m/s)	Mean (m/s)	Std (m/s)
Predicted	0.222	0.014	0.233	0.017	0.230	0.014
Measured	0.291		0.302		0.301	
	Mean (A)	Std (A)	Mean (A)	Std (A)	Mean (A)	Std (A)
Predicted	0.648	0.057	0.762	0.062	0.587	0.047
Measured	0.615		0.656		0.521	



Figure 6.15: In this scene the terrain box has a section of covered gravel and a section of wet flat sand, with the *Lunatron* traversing from left to right.

current values were within 1 standard deviation from the predicted value, whereas for the wheel speed the measured values were greater than 1 standard deviation from the predicted value.

6.5.3 Gravel to Covered Aggregate

The final prediction is for a transition from gravel to gravel dusted with loose sand, as shown in Figure 6.16. This set is to assess how the classifiers predict a set of features from a hybrid terrain not previously seen.

Both Naive Bayes and SVM correctly identify the first section as AGG when using both transformed image and lidar features. Both Naive Bayes and SVM classify the second section

Table 6.14: Mean wheel speed wheel and current draw over COM predicted terrain.

	Right Front Wheel		Right Middle Wheel		Right Rear Wheel	
	Mean (m/s)	Std (m/s)	Mean (m/s)	Std (m/s)	Mean (m/s)	Std (m/s)
Predicted	0.268	0.015	0.278	0.017	0.272	0.014
Measured	0.301		0.309		0.307	
	Mean (A)	Std (A)	Mean (A)	Std (A)	Mean (A)	Std (A)
Predicted	0.565	0.021	0.661	0.030	0.473	0.027
Measured	0.586		0.653		0.475	



Figure 6.16: In this scene the terrain box has a section of covered gravel and a section of gravel, with the *Lunatron* traversing from right to left.

of hybrid terrain as LOO using both transformed image and lidar features. However, both classify the hybrid terrain as AGG when using only lidar features.

For the second section of covered aggregate, the predicted *LunaTron* wheel speed and current draw is compared to the measured values as given in Table 6.15. In this case the measured current values were within 1 standard deviation of both the LOO and AGG terrain types. The measured wheel speeds are greater than 1 standard deviation from both, however they are closer to the AGG values. The measured current draw is likely greater than for clean aggregate due the wheels slipping on the dusted sand, and is likely less than for loose sand as the underlying gravel provides improved traction.

Table 6.15: Mean wheel speed wheel and current draw over COM predicted terrain.

	Right Front Wheel		Right Middle Wheel		Right Rear Wheel	
	Mean (<i>m/s</i>)	Std (<i>m/s</i>)	Mean (<i>m/s</i>)	Std (<i>m/s</i>)	Mean (<i>m/s</i>)	Std (<i>m/s</i>)
LOO	0.222	0.014	0.233	0.017	0.230	0.014
AGG	0.267	0.017	0.270	0.019	0.266	0.018
Measured	0.291		0.297		0.294	
	Mean (<i>A</i>)	Std (<i>A</i>)	Mean (<i>A</i>)	Std (<i>A</i>)	Mean (<i>A</i>)	Std (<i>A</i>)
LOO	0.648	0.057	0.762	0.062	0.587	0.047
AGG	0.597	0.051	0.671	0.067	0.472	0.043
Measured	0.635		0.728		0.536	

6.6 Discussion, Limitations, and Recommendations

Terrain classification was compared using two classifiers: Naive Bayes and multi-class support vector machines. Many other classification techniques, such as artificial neural networks, exist and could have been examined. However the intent of this research was not to find the optimal classification method; the intent was to demonstrate that lidar reflectance intensity and spectral features improve classification over images alone. For this thesis, both Naive Bayes and SVM classifiers demonstrated reduced classification errors when provided feature vectors including lidar and spectral features.

Classification was compared between Naive Bayes and SVM classifiers. Both classifiers had similar performances, with Naive Bayes generally showing improved classification. In the context of a low-cost lunar prospecting rover with limited computational capacity, the Naive Bayes was shown to require less time to classify test data compared to SVM. Additionally, the reduced feature vector greatly reduced the size the resultant classifiers compared to using the full feature vector length.

The experimental work was conducted on 8 different terrain types that are not an exhaustive list of soils or terrain conditions. Soil with organic content, such as topsoil, or clay-rich soil are found in off-road unstructured environments in which mobile robots may be deployed, such as agricultural lands and forests. To deploy a mobile robot with a trained classifier would require

training data from many more terrain types. Alternatively, unsupervised classifiers could be utilized to classify terrain as the mobile robot is deployed in the field. However, it may not be possible to classify a hazardous terrain until the mobile robot has encountered it.

The experimental work did not involve a full set of hazardous terrain conditions that resulted in immobilization, such as loose terrain on an incline. A full set of immobilization conditions would be required to train the classifier to for such prediction. The terrain box was lifted on jacks twice, and the *LunaTron* was driven up the incline in both dry loose sand and wet mixed sand. It was able to traverse the incline in loose dry sand, with a measurable increase in current draw. It became immobilized in the wet mixed sand on the incline. The jacks failed after the second set and were not able to be raised again.

Proximal soil sensing combined with soil inference systems has been shown to predict soil mechanical properties using single spectral measurements. These techniques similarly require a prior set of measured soil data, and the soil inferencing is limited to soil specific to a region. In other words, training with Southern Ontario soil may not work for inferring soil in New Zealand.

It should be noted that spectroscopy alone is not better than standard RGB images in the sense that the interpreted spectra only applies to the top few microns of the surface. *Spirit* was trapped by loose drift material that visually looked similar to the more solid material it had been driving on. Howard et al [115] note that “sensing only terrain geometry fails to reveal mechanical properties of terrain that are critical to assessing its traversability, such as potential for slippage, sinkage, and the degree of compliance with potential obstacles”. The reflectance intensity can be interpreted to indicate the dryness of the soil. A dry sand can be interpreted to be more likely to be weakly cohesive, whereas a dry clayey soil may have improved shearing. Lidar reflectance intensity has been used to interpret duricrusts with underlying weakly cohesive soils. However, the same reflectance intensity may also indicate solid rock. A high-powered laser could heat the terrain and the thermal inertia could be measured to infer soil density. However, the IVS laser was not sufficiently powerful to heat the sand, nor did the user interface for IVS allow for the laser to be operated in such a setting. Furthermore, the thermal

inertia would require IR sensors to measure.

The lidar and spectroscopic data collected were not vehicle-centric. IVS was designed to be mounted on a vehicle similar in scope to MESR, whereas *LunaTron* was used for collecting vehicle data. The mass of IVS is beyond what *LunaTron* could carry, and IVS required a dedicated power supply. Furthermore, the mass and power requirements of IVS are beyond what the Husky rover could meet. More importantly IVS is not suited to field operations on a mobile platform at its currently technology readiness level. Therefore, a complete integrated mobility test involving an instrumented mounted on a vehicle was not performed. It is worth noting that even though IVS was designed to integrate with a rover such as MESR, the user interface for MESR did not facilitate access to lidar intensity data, which would have been required for this work had IVS been mounted to it. Similarly, the hyperspectral images of the samples were collected at a different facility. The hyperspectral imager was fixed to a platform and the samples placed underneath for imaging. This set up was also not conducive to integrated testing with a rover.

One goal for classifying terrain is to predict mobile robot performance before coming in contact with terrain to avoid immobilization scenarios. Instead of trying to avoid immobilization, the vehicle could be sized with more powerful motors to overcome such terrain. However, off-road vehicles with powerful engines to drive wheels are not able to overcome any obstacle or terrain condition and occasionally become stuck. For battery powered mobile robots, more powerful motors require greater power which leads to increased mass or reduced operational life. None-wheeled options, such as tank treads, provide improved traction but require more power to operate.

Chapter 7

Tele-Operation Over Time Delay

This chapter presents the experimental outcomes of the tele-operation testing. The objective of this testing is to assess human performance in remotely operating a mobile robot in poor lighting conditions over time delay. The intention is to demonstrate that human-in-the-loop direct-drive tele-operation remains, in the near term, a more viable option to autonomy for a low-cost short-duration south lunar pole prospecting mission.

Human performance experimentation inherently requires a set of human testers. A tangential development project, REALM, sought to enable web-browser based access to robotic equipment which would facilitate remote participation. A collaboration with the Italian Mars Society had the potential to provide approximately 30 volunteers to remotely drive a mobile robot through an circuit at Western University in daylight and in the dark with time delay and harsh lighting. The primary objective for the Italian Mars Society's study was to evaluate the human operator experience, and to serve as a basis for developing future studies. While some initial results were achieved [116], a number of complicating factors prevented this collaboration from being fulfilled. The outdoor driving circuit at Western University needed to be close enough to an Internet access point to facilitate the wireless connection to the mobile robot. The wireless connection also needed to be strong enough over the extent of the circuit to facilitate streaming video to the remote user. These access restrictions limited the circuit to be the garden pathway outside of the Spencer Engineering Building. However, this area is traf-

ficked throughout weekdays, which limited testing time to the weekend. Additionally, the dark condition could be performed overnight with the remote participants 6 hours ahead in Europe, instead of requiring local participants to devote a night. However, the Internet connection between Europe and the local server proved to be too unstable to facilitate this remote access and driving tests. The experience from this attempt demonstrated the need to have a strong stable wireless connection between the human tester and the mobile robot, and the need to conduct the testing at an off-campus location.

The remainder of this chapter describes the experimental setup for two sets of tele-operation testing, the results of the testing, and an interpretation of the results.

7.1 Experimental Equipment

This section describes the equipment and setup for the tele-operation experiments. Data collection took place at the Elginfield Observatory, shown in Figure 7.1. The observatory, which is no longer used for astronomical research, is located north of London, Ontario. The initial testing took place outdoors with a course set up on the grounds in front of the building. Following the initial remote driving tests, cornering tests were conducted inside the building in the telescope dome where lighting could be controlled. For both sets of testing the human tele-operators was located in a windowless room within the observatory such that they could not see either the outdoor course or the indoor cornering setup.

7.1.1 The Robot Operating System

The Robot Operating System (ROS) is a middleware framework that facilitates data messaging between sensing devices, actuators, algorithms, and users. ROS provides the communication layer between nodes. Nodes are the sources and sinks for data within a ROS network, and they communicate to each other via the ROS Master node. Messages contain data that are published or read by nodes on specific topics. Topics are asynchronous many-to-many communication streams. A node can publish messages to a topic regardless of whether or not another node



Figure 7.1: Both the outdoor and indoor tele-operation testing took place at the Elginfield Observatory.

is reading those messages. A node that is subscribed to a topic will try to read any message that gets published to that topic regardless of whether or not another node is publishing to that topic. In addition to messages are services and actions. Services are synchronous one-to-many functions for short requests. Actions are similar to services but are longer running processes.

Additional ROS packages are required for interfacing with hardware. The `rosbridge suite` package facilitates external connections to a local ROS network. A WebSocket connection becomes a node on the ROS network and enables messaging into and out of the network. The `rosbridge server` converts JSON-formatted data strings sent by an external user interface to ROS topic messages; these topic messages are read by other nodes. Conversely, topic messages sent to the WebSocket are converted to JSON strings to be read by the remote UI. The `usb camera` package reads in the video captured from a USB web camera, and the `web video server` package

provides streaming video to an external user.

The tele-operation testing used ROS Hydro operating on Linux Ubuntu 12.04 machines.

Table 7.1: List of commonly used ROS Hydro packages.

ROS Package	Function
husky	Husky kinematics
rosbridge_suite	Facilitates external connections
usb_cam	Capture video from web cam
web_video_server	Streams video to external viewer

7.1.2 Husky A200 Mobile Robot

The Clearpath Robotics Husky A200 mobile robot platform was used as the rover for tele-operation. The Husky platform is 99 *cm* long, 67 *cm* wide (wheel to wheel), and 39 *cm* tall. Its nominal mass is 50 *kg* without additional hardware, and is capable of handling a maximum payload of 75 *kg*. It has a maximum speed of 100 *cm/s*, and can turn-in-place.

The Husky was controlled with a laptop computer running Linux Ubuntu 12.04. Connected to the laptop was an external WiFi adapter, and a monocular camera. The peripherals and Husky serial interface were all connected via USB hub to the laptop. The external 9 dBi Wireless N adapter provided improved connectivity at greater distance compared to the internal laptop adapter. Two forward-facing LED headlights were powered off of the internal Husky battery to provide lighting in dark conditions.

ROS Hydro facilitated data messaging between sensing devices, the Husky, and the remote user. The Logitech QuickCam Pro 9000 monocular camera was mounted near the rear of the Husky to allow the front two wheels to be visible in the field of view. ROS captured video from the camera nominally at 15 FPS and provided the video for streaming using the Web Video Server package.

The remote user connected to the Husky via a WiFi connection. A rosbridge server on the Husky laptop provided a WebSocket connection to allow for the remote user to connect to the Husky. The rosbridge server converted JSON-formatted data strings sent by the user



Figure 7.2: The Husky A200 mobile robot shown outdoors for the tele-operation testing.

interface to ROS topic messages; these topic messages were then read by the Husky packages and converted to motion commands. The outbound video was provided by the Web Video Server. This video server allowed the video quality, in terms of video compression, to be controlled by the remote user.

7.1.3 Tele-Operation User Interface

The remote user controlled the Husky from an Internet browser Javascript-based user interface (UI). The UI read in inputs from a Logitech F310 gamepad and sent the corresponding JSON formatted data strings to the IP address of the Huskys laptop. The UI provided the video stream, input to adjust the video quality and time delay, and a gamepad input indicator.

A Javascript-based internet browser provided the interface to the Husky. The laptop on board the Husky ran the Robot Operating System (ROS), and provided a WebSocket connection using the `rosbridge` server package. The game pad inputs were sent to the WebSocket connection and were then converted to translational and rotational motion by the Husky ROS



Figure 7.3: The user tele-operates the rover through an interface using a gamepad.

packages. Streaming video was nominally captured through ROS at 15 FPS and delivered using the web video server package; the frame rate was adjusted on the Husky webcam end while the video quality and resolution were adjustable on the Javascript interface end. The time delay was enabled by buffering video frames for the designated duration.

7.2 Outdoor Driving Course

This section describes the results of the initial tele-operating tests through outdoor driving courses. The testing focused on the human performance of tele-operating a rover in lighting conditions that may be experienced at the South Lunar pole over limited band-width and time-delay. Two sets of three time trials were performed; each set involved five test drivers. Each set of time trials was performed on different test circuits. The time trials were of increasing operational difficulty: daylight conditions without time delay, daylight conditions with time 4 s delay, and harsh lighting with 4 s time delay. The harsh lighting was after nautical dusk with a 1000 W spotlight shining over the circuit. Obstacles were placed in the path of the light to cast



Figure 7.4: The tele-operated rover provides streaming video for the user.

long shadows.

The first circuit was a simple double figure-8, shown in Figure 7.5 toward the spotlight. From the operator's perspective the Husky was driving into the low-angle light around obstacles, and the driving away from the light into long shadows. The circuit was approximately 90 *m* in displacement and two circuits were completed for a total displacement of 180 *m*. A more complicated circuit, shown in Figure 7.6 with a total displacement of 150 *m*, with more turns and greater distances between waypoints, was completed by a different set of drivers. This complex circuit featured similar situations of driving into the low light and into shadows.

7.2.1 Results

The results of the simpler circuit, given in Table 7.2, show that the drivers had consistent times for the ideal daylight conditions. The addition of the time delay caused an expected increase in completion time. However, by the final run in harsh lighting conditions, the drivers had learnt the circuit and 4 out of 5 improved their performance. The average speed over circuit in ideal



Figure 7.5: The first test circuit was a double figure 8; when repeated once the total drive distance is approximately 180 *m*.

conditions was 41 *cm/s* and 31 *cm/s* for harsh lighting conditions compared to a set speed of 50 *cm/s* for the Husky. The results of the more complex circuit are shown in Table 7.3.



Figure 7.6: The more complicated driving circuit had the driver tele-operate the rover through a number of turns and straight-aways for a distance of approximately 150 *m*.

The average speed for the ideal conditions was 41 *cm/s* which is consistent with the previous trial. When the time delay was introduced, the average speed reduced to 29 *cm/s*, and further reduced to 21 *cm/s* in harsh lighting. In both cases, the standard deviation on completion time increased with the difficulty of the task.

The times listed in Tables 7.2 and 7.3 are the times from when the vehicle first began to move until the time the rover returned to the starting area. The three trials are denoted as T1 for ideal conditions, T2 for daylight and time-delay, and T3 for harsh lighting. Minor penalties, denoted by lower-case ‘m’, are noted for instances where the rover ran into or grazed an obstacle, but did not require human intervention. Major penalties, denoted by capital ‘M’, required human intervention to rescue or prevent damage to the rover. A major penalty on an

actual mission would likely result in failure.

Table 7.2: Times for 180 *m* figure 8 circuit: Set 1.

	T1 (<i>s</i>)	Pen.	T2 (<i>s</i>)	Pen.	T3 (<i>s</i>)	Pen.
Driver 1	434		699		855	1m
Driver 2	435		636		490	
Driver 3	434		705		496	
Driver 4	424		577		480	2m
Driver 5	444		1001	1M	777	1m
Mean	434		724		620	
Std. Dev	6.3		146		162	

The general experience for tele-operators for the first circuit was that the addition of time-delay increased the difficulty of the circuit. On straight-aways there was a momentary lapse in recalling the time-delay; the user would be pressing the directional joystick on the gamepad and observing the forward motion on the video feed which, after 4 seconds, would appear to be occurring without delay. The greatest challenge under time delay was cornering around obstacles; it would only be when attempting to drive around or avoid an obstacle that the user would recall the delay. This lapse is noted in the major penalty of Driver 5. For the harsh-lighting condition the users had essentially learnt the simple route and were able to navigate it despite the reduction in visibility. This ‘blind driving’, while on average resulted in faster times, did have a greater number of minor penalties from the rover grazing into obstacles from tight turns.

The second trial, with new drivers, introduced a circuit that was not as easy to navigate from memory. For the two trials under ideal conditions the average driving speed was the same, however for the more complex circuit that standard deviation on time to completion was greater. The introduction of time-delay resulted in similar experiences as the first group: momentarily forgetting about the time-delay while on straight-aways and difficulty turning. The driver was not able to learn and memorize the circuit as easily as the first circuit; with the introduction of the harsh lighting conditions the time to completion increased further. As expected, turning was an even greater challenge in this lighting condition. In shadow, and despite the headlights

Table 7.3: Times for 150 m complex circuit: Set 2.

	T1 (s)	Pen.	T2 (s)	Pen.	T3 (s)	Pen.
Driver 6	415		483		588	1M1m
Driver 7	370	1m	528		975	
Driver 8	364	1m	542		706	
Driver 9	336		592		788	
Driver 10	336		435	1m	675	
Mean	364		516		746	
Std. Dev	29		53		131	

on the rover, it was difficult to assess the amount the rover had turned. Driving into the low-angle light was itself not a challenge, however it made identifying potential hazards on the ground more difficult.

Comparison of the two circuits showed consistent operator speed regardless of circuit configuration in ideal conditions. The difference in maximum permissible speed and operated speed is attributed to reduced speed while turning corners. Table 7.4 provides a summary of the the average speeds and Table 7.5 provides a summary of the errors. The average speed under time delay was similar to *Copernicus* testing (35.5 cm/s), while noting that *Copernicus* testing was for a far greater distance.

Table 7.4: Summary of averaged speeds (cm/s) for all 6 trials.

	T1	T2	T3
Set 1	41	25	31
Ratio	82 %	50 %	62 %
Set 2	41	29	21
Ratio	82%	58%	42 %

Table 7.5: Summary of errors for all 6 trials.

	T1	T2	T3
Set 1	0	1M	4m
Set 2	2m	1m	1M1m

7.2.2 Interpretations of Results

The results showed that a human operator could tele-operate a mobile robot in harsh lighting conditions under time-delay. The average drive speed was 21-31 *cm/s* under these conditions, compared to 41 *cm/s* under ideal conditions for a mobile robot with a set speed of 50 *cm/s*. This speed compares favourably to autonomous mobile robots using lidar-based navigation (3-6 *cm/s*), and to current planetary robots utilizing space qualified flight computers (1.5 *cm/s*). The results from this initial testing informed the need for a more focused study on the human performance specific to the steering the mobile robot around corners.

This performance in the south lunar polar analogous lighting conditions suggests that a near-future lunar prospecting mission be conducted in a direct-drive tele-operated manner to minimize complexity and cost to ensure the mission proceeds. By minimizing the use of autonomy and active sensing, then overall power and computational requirements are lowered which leads to a reduction in program cost. Over the duration of a longer mission, off-loading navigation to autonomy makes far more sense, however the short duration nature of a proposed prospecting mission may benefit from have direct human operators. It is proposed that demonstrating the prospecting technology over the short-duration mission is the near-term objective; robust autonomy is better suited for a mission of greater duration, scope and budget.

7.3 Cornering Law Testing

The cornering law testing was set up inside the Elginfield Observatory telescope dome. The human tester tele-operated the Husky through a cornering task. The task consisted of driving the Husky forward through one corridor and out the aperture and turn left into an orthogonal aperture with a corridor of equal width, as shown in Figures 7.7 and 7.8. The conditions of the task randomly varied. The corridor widths varied between 85, 95, 105, 115 *cm*; the lighting varied between ambient dome lighting, dome lighting off with a 250 *W* light directed toward the initial Husky placement and forward facing LED headlights on, and dome lighting off and forward facing LED headlights on; and the time-delay on the returned video varied between

0, 2, and 4 seconds. These combinations totalled a block of 36 different task conditions. Each block was repeated for a total of 4 blocks.



Figure 7.7: The corridor walls were higher than the field of view of the monocular camera. The tele-operator had to navigate around the corner using the limited spatial cues visible in the field of view, including placement of the walls. Shown with an aperture width of 95 *cm*

The human tester was provided an opportunity to practise operating the Husky outside of the dome within visual proximity to assess how it moved, turned, and visually appeared in the UI over the various time delays. The Husky was then moved back into the dome for the time trials to begin. The timer began when the Husky began to move until it crossed a finish line. Crossing the finish line resulted in a successful task attempt. The task attempt was halted and counted as an error if the Husky collided with a wall. The task condition was reset in the event of an error and the human tester was provided the opportunity to try repeat. Each task condition was afforded three attempts before being recorded as ‘did not finish (DNF)’. After a completed attempt, or DNF, the next random task condition was set up.



Figure 7.8: Cornering through corridors, shown with an aperture width of 95 *cm*.

The parameters of the task conditions were first examined with an initial human tester. Aperture widths of 125 and 135 *cm* were initially considered, however it was found that there was little difference in performance between these and the 115 *cm* width. These two widths were scrapped in favour of reducing the total number of tasks in a given block. The narrower width of 85 *cm* was instead added to increase the task difficulty. A spot light was planned to be placed facing out from the second corridor. However, the light cast by this setting differed little from the ambient light condition, and the direct brightness of the light was not present in the video until after the corner had been turned. This second spot light configuration was eliminated in favour of having all lights aside from the LED headlights off. This lighting condition was established as the most difficult.

Eight human testers volunteered to each spend time at the observatory performing the tele-operating tasks. Each block took between 1 and 4 hours to complete, with the first block typically requiring the longest amount of time and the fourth requiring the least. For most testers,

the first block was performed on one day and the remaining three blocks were performed on a second day¹. The first day included the introduction and initial practise, and during the first block short breaks were taken after subsets of 12 tasks were completed. Additional time was required to ensure the human tester was following along and on the correct task condition. The introduction of the task to the human tester was conducted in the windowless operations room next to the telescope dome. The dome remained closed off during the introduction. The cornering task, including the variable parameters, was described to the human tester. The Husky was brought outside of the dome to allow the tester to visualize the vehicle and practise operating it with the UI. The Husky was then taken back to the dome to begin the first block. For blocks 2, 3, and 4 the full block of 36 tasks conditions were performed before taking a half-hour break. Generally the success rate and times improved with each successive block.

7.3.1 Results

This section presents the results from the cornering tests. Times and errors were recorded for each of the 36 task conditions over 4 trial blocks for 8 human testers. The data for one of the human testers was discarded as the task completion times were in upwards of 10 times greater than mean for the remaining 7 and adversely skewed the results. The results presented here are for the remaining 7 human testers.

Out of all recorded tasks, the longest task completion time was 305.5 seconds, and the shortest task completion time was 17.4 seconds. For tasks that resulted in DNFs, an adjusted completion time t_{adj} was assessed based on the successful times for that specific task condition:

$$t_{adj} = t_{min,c} + e_c \times t_{max,c} \quad (7.1)$$

where $t_{min,c}$ is the minimum successful completion time for that task condition, f_c is the failure rate for task condition and $t_{max,c}$ is the maximum successful completion time for that task condition. Then, for each of the 36 task conditions, an averaged time was calculated over

¹Tester number 7 required a third day to complete the fourth block; tester number 8 completed all four blocks in one day due to time restrictions

all trial blocks and human testers. The sum of all errors and attempts was also calculated to assess a failure rate. A score for each task condition was also assessed to account for both the time and error rate:

$$S_c = \frac{1}{2} \left(\frac{t_{mean,c}}{t_{max,c}} + \frac{e_c}{a_c} \right) \quad (7.2)$$

where $t_{mean,c}$ is the average completion time for a task condition, t_{max} is the global maximum task completion time of 305.5 seconds, e_c is the total number of errors for a given task condition, a_c is the total number of attempts for a given task condition, and S_c is the resultant score out of 1. Scores approaching 1 indicate that the task was more difficult to complete. It is noted that a score of 1, which would indicate the task was impossible, is not achievable using this formulation as half of the score is given based on at least one successful time. A low score indicates that the task was completed quickly with little error. A summary of these results are provided in Appendix B. The score facilitates comparison between the lighting conditions. Based on these scores, the most difficult task condition was tele-operating the mobile robot at the narrowest corridor over 4 seconds of time delay in the dark. The easiest task condition was tele-operating the mobile robot at the widest corridor without time delay in the dark. Times, errors, and scores are also provided in Appendix B for the trial blocks. The general trend shows a reduction in errors and completion times with successive trial blocks.

7.3.2 Cornering Law

Indexes of difficulty are derived using models outlined in Chapter 5 to fit the completion time results into a cornering law formulation. Each index of difficulty, shown in Table 7.6 was assessed in the linear regression for goodness of fit. The model proposed by Pastel [111] and used by Helton [112], where $ID = \log_2 \left(\frac{p}{w-p} + 1 \right)$, resulted in the best fit as determined by greatest R^2 values and positive intercept values. This model is also analogous to the Shannon formulation of Fitts' Law based on information theory.

Table 7.6: Indexes of Difficulty for corridor widths.

Widths (m)	$ID = \frac{p}{w-p}$	$ID = \log_2\left(\frac{p}{w-p} + 0.5\right)$	$ID = \log_2\left(\frac{p}{w-p} + 1\right)$
0.85	3.72	2.08	2.24
0.95	2.39	1.53	1.76
1.05	1.76	1.18	1.47
1.15	1.40	0.92	1.26

Interpretation and Comparison of Lighting Conditions

The results are first examined to compare the three lighting conditions. Table 7.7 shows the results of linear regression for the no time delay condition, and the mean times are plotted against ID in Figure 7.9. The ambient lighting condition here is analogous to the cornering law testing by Helton [112], and the results here fit well ($R^2 = 0.957$) with the cornering law model developed by Pastel [111]. The, in terms of intercept and slope, results show close agreement between the ambient and the dark conditions. This is interpreted to mean that in darkness the human user can tele-operated the mobile robot around a corner with similar performance as ideal lighting conditions. With the inclusion of the bright spot light initially shining toward the camera view, the completion times did not fit the model as well, and this particular lighting and delay condition had the worst fit ($R^2 = 0.890$). This result with the spot light provides an indication that a bright light toward the camera view does have an effect on the tele-operation performance.

Table 7.7: Linear Regression for 0 second time delay.

	R^2	b (s)	m (s/bit)	IP (bit/s)
Ambient lighting	0.957	12.8	10.4	0.096
Bright Spot light	0.890	18.6	6.7	0.149
Dark Condition	0.956	13.9	10.8	0.093

It is worth considering a condition when the corridor width is great enough such that from an initial position the trajectory is nearly a straight line to the final position (the assumption here is that the mobile robot starts positions at an angle, or that the finish line is within the

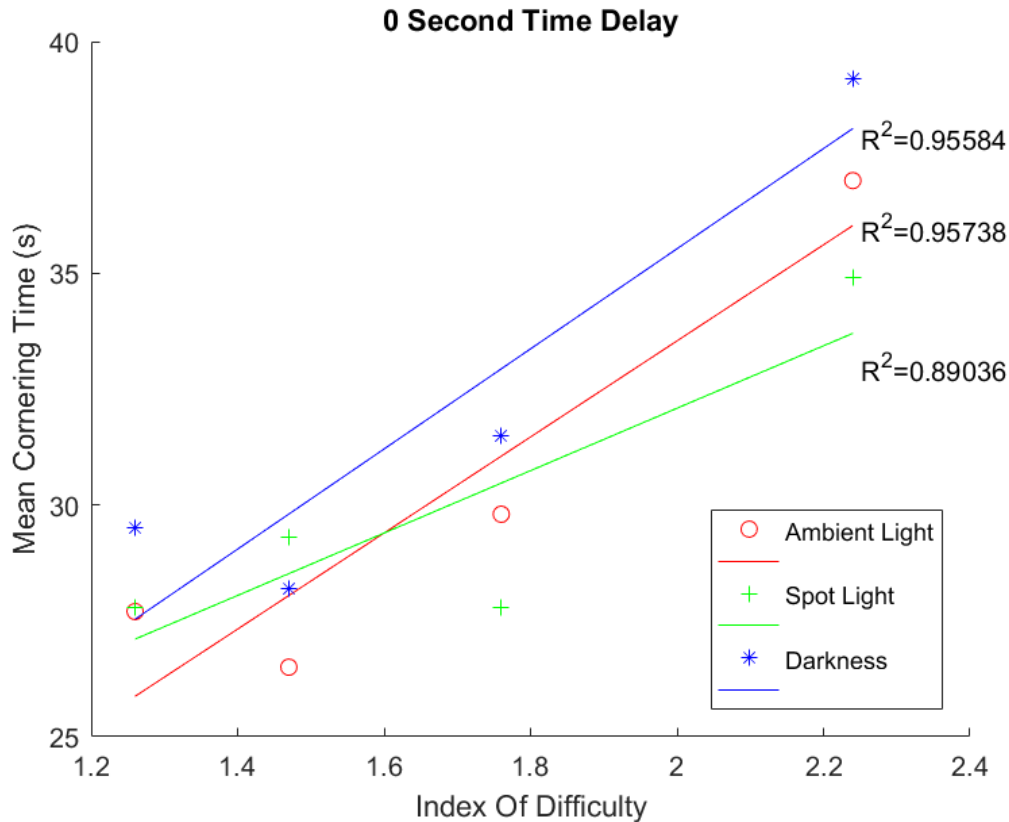


Figure 7.9: Mean time to negotiate corner versus index of difficulty without time delay, where $ID = \log_2\left(\frac{p}{w-p} + 1\right)$.

camera field of view). From the initial position, the human would simply drive straight (or nearly straight with a long radius of curvature) past the inside corner toward the finish line. Considering the simplified geometry puts this distance at approximately 3.5 m. At the set speed of 0.25 m/s this would be completed in approximately 14 seconds, which is slightly greater than the regression-derived values for the limiting cases of no difficulty. The limiting case demonstrates the current results are at least sensible.

Table 7.8 shows the results of linear regression for 2 seconds of time delay, and the mean times are plotted against ID in Figure 7.10. The results show close agreement, in terms of intercept and slope, in between the ambient and the dark conditions. As with no time delay, this is interpreted to mean that in darkness the human user can tele-operated the mobile robot

around a corner with similar performance as ideal lighting conditions with the presence of a 2 second delay. With the inclusion of the bright spot light initially shining toward the camera view, the results fit the model well ($R^2 = 0.992$) however the regression parameters (slope and intercept) were inconsistent with the other two conditions. This result with the spot light provides further indication that a bright light toward the camera view does have an effect on the tele-operation performance.

Table 7.8: Linear Regression for 2 second time delay.

	R^2	b (s)	m (s/bit)	IP (bit/s)
Ambient lighting	0.980	34.3	17.2	0.058
Bright Spot light	0.992	22.1	24.6	0.041
Dark Condition	0.974	37.7	14.2	0.070

Table 7.9 shows the results of linear regression for 4 seconds of time delay, and the mean times are plotted against ID in Figure 7.11. Here the data fit the model well ($R^2 > 0.960$ in each case). However, unlike in the previous two time delay values, there is not a similar consistency between the ambient and dark conditions. This lack of consistency is interpreted to mean that as the delay increases, the lighting condition itself contributes less to tele-operation performance.

Table 7.9: Linear Regression for 4 second time delay.

	R^2	b (s)	m (s/bit)	IP (bit/s)
Ambient lighting	0.964	30.1	33.3	0.030
Bright Spot light	0.973	47.4	22.4	0.045
Dark Condition	0.961	19.0	43.3	0.023

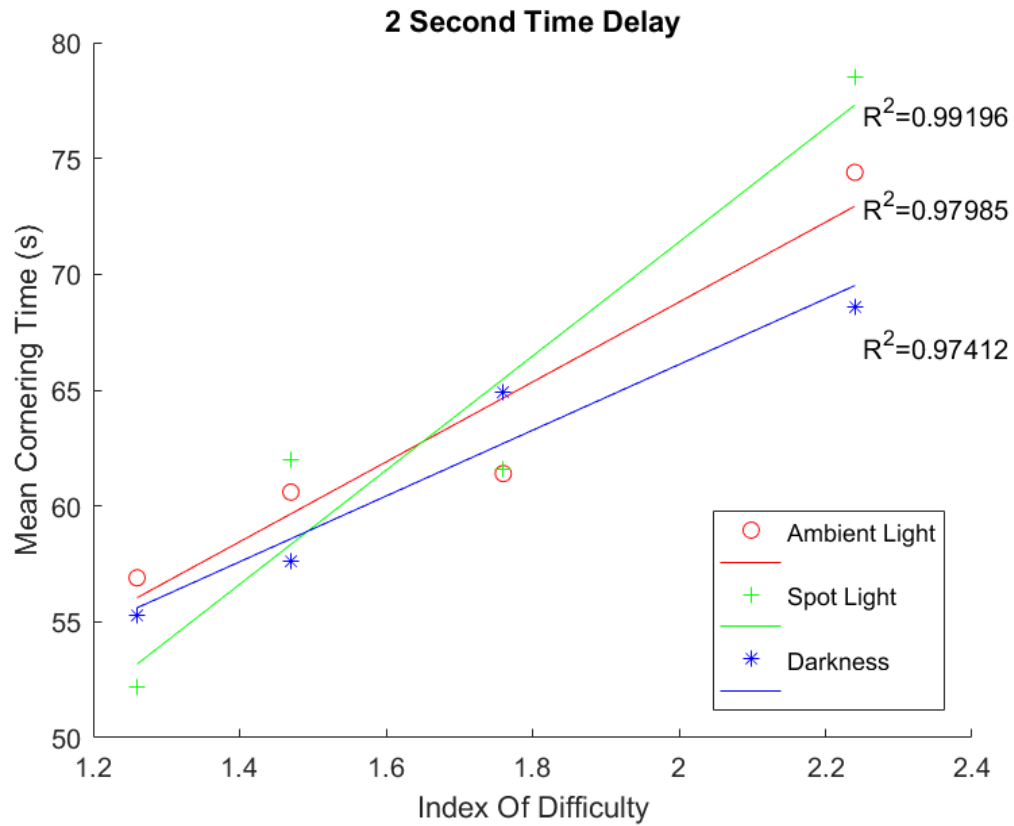


Figure 7.10: Mean time to negotiate corner versus index of difficulty with 2 second time delay, where $ID = \log_2\left(\frac{p}{w-p} + 1\right)$.

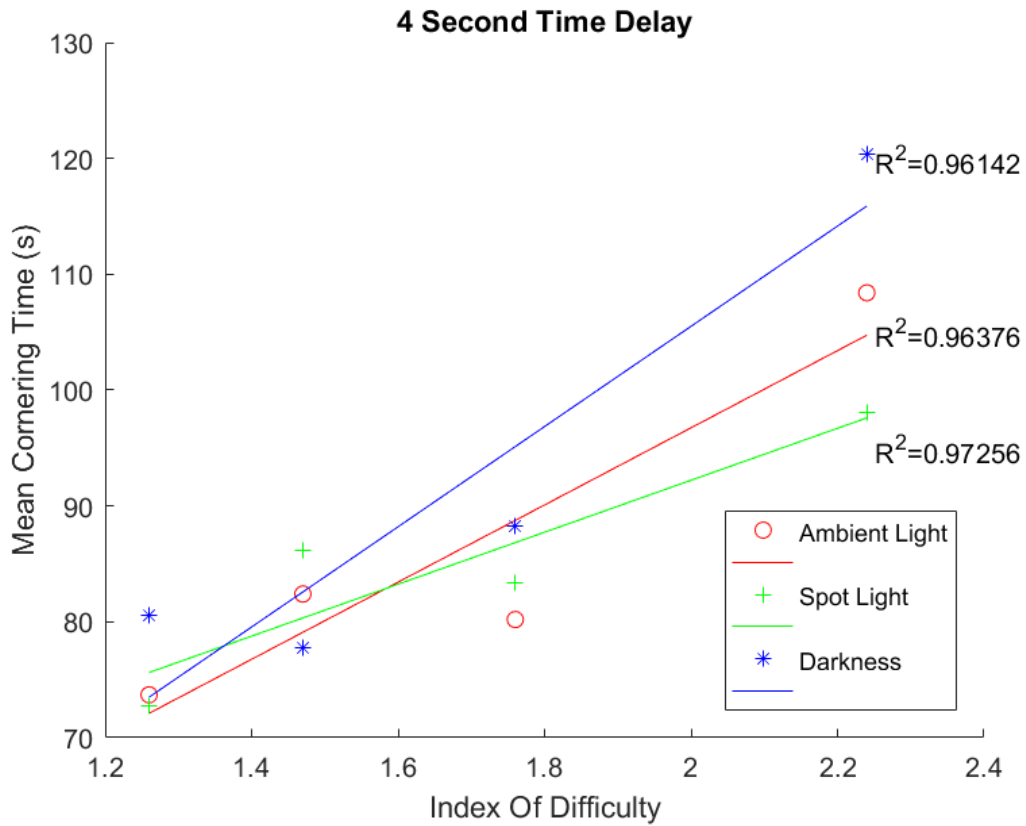


Figure 7.11: Mean time to negotiate corner versus index of difficulty with 4 second time delay, where $ID = \log_2\left(\frac{p}{w-p} + 1\right)$.

Interpretation and Comparison of Time Delay

Table 7.10 shows the results of linear regression for the ambient lighting condition, and the mean times are plotted against ID in Figure 7.12. The data fit the model well ($R^2 > 0.950$), and as the time delay is increased the mean times also increased.

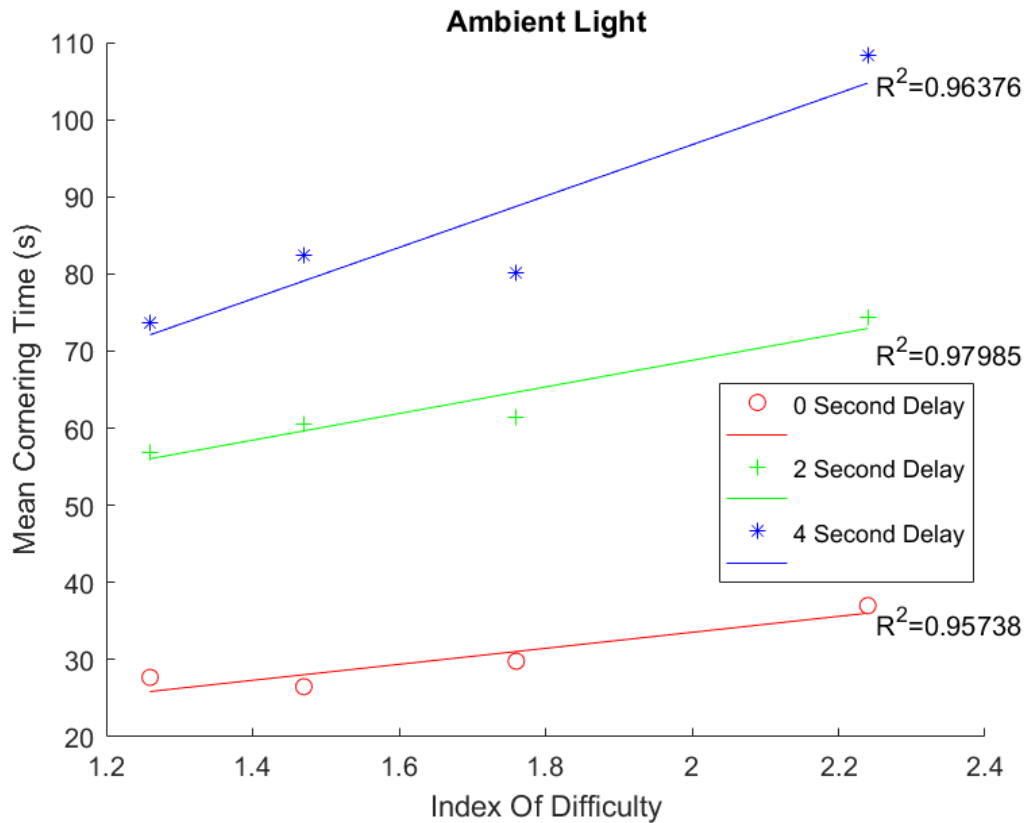


Figure 7.12: Mean time to negotiate corner versus index of difficulty in ambient lighting, where $ID = \log_2\left(\frac{p}{w-p} + 1\right)$.

Table 7.11 shows the results of linear regression for the bright spot light condition, and the mean times are plotted against ID in Figure 7.13. As previously noted, the data for no time delay showed the worst fit, however with delay the data fit the model well ($R^2 > 0.970$). However, as the time delay is increased the mean times also increased.

Table 7.12 shows the results of linear regression for the dark condition, and the mean times are plotted against ID in Figure 7.14. The data fit the model well ($R^2 > 0.950$), however the

Table 7.10: Linear Regression for Ambient Lighting Condition.

	R^2	b (s)	m (s/bit)	IP (bit/s)
0 sec delay	0.957	12.8	10.4	0.096
2 sec delay	0.980	34.3	17.2	0.058
4 sec delay	0.964	30.1	33.3	0.030

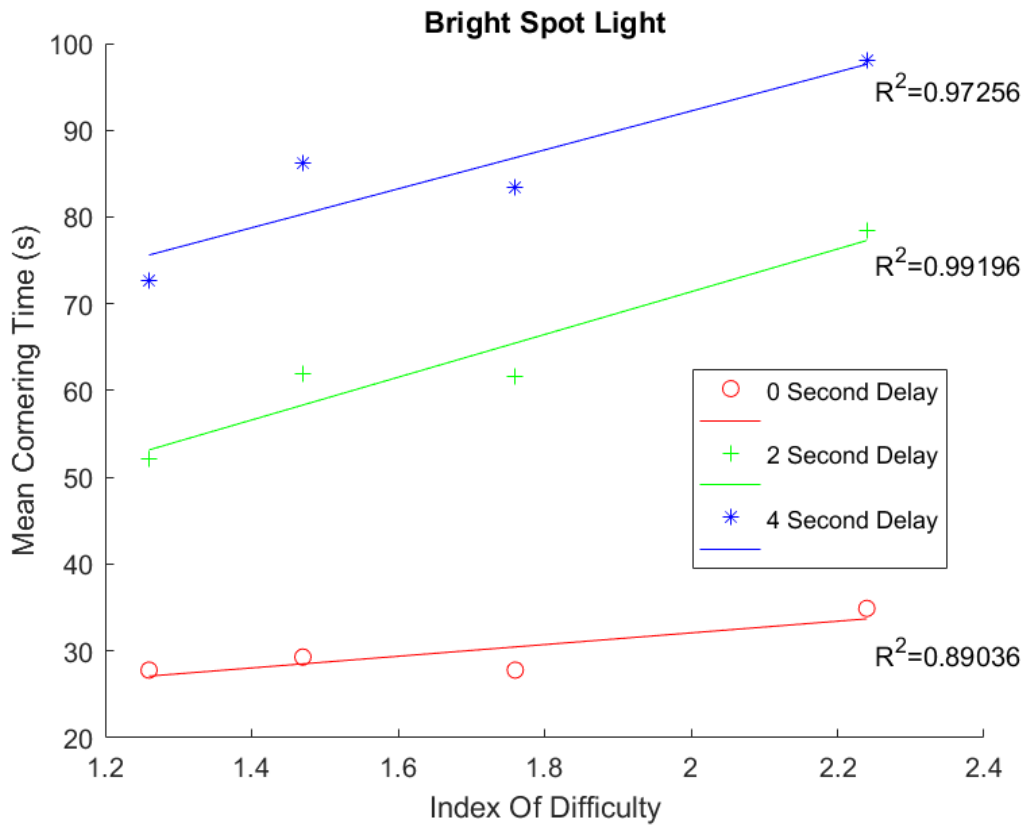


Figure 7.13: Mean time to negotiate corner versus index of difficulty with the bright spot light, where $ID = \log_2\left(\frac{p}{w-p} + 1\right)$.

regression intercept for the 4 second delay is not consistent with the other lighting conditions, which show an increase in time compared to no delay. Similar to the other lighting conditions, as the time delay is increased the mean times also increased.

Table 7.11: Linear Regression for Bright Spot Light Condition.

	R^2	b (s)	m (s/bit)	IP (bit/s)
0 sec delay	0.890	18.6	6.7	0.149
2 sec delay	0.992	22.1	24.6	0.041
4 sec delay	0.973	47.4	22.4	0.045

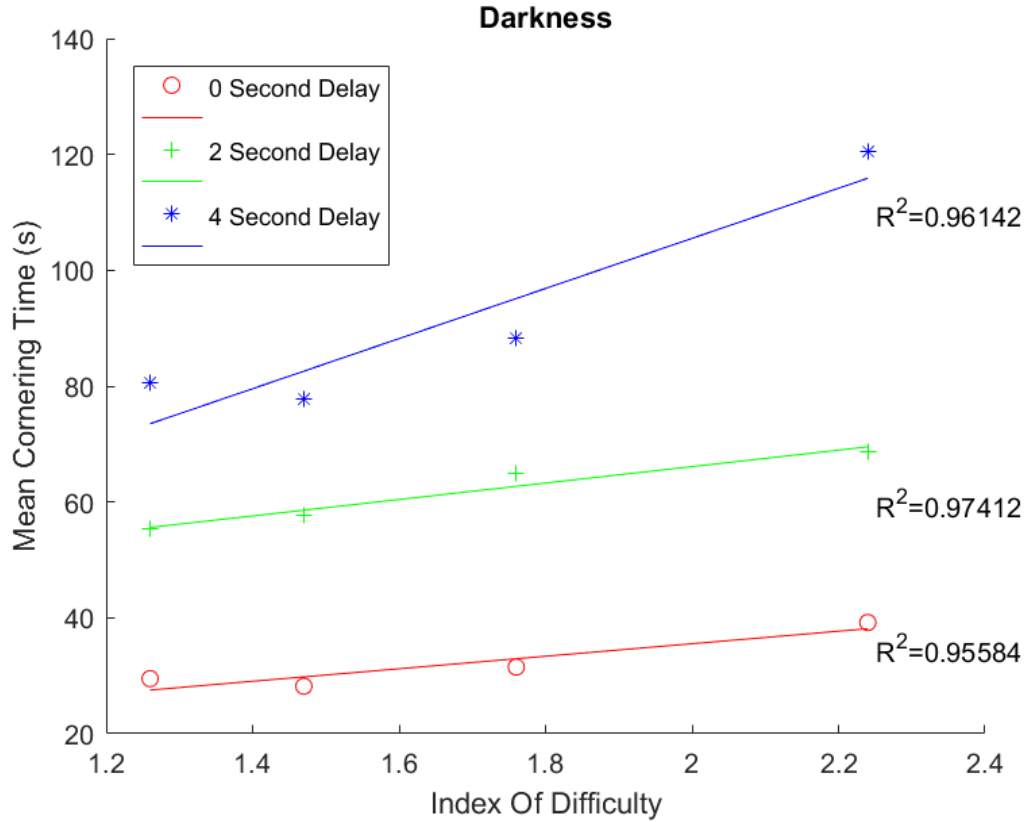


Figure 7.14: Mean time to negotiate corner versus index of difficulty in darkness, where $ID = \log_2\left(\frac{p}{w-p} + 1\right)$.

Table 7.12: Linear Regression for Dark Condition.

	R^2	b (s)	m (s/bit)	IP (bit/s)
0 sec delay	0.956	13.9	10.8	0.093
2 sec delay	0.974	37.7	14.2	0.070
4 sec delay	0.961	19.0	43.3	0.023

Discussion

Mackenzie [104] states that an increased positive intercept value “indicates the presence of an additive factor unrelated to the index of difficulty”. For this thesis the additive factor is considered to be the presence of time delay, as the intercept value is greater for conditions with time delay compared to no delay (with the notable exception of the dark condition at 4 second delay). One observed, but not recorded, tendency for the human testers was to employ a ‘wait and see’ approach for all time delay conditions. The mobile robot was moved either through rotation or translation and then stopped until the video displayed the resultant pose. The duration of movement before a pause varied by human, and increased as the task was learned. The additive factor, and in particular its increase, could be interpreted to be a function of the wait and see approach while negotiating corners.

The times to complete the driving course in Section 7.2 can be re-examined with the additive factor, which is related to the time required to complete the task. The complex driving course had 10 corners to negotiate, noting that all corners were greater or lesser than 90° and both right and left turns. The mean completion time for the ambient condition was 364 s. The cornering law results show that the increase in additive factor from no delay to 4 s delay to be 17.3 s. If this time is interpreted to be an increase in time to complete a corner, then for 10 corners the additional time will be 173 s for a total time of 537 s, which is within 5% of the mean time to complete the course with 4 s delay. The increase in additive factor to 4 s delay with the bright spot light is 34.6 s. For 10 corners the additional time will be 346 s for a total time of 710 s, which is within 5 % of the mean time to complete the course with 4 s delay with the bright spot light.

The same conclusions cannot be made about the change in lighting conditions. The bright spot light had a greater ‘additive factor’ than the dark condition compared as to the ambient condition for both no delay and 4 second delay, whereas it had the smallest intercept value for 2 second delay. Darkness had a greater additive factor compared to the ambient condition with the notable exception at 4 seconds of delay where it had the smallest intercept value.

In Fitts’ Law formulations, and similar formulations modelled on information theory, the

index of difficulty is in units of bits and is considered to the transmitted information, and IP (the inverse of the slope from regression) is the information transmission rate. These two parameters are less intuitive to interpret. Fitts sought to find a the information transmission rate for the tapping test, whereas other studies have examined the role of larger limb group movement [104] to find IP decreased. In other words, more complex human psycho-motor movements to perform the same task reduced the information transmission rate. For this thesis, the trends show that increasing the time delay for the same task results in a decrease in IP , analogous to incorporating additional limbs in the tapping test.

The same conclusions cannot be made about the change in lighting conditions. The bright light with no delay conditions shows the best overall information transmission rate (while noting worst regression fit), and at 4 seconds delay has the best information transmission of the three lighting conditions. At 2 second delay the bright light condition has the lowest transmission rate whereas the dark condition has the highest.

7.4 Limitations and Recommendations

This section describes the limitations to the testing results and interpretations, and recommendations for future testing.

The Elginfield Observatory was ideal in that it afforded the space and isolation needed to complete the data collection. However its remoteness limited access for volunteers and required them to be present for long hours at a time. This overall required time commitment limited the number of human testers available to volunteer for this testing. A greater number of human testers may result in improved data, and improved data may provide a better fit (notably for the bright spot light at no delay).

There is currently no Internet connection at the observatory, however there is a connection to the house at the site, which is connected via VPN to Western University. If the network connection were to be extended to the observatory, and if it were sufficiently stable, human testers could participate remotely from Western campus. The overall time commitment may be the

same, however the testing could be structured to better accommodate participant availability.

The basis for this thesis question is that current limits in computation and communication bandwidth suggest that direct-drive tele-operation is preferred to autonomy for a short-duration south lunar pole prospecting mission. While the bandwidth limitations do currently exist, high-speed (622 Mbps downlink and 20 Mbps uplink) laser-based communication between Earth and the moon was demonstrated on the LADEE mission [117]. The increase in bandwidth will afford far greater spatial awareness data to be transferred to operators on Earth. Conversely, the large volumes of data can be processed on Earth-based computers to enable rover autonomy. The data will still suffer from the round trip time delay, however computationally intensive predictive models can mitigate potential driving hazards.

The monocular camera for video capture was chosen for its availability rather than its utility. The USB web cam is not suitable for the dynamic range of lighting, nor is it wide-angle, which is more standard for mobile robotic applications. A higher quality, wide angle camera with better dynamic range may provide improved video in any of the use cases, which in turn may affect the human performance. Furthermore, planetary rovers current and planned include a number of cameras at different orientations to provide the operator with as much spatial awareness as possible. It is recommended that future tests on cornering law consider including additional cameras to increase spatial awareness. The results of such testing may show the minimum number of camera views required to enable the tele-operator to safely navigate through the corner without collision. Since additional cameras require an increase in data transmission there may be a trade-off between number of camera views and resolution within a bandwidth restriction to limit the error rate while still maintaining vehicle speed.

During the cornering tests it was observed that addition of the bright light resulted in altered depth perception compared to the ambient and dark conditions. Collisions were more likely to occur on the inside corner in ambient and dark conditions, whereas with the bright spot light the collisions occurred with the outer wall. Users reported that the bright light affected their depth perception, and also obscured visual cues used for assessing the mobile robot spatial position with respect to the outer wall. This effect was not predicted and thus data on collision

located was not recorded. It is recommended that future tests on cornering law consider not just the event but also the location of the collision.

Chapter 8

Conclusions and Recommendations

This chapter presents the contributions of the performed work, and recommendations for future directions of research.

8.1 Contributions

The theme for this thesis was an engineering design trade-off study to consider:

Which operating mode, direct-drive tele-operation or supervisory controlled lidar-based autonomy, leads to improved scientific return in the context of a near-term, low-cost, short-duration lunar prospecting mission?

This trade-off study was supported by two research projects, which provide evidence to support the research questions given in Chapter 1.1:

Can lidar reflectance intensity and non-contact spectroscopic measurements improve classification of terrain for rover traverse performance prediction

and

Can the degradation in human performance for tele-operating a rover in non-ideal lighting conditions over time delay fit into Cornering Law?

The following sections outline the supporting evidence for these two questions.

8.1.1 Terrain Classification

The supportive evidence for terrain classification was provided using experimental data collected from a mobile robot and a prototype integrated vision system, and established classification techniques. Background literature on terrain classification for traversability prediction was presented in Chapter 3, where previous studies focused on classifying disparate terrain types with optical images, vehicle vibrations, and acoustics using trained classifiers. Background literature on Naive Bayes and SVM classifiers was presented in Chapter 4, and both classifiers were compared for classification errors. Data collection, processing, and classification were presented in Chapter 6. The results of classification show that the inclusion lidar reflectance intensity values improves both Naive Bayes and SVM classification in all but one case, which was classification of the three bulk composition terrain types. The Naive Bayes resulted in fewer classification errors compared to SVM in all but one case, which was classification of the three bulk composition terrain types. Spectral reflectance features were added to feature vectors to further improve Naive Bayes and SVM classification of four aggregate types.

8.1.2 Tele-Operation Over Time Delay

The supportive evidence for tele-operation performance degradation in non-ideal lighting conditions over time delay was provided using experimental data collected from human testers tele-operating a mobile robot around a corner. Background literature on cornering law, and its origins in Fitts' Law, was presented in Chapter 5. Data collection and analysis were presented in Chapter 7. The results fit within the cornering law model, and time delay was shown to decrease the index of performance and increase the 'additive factor'. The affect of lighting on performance was less conclusive. The additive factor was interpreted to be the increase in time required to tele-operate through a turn.

8.1.3 Lunar South Pole Prospecting Operations Trade-Off

The two primary options for operating a lunar prospecting rover are direct-drive tele-operations, and supervisory-controlled lidar-based autonomous navigation. This thesis examined operating conditions for both operational modes within the context of a low-cost, near-term, short-duration lunar south pole prospecting mission. A near-term mission implies that high-speed laser-based communication will not be available. A low-cost mission implies that existing technologies will be utilized; therefore existing space qualified computers, such as the 200 *MHz* *Curiosity* RCE will be utilized. Short-duration implies that the prospecting must be performed during the 10-14 day lunar day and therefore the speed of the rover should be prioritized in order to maximize the science data return.

For the lidar-based autonomous navigation case, the navigation system must be capable of identifying terrain conditions that may impede the rover's traverse. Lidar can be used to classify geometric obstacles, and utilizing lidar reflectance intensity was shown in this thesis to aid in terrain classification. Lidar is lighting invariant which is beneficial given the harsh lighting conditions anticipating at the lunar south pole. However, lidar-based navigation may be slow, as seen in the *Scarab* terrestrial analogue.

For the direct-drive tele-operation case, the tele-operator must rely upon the delayed video-feedback, which may exhibit harsh lighting. Time delayed video and harsh lighting was shown in this thesis to degrade the drive performance compared to ideal conditions, particularly when turning around obstacles. The results from the cornering studying may show predictive capabilities when plotting out the time to complete complex traverses. Nonetheless, the degraded conditions still resulted in fast traverse speeds compared to what might be expected from a *Scarab*-like autonomous lunar prospecting rover.

8.1.4 Summary of Contributions

1. An engineering trade-off between tele-operation and autonomous navigation for a low-cost, near-term, short-duration lunar south pole prospecting mission.

2. The demonstration of using lidar reflectance intensity to improve terrain classification over just visual images.
3. The demonstration of applying cornering law to time delayed and variable lighting condition tele-operations.

8.2 Future Research Direction

Recommendations for improving the research in this thesis are provided in Chapters 7 and 6. This concluding section provides recommendations and direction of future research.

The research theme for this thesis was a trade-off study between tele-operation and autonomous navigation. A future research project may utilize the Husky in a complex driving course in different lighting conditions and time delay to make a direct comparison to determine which mode, tele-operation or autonomy, results in the fastest time to complete.

8.2.1 Terrain Classification

The original intent for this research was to use spectroscopy to improve classification; lidar was included as it was integrated into the IVS instrument. However, the lidar reflectance was found to be informative in distinguishing between wet and dry sands, and the variance of intensity was found to be informative in distinguishing between densely packed sand and aggregates. Further work with a wider range of soils and terrain types may show lidar reflectance to be useful in identifying conditions such as duricrusts.

The basis for this work was a proposed lunar south pole prospecting mission. Lunar simulant material and representative lunar terrain conditions should be examined with the lidar for classification purposes. This work should also be extended to Martian simulant and representative Martian terrain conditions.

In this thesis the lidar reflectance intensity was shown to improve classification in combination with images taken in ideal lighting conditions. However, lidar features alone resulted in

higher classification errors. Lidar, an active sensing instrument, does not depend on an external light source, which is an argument for using it on south lunar pole prospecting missions in permanently shadowed regions, or any operational setting with variant lighting. One future research direction is to assess the limits of lighting condition on classifications, particularly low-angled light analogous to the south lunar pole.

Low-angled or otherwise poor lighting may prove too challenging for terrain classification incorporating optical images. Terrain classification, using lidar alone, would prove beneficial in such operational conditions. Additional classification techniques may demonstrate reduced errors when utilizing just the lidar reflectance data. Furthermore, the only statistics used for this work were mean and standard deviation for a region within a point cloud. Future work may include statistics on lidar point height information, which may prove to be aid in lidar-only classification.

Proximal soil science techniques and soil inferencing systems may have previously demonstrated the ability to infer soil properties, including mechanical properties, from single measurements. Extending these techniques, with proper equipment, may demonstrate an ability to use a combination of sensors, such as lidar, optical imagery and spectroscopy, to infer soil mechanical and vehicle bearing properties.

8.2.2 Tele-Operation

The cornering law work showed that time-delay and lighting conditions affected the index of performance and ‘additive factor’. This additive factor was interpreted to be an increase in time to make a turn under different conditions. An outdoor course could be set up with well-defined 90 degree turns to test the predictive capability of this interpretation.

The cornering law work utilized a single forward-pointing monocular camera. The work could be replicated replacing optical cameras with a lidar, or other active sensing, to compare the performance. This type of testing may inform the preferred sensing method for a south lunar pole prospecting mission.

The cornering law was developed for ground-based mobile robots negotiating a 2-dimensional

corner. Tele-operated underwater vehicles navigate in 3-dimensions, and the round trip time-delay increases by 1 s per *km* depth. Manoeuvring an underwater vehicle at those depths would be an extension of the 2-D cornering law for mobile robots in poor lighting and over time delay.

Bibliography

- [1] B. H. Wilcox. “Non-Geometric Hazard Detection for a Mars Micro rover.” Technical report, Jet Propulsion Laboratory, Houston, Texas, USA (1994).
- [2] A. Colaprete, R. C. Elphic, D. Andrews, G. Sanders, A. McGovern, R. Vaughan, J. Heldmann, and J. Trimble. “Resource Prospector: Mission Goals, Relevance and Site Selection.” *Lunar Exploration Analysis Group (2015)* pages 1–2 (2015).
- [3] J. D. Carpenter, R. Fisackerly, S. Aziz, and B. Houdou. “Exploring Cold Trapped Volatiles From Stationary Platforms And Mobile Rovers: ESA Activities For Resource Prospecting At The Poles.” *Lunar Exploration Analysis Group (2015)* (2015).
- [4] D. Shirley and J. Matijevic. “Mars Pathfinder Micro rover.” *Autonomous Robots* **2**(4), 283–289. ISSN 0929-5593 (1995).
- [5] R. E. Arvidson, J. F. Bell, P. Bellutta, N. A. Cabrol, J. G. Catalano, J. Cohen, L. S. Crumpler, D. J. Des Marais, T. A. Estlin, W. H. Farrand, R. Gellert, J. A. Grant, R. N. Greenberger, E. A. Guinness, K. E. Herkenhoff, J. A. Herman, K. D. Iagnemma, J. R. Johnson, G. Klingelhöfer, R. Li, K. A. Lichtenberg, S. A. Maxwell, D. W. Ming, R. V. Morris, M. S. Rice, S. W. Ruff, A. Shaw, K. L. Siebach, P. A. de Souza, A. W. Stroupe, S. W. Squyres, R. J. Sullivan, K. P. Talley, J. A. Townsend, A. Wang, J. R. Wright, and A. S. Yen. “Spirit Mars Rover Mission: Overview and selected results from the northern Home Plate Winter Haven to the side of Scamander crater.” *Journal of Geophysical Research* **115**. ISSN 0148-0227 (2010).

- [6] S. W. Squyres, R. E. Arvidson, D. Bollen, J. F. Bell, J. Brückner, N. A. Cabrol, W. M. Calvin, M. H. Carr, P. R. Christensen, B. C. Clark, L. Crumpler, D. J. Des Marais, C. D’Uston, T. Economou, J. Farmer, W. H. Farrand, W. Folkner, R. Gellert, T. D. Glotch, M. Golombek, S. Gorevan, J. A. Grant, R. Greeley, J. Grotzinger, K. E. Herkenhoff, S. Hviid, J. R. Johnson, G. Klingelhöfer, A. H. Knoll, G. Landis, M. Lemmon, R. Li, M. B. Madsen, M. C. Malin, S. M. McLennan, H. Y. McSween, D. W. Ming, J. Moersch, R. V. Morris, T. Parker, J. W. Rice, L. Richter, R. Rieder, C. Schröder, M. Sims, M. Smith, P. Smith, L. A. Soderblom, R. Sullivan, N. J. Tosca, H. Wänke, T. Wdowiak, M. Wolff, and A. Yen. “Overview of the Opportunity Mars Exploration Rover Mission to Meridiani Planum: Eagle Crater to Purgatory Ripple.” *Journal of Geophysical Research* **111**(E12). ISSN 0148-0227 (2006).
- [7] B. Muirhead. “Mars rovers, past and future.” *2004 IEEE Aerospace Conference Proceedings (IEEE Cat. No.04TH8720)* pages 128–134. IEEE. ISBN 0-7803-8155-6.
- [8] T. P. Rivellini. “Mars rover mechanisms designed for Rocky 4.” *The 27th Aerospace Mechanisms Symposium* (1993).
- [9] J. Chottiner. “Simulation of a Six Wheel Martian Rover Called the Rocker Bogie.” Msc thesis, The Ohio State University (1992).
- [10] M. Cross, A. Ellery, and A. Qadi. “Estimating terrain parameters for a rigid wheeled rover using neural networks.” *Journal of Terramechanics* **50**(3), 165–174. ISSN 00224898 (2013).
- [11] J. F. Mustard, M. Adler, A. Allwood, D. S. Bass, D. W. Beaty, J. F. Bell, W. B. Brinckerhoff, M. Carr, D. J. D. Marais, B. Drake, K. S. Edgett, J. A. Grant, S. M. Milkovich, D. Ming, S. Murchie, T. C. Onstott, S. W. Ruff, M. A. Sephton, A. Steele, B. Drake, K. S. Edgett, J. Eigenbrode, J. A. Grant, S. M. Milkovich, and D. Ming. “Report of the Mars 2020 Science Definition Team.” Technical report (2013).

- [12] G. R. Osinski, R. Francis, T. Haltigin, M. C. Kerrigan, A. Pontefract, E. A. Silber, and L. L. Tornebene. “Overview of the 2015 CanMars Mars Sample Return Analogue Mission.” *47th Lunar and Planetary Science Conference* (2016).
- [13] M. D. Cross, I. M. Pritchard, R. Francis, and G. R. Osinski. “Science Activity Resource Planning for 2015 CanMars MSR Analogue Mission.” *47th Lunar and Planetary Science Conference* (2016).
- [14] R. Francis, M. D. Cross, M. C. Kerrigan, and G. R. Osinski. “Exploration and Decision-Making Rules and Resources on the 2015 CanMars MSR Analogue Mission: An Analogue for Mars 2020 Rover Operations.” *47th Lunar and Planetary Science Conference* (2016).
- [15] M. C. Kerrigan and G. R. Osinski. “2015 CanMars MSR Analogue Mission: Mission Control Team Structure and Operations.” *47th Lunar and Planetary Science Conference* (2016).
- [16] E. A. Silber, G. R. Osinski, R. Francis, M. D. Cross, and I. M. Pritchard. “2015 CanMars MSR Analogue Mission: An Overview of the Mission Control Tactical Team.” *47th Lunar and Planetary Science Conference* (2016).
- [17] G. B. Sanders, L. Moore, D. S. McKay, T. M. Simon, D. E. Lueck, C. F. Parrish, K. R. Johnson, G. Mungas, M. Pelletier, K. Sacksteder, M. Duke, J. Taylor, L. Taylor, and D. Boucher. “Regolith & Environment Science , and Oxygen & Lunar Volatile Extraction (RESOLVE) for Robotic Lunar Polar Lander Mission.” *International Lunar Conference 2005* pages 1–16 (2005).
- [18] J. Quinn, J. Smith, J. Captain, A. Paz, A. Colaprete, R. Elphic, and K. Zacny. “Resource Prospector: The RESOLVE Payload.” *Lunar Exploration Analysis Group (2015)* (2015).
- [19] B. Harvey. *Soviet and Russian Lunar Exploration*. Springer Praxis Books. Praxis, New York, NY. ISBN 978-0-387-21896-0 (2007).

- [20] T. Sheridan. “Space teleoperation through time delay: review and prognosis.” *IEEE Transactions on Robotics and Automation* **9**(5), 592–606. ISSN 1042296X (1993).
- [21] W.-H. Ip, J. Yan, C.-L. Li, and Z.-Y. Ouyang. “Preface: The Chang’e-3 lander and rover mission to the Moon.” *Research in Astronomy and Astrophysics* **14**(12), 1511–1513. ISSN 1674-4527 (2014).
- [22] Z. Liu, K. Di, M. Peng, W. Wan, B. Liu, L. Li, T. Yu, B. Wang, J. Zhou, and H. Chen. “High precision landing site mapping and rover localization for Chang’e-3 mission.” *Science China Physics, Mechanics & Astronomy* **58**(1), 1–11. ISSN 1674-7348 (2015).
- [23] D. Wettergreen, D. Jonak, D. Kohanbash, S. Moreland, S. Spiker, J. Teza, and W. Whitaker. “Design and Experimentation of a Rover Concept for Lunar Crater Resource Survey.” *47th AIAA Aerospace Sciences Meeting Including The New Horizons Forum and Aerospace Exposition* pages 1–8 (2009).
- [24] D. Wettergreen, S. Moreland, K. Skonieczny, D. Jonak, D. Kohanbash, and J. Teza. “Design and field experimentation of a prototype Lunar prospector.” *The International Journal of Robotics Research* **29**(12), 1550–1564. ISSN 0278-3649 (2010).
- [25] A. Winterholler, M. Roman, T. Hunt, and D. Miller. “Design of a high-mobility low-weight lunar rover.” *International Symposium on Artificial Intelligence, Robotics and Automation in Space* Figure 1, pages 1–6. Munich (2005).
- [26] D. P. Miller and K. Machulis. “Visual aids for lunar rover tele-operation.” *International Symposium on Artificial Intelligence, Robotics and Automation in Space* pages 1–6. Munich (2005).
- [27] L. Pedersen, M. Allan, V. To, H. Utz, W. Wojcikiewicz, and C. Chautems. “High Speed Lunar Navigation for Crewed and Remotely Piloted Vehicles.” *i-SAIRAS* pages 600–607. Sapporo (2010).

- [28] L. Pedersen, M. Allan, H. Utz, M. Deans, X. Bouyssououse, Y. Choi, L. Fluckiger, S. Y. Lee, V. To, J. Loh, W. Bluethmann, R. R. Burrige, J. Graf, and K. Hambuchen. “Tele-Operated Lunar Rover Navigation Using LIDAR.” *i-SAIRAS Milano* (2012).
- [29] M. Bajracharya, M. W. Maimone, and D. Helmick. “Autonomy for Mars Rovers: Past, present, and future.” *Computer* **41**(12), 44–50. ISSN 00189162 (2008).
- [30] A. Kemurdjian. “Experience in Creating Self Propelled Undercarriages for Planet Rovers.” *Journal of Aerospace Engineering* **4**(4), 317–329. ISSN 0893-1321 (1991).
- [31] A. Mishkin, J. Morrison, T. Nguyen, H. Stone, B. Cooper, and B. Wilcox. “Experiences with operations and autonomy of the Mars Pathfinder Microrover.” *1998 IEEE Aerospace Conference Proceedings (Cat. No.98TH8339)* volume 2, pages 337–351. IEEE. ISBN 0-7803-4311-5.
- [32] P. Leger, A. Trebi-Ollennu, J. Wright, S. Maxwell, R. Bonitz, J. Biesiadecki, F. Hartman, B. Cooper, E. Baumgartner, and M. Maimone. “Mars Exploration Rover Surface Operations: Driving Spirit at Gusev Crater.” *2005 IEEE International Conference on Systems, Man and Cybernetics* volume 2, pages 1815–1822. IEEE. ISBN 0-7803-9298-1.
- [33] A. Ellery. *Planetary Rovers*. Springer Berlin Heidelberg, Berlin, Heidelberg. ISBN 978-3-642-03258-5 (2016).
- [34] J. P. Grotzinger, J. Crisp, A. R. Vasavada, R. C. Anderson, C. J. Baker, R. Barry, D. F. Blake, P. Conrad, K. S. Edgett, B. Ferdowski, R. Gellert, J. B. Gilbert, M. Golombek, J. Gómez-Elvira, D. M. Hassler, L. Jandura, M. Litvak, P. Mahaffy, J. Maki, M. Meyer, M. C. Malin, I. Mitrofanov, J. J. Simmonds, D. Vaniman, R. V. Welch, and R. C. Wiens. “Mars Science Laboratory Mission and Science Investigation.” *Space Science Reviews* **170**(1-4), 5–56. ISSN 0038-6308 (2012).
- [35] J. Vago, O. Witasse, H. Svedhem, P. Baglioni, A. Haldemann, G. Gianfiglio, T. Blancquaert, D. McCoy, and R. de Groot. “ESA ExoMars program: The next step in exploring Mars.” *Solar System Research* **49**(7), 518–528. ISSN 0038-0946 (2015).

- [36] M. Winter, C. Barclay, V. Pereira, R. Lancaster, M. Caceres, K. McManamon, B. Nye, N. Silva, D. Lachat, and M. Campana. “ExoMars Rover Vehicle: Detailed Description of the GNC System.” *ASTRA* (2015).
- [37] S. M. Clegg, R. C. Wiens, S. Maurice, O. Gasnault, S. K. Sharma, A. K. Misra, R. Newell, O. Forni, J. Lasue, R. B. Anderson, K. L. Nowak-Lovato, T. Fouchet, S. M. Angel, F. Rull, J. R. Johnson, and SuperCam Science Team. “Remote Geochemical and Mineralogical Analysis with SuperCam for the Mars 2020 Rover.” *Lunar and Planetary Science Conference* page 2781 (2015).
- [38] G. A. Landis, R. Dyson, S. J. Oleson, J. D. Warner, and A. J. Colozza. “Venus Rover Design Study.” *AIAA SPACE 2011 Conference and Exposition* September, pages 1–14 (2011).
- [39] G. A. Landis, R. Dyson, M. Mcguire, S. J. Oleson, G. R. Schmidt, J. Grantier, L. M. Burke, I. J. Dux, M. J. Bur, J. Fincannon, K. M. Bury, M. Mongalier, L. Glenn, J. D. Warner, T. W. Packard, A. J. Colozza, M. C. Martini, and J. E. Fittje. “Human Telerobotic Exploration of Venus : A Flexible Path Design Study.” *49th AIAA Aerospace Sciences Meeting* January, pages 1–17 (2011).
- [40] S. R. Oleson and M. V. Paul. “Titan Submarine : Exploring The Depths of Kraken Mare.” *AIAA SPACE 2015 Conference and Exposition* pages 1–15 (2015).
- [41] T. Bayer, B. Cooke, I. Gontijo, and K. Kirby. “Europa Clipper mission: the habitability of an icy moon.” *2015 IEEE Aerospace Conference* pages 1–12. IEEE. ISBN 978-1-4799-5379-0 (2015).
- [42] R. T. Pappalardo, D. Senske, L. Prockter, B. Paczkowski, S. Vance, A. Rhoden, B. Goldstein, T. Magner, and B. Cooke. “Science Objectives for the Europa Clipper Mission Concept: Investigating the Potential Habitability of Europa.” *European Planetary Science Congress* (2015).

- [43] L. V. Zasova, N. I. Ignatiev, and M. V. Gerasimov. “Future Venus Exploration: Mission Venera-D.” *Venus Exploration Targets Workshop* (2014).
- [44] J.-P. Lebreton, O. Witasse, C. Sollazzo, T. Blancquaert, P. Couzin, A.-M. Schipper, J. B. Jones, D. L. Matson, L. I. Gurvits, D. H. Atkinson, B. Kazeminejad, and M. Pérez-Ayúcar. “An overview of the descent and landing of the Huygens probe on Titan.” *Nature* **438**(7069), 758–764. ISSN 0028-0836 (2005).
- [45] M. Bekker. *Introduction to Terrain-Vehicle Systems*. University of Michigan Press (1969).
- [46] J. Y. Wong. *Theory of Ground Vehicles*. John Wiley & Sons, 4th edition. ISBN 0-470-17038-7 (2008).
- [47] J. Y. Wong. *Terramechanics and Off-Road Vehicle Engineering*. Elsevier, 2nd edition. ISBN 9780750685610 (2010).
- [48] N. C. Costes, J. E. Farmer, G. C. Marshall, and S. Flight. “MOBILITY PERFORMANCE OF THE LUNAR ROVING VEHICLE : TERRESTRIAL STUDIES - APOLLO 15 RESULTS.” *Apollo The International Magazine Of Art And Antiques* (December) (1972).
- [49] V. Asnani, D. Delap, and C. Creager. “The development of wheels for the Lunar Roving Vehicle.” *Journal of Terramechanics* **46**(3), 89–103. ISSN 00224898 (2009).
- [50] H. Shibly, K. Iagnemma, and S. Dubowsky. “An equivalent soil mechanics formulation for rigid wheels in deformable terrain, with application to planetary exploration rovers.” *Journal of Terramechanics* **42**(1), 1–13. ISSN 00224898 (2005).
- [51] K. Iagnemma, H. Shibly, and S. Dubowsky. “On-line terrain parameter estimation for planetary rovers.” *Proceedings 2002 IEEE International Conference on Robotics and Automation (Cat. No.02CH37292)* volume 3, pages 3142–3147. IEEE. ISBN 0-7803-7272-7 (2002).

- [52] K. Iagnemma and S. Dubowsky. *Mobile Robots in Rough Terrain: Estimation, Motion Planning, and Control with Application to Planetary Rovers*, volume 12. Springer, star edition. ISBN 3-540-21968-4 (2004).
- [53] C. Tan, Y. Zweiri, K. Althoefer, and L. Seneviratne. “Online Soil Parameter Estimation Scheme Based on NewtonRaphson Method for Autonomous Excavation.” *IEEE/ASME Transactions on Mechatronics* **10**(2), 221–229. ISSN 1083-4435 (2005).
- [54] R. Yousefi Moghaddam, A. Kotchon, and M. Lipsett. “Method and apparatus for on-line estimation of soil parameters during excavation.” *Journal of Terramechanics* **49**(3-4), 173–181. ISSN 00224898 (2012).
- [55] G. Reina, L. Ojeda, A. Milella, and J. Borenstein. “Wheel slippage and sinkage detection for planetary rovers.” *IEEE/ASME Transactions on Mechatronics* **11**(2), 185–195. ISSN 1083-4435 (2006).
- [56] A. Angelova, L. Matthies, D. Helmick, and P. Perona. “Learning and prediction of slip from visual information.” *Journal of Field Robotics* **24**(3), 205–231. ISSN 15564959 (2007).
- [57] T. Leung and J. Malik. “Representing and Recognizing the Visual Appearance of Materials using Three-dimensional Textons.” *International Journal of Computer Vision* **43**(1), 29–44. ISSN 09205691 (2001).
- [58] C. Brooks and K. Iagnemma. “Vibration-based terrain classification for planetary exploration rovers.” *IEEE Transactions on Robotics* **21**(6), 1185–1191. ISSN 1552-3098 (2005).
- [59] C. A. Brooks and K. D. Iagnemma. “Self-Supervised Classification for Planetary Rover Terrain Sensing.” *2007 IEEE Aerospace Conference* pages 1–9. IEEE. ISBN 1-4244-0524-6 (2007).

- [60] I. Halatci, C. A. Brooks, and K. Iagnemma. "Terrain Classification and Classifier Fusion for Planetary Exploration Rovers." *2007 IEEE Aerospace Conference* pages 1–11. IEEE. ISBN 1-4244-0524-6 (2007).
- [61] A. Kleiner. "Online learning terrain classification for adaptive velocity control." *2010 IEEE Safety Security and Rescue Robotics* pages 1–7. IEEE. ISBN 978-1-4244-8898-8 (2010).
- [62] C. A. Brooks and K. Iagnemma. "Self-supervised terrain classification for planetary surface exploration rovers." *Journal of Field Robotics* **29**(3), 445–468. ISSN 15564959 (2012).
- [63] J. Libby. "Thesis Proposal." (2012).
- [64] D. Michel. *System of terrain analysis, energy estimation and path planning for planetary exploration by robot teams*. Phd, University of Western Ontario (2013).
- [65] R. A. Viscarra Rossel, A. B. McBratney, and B. Minasny, editors. *Proximal Soil Sensing*. Springer Netherlands, Dordrecht. ISBN 978-90-481-8858-1 (2010).
- [66] V. Adamchuk and R. V. Rossel. "Development of On-the-Go Proximal Soil Sensor Systems." R. A. Viscarra Rossel, A. B. McBratney, and B. Minasny, editors, *Proximal Soil Sensing* chapter 2, pages 15–28. Springer Netherlands, Dordrecht. ISBN 978-90-481-8859-8 (2010).
- [67] A. B. McBratney, B. Minasny, and R. Viscarra Rossel. "Spectral soil analysis and inference systems: A powerful combination for solving the soil data crisis." *Geoderma* **136**(1-2), 272–278. ISSN 00167061 (2006).
- [68] R. S. Harmon, F. C. De Lucia, A. W. Miziolek, K. L. McNesby, R. A. Walters, and P. D. French. "Laser-induced breakdown spectroscopy (LIBS) - an emerging field-portable sensor technology for real-time, in-situ geochemical and environmental analysis." *Geochemistry: Exploration, Environment, Analysis* **5**(1), 21–28. ISSN 1467-7873 (2005).

- [69] S. Grunwald, J. A. Thompson, and J. L. Boettinger. “Digital Soil Mapping and Modeling at Continental Scales: Finding Solutions for Global Issues.” *Soil Science Society of America Journal* **75**(4), 1201. ISSN 0361-5995 (2011).
- [70] K. Stelmazczyk, P. Rohwetter, G. Mejean, J. Yu, E. Salmon, J. Kasparian, R. Ackermann, J.-P. Wolf, and L. Woste. “Long-distance remote laser-induced breakdown spectroscopy using filamentation in air.” *Applied Physics Letters* **85**(18), 3977. ISSN 00036951 (2004).
- [71] C. Cunningham, U. Wong, K. Peterson, and W. Whittaker. “Predicting Terrain Traversability from Thermal Diffusivity.” L. Mejias, P. Corke, and J. Roberts, editors, *Field and Service Robotics SE - 5* volume 105 of *Springer Tracts in Advanced Robotics*, pages 61–74. Springer International Publishing. ISBN 978-3-319-07487-0 (2015).
- [72] D. Burton, D. B. Dunlap, L. J. Wood, and P. P. Flaig. “Lidar Intensity as a Remote Sensor of Rock Properties.” (2011).
- [73] A. Suvinen and M. Saarilahti. “Measuring the mobility parameters of forwarders using GPS and CAN bus techniques.” *Journal of Terramechanics* **43**(2), 237–252. ISSN 00224898 (2006).
- [74] T. P. Setterfield and A. Ellery. “Terrain Response Estimation Using an Instrumented Rocker-Bogie Mobility System.” *IEEE Transactions on Robotics* **29**(1), 172–188. ISSN 1552-3098 (2013).
- [75] A. B. McBratney, B. Minasny, S. R. Cattle, and R. Vervoort. “From pedotransfer functions to soil inference systems.” *Geoderma* **109**(1-2), 41–73. ISSN 00167061 (2002).
- [76] J. Bouma. “Using Soil Survey Data for Quantitative Land Evaluation.” B. A. Stewart, editor, *Advances in Soil Science* volume 9 of *Advances in Soil Science*, pages 177–213. Springer US, New York, NY. ISBN 978-1-4612-8144-3 (1989).

- [77] J. L. Boettinger, D. W. Howell, A. C. Moore, A. E. Hartemink, and S. Kienast-Brown, editors. *Digital Soil Mapping*. Springer Netherlands, Dordrecht. ISBN 978-90-481-8862-8 (2010).
- [78] S. Grunwald. “Multi-criteria characterization of recent digital soil mapping and modeling approaches.” *Geoderma* **152**(3-4), 195–207. ISSN 00167061 (2009).
- [79] F. A. Kruse. “Mapping surface mineralogy using imaging spectrometry.” *Geomorphology* **137**, 41–56. ISSN 0169555X (2012).
- [80] A. Suvinen. “A GIS-based simulation model for terrain tractability.” *Journal of Terramechanics* **43**(4), 427–449. ISSN 00224898 (2006).
- [81] A. Hohmann, G. Grandjean, V. Mardhel, G. Schaefer, and N. Desramaut. “A GIS-based Vehicle Mobility Estimator for Operational Contexts.” *Transactions in GIS* **17**(1), 78–95. ISSN 13611682 (2013).
- [82] W.-I. Park, D.-J. Kim, and H.-J. Lee. “Terrain trafficability analysis for autonomous navigation: A GIS-based approach.” *International Journal of Control, Automation and Systems* **11**(2), 354–361. ISSN 1598-6446 (2013).
- [83] K. a. Lichtenberg, R. E. Arvidson, F. Poulet, R. V. Morris, A. Knudson, J. F. Bell, G. Bellucci, J.-P. Bibring, W. H. Farrand, J. R. Johnson, D. W. Ming, P. C. Pinet, a. D. Rogers, and S. W. Squyres. “Coordinated analyses of orbital and Spirit Rover data to characterize surface materials on the cratered plains of Gusev Crater, Mars.” *Journal of Geophysical Research* **112**(E12), E12S90. ISSN 0148-0227 (2007).
- [84] K. Lichtenberg. *Remote Sensing and Terramechanics Study of Mars using Orbital and Rover Data Sets*. Ph.D. thesis, Washington University in St. Louis (2010).
- [85] J. Wong. “Predicting the performances of rigid rover wheels on extraterrestrial surfaces based on test results obtained on earth.” *Journal of Terramechanics* **49**(1), 49–61. ISSN 00224898 (2011).

- [86] R. Team. “Characterization of the Martian Surface Deposits by the Mars Pathfinder Rover, Sojourner.” *Science* **278**(5344), 1765–1768. ISSN 00368075 (1997).
- [87] H. J. Moore, D. B. Bickler, J. A. Crisp, H. J. Eisen, J. A. Gensler, A. F. C. Haldemann, J. R. Matijevic, L. K. Reid, and F. Pavlics. “Soil-like deposits observed by Sojourner, the Pathfinder rover.” *Journal of Geophysical Research* **104**(E4), 8729–8746. ISSN 0148-0227 (1999).
- [88] R. E. Arvidson, J. L. Gooding, and H. J. Moore. “The Martian surface as imaged, sampled, and analyzed by the Viking landers.” *Reviews of Geophysics* **27**(1), 39. ISSN 8755-1209 (1989).
- [89] A. Shaw, R. E. Arvidson, R. Bonitz, J. Carsten, H. U. Keller, M. T. Lemmon, M. T. Mellon, M. Robinson, and A. Trebi-Ollennu. “Phoenix soil physical properties investigation.” *Journal of Geophysical Research* **114**. ISSN 0148-0227 (2009).
- [90] R. Sullivan, R. Anderson, J. Biesiadecki, T. Bond, and H. Stewart. “Cohesions, friction angles, and other physical properties of Martian regolith from Mars Exploration Rover wheel trenches and wheel scuffs.” *Journal of Geophysical Research* **116**(E2). ISSN 0148-0227 (2011).
- [91] G. H. Heiken, D. T. Vaniman, and B. M. French, editors. *Lunar Sourcebook: A User’s Guide to the Moon*. Cambridge University Press. ISBN 0521334446 (1991).
- [92] A. R. Webb and K. D. Copsey. *Statistical Pattern Classification*. John Wiley & Sons, 3rd edition (2011).
- [93] D. D. Lewis. “Naive (Bayes) at Forty: The Independence Assumption in Information Retrieval.” *European Conference on Machine Learning* pages 4–15 (1998).
- [94] I. Rish. “An empirical study of the Naive Bayes Classifier.” *IJCAI 2001 workshop on empirical methods in artificial intelligence* **3**(22), 41–46 (2001).

- [95] D. W. Hainsworth. “Teleoperation User Interfaces for Mining Robotics.” pages 19–28 (2001).
- [96] C. Preusche and G. Hirzinger. “Telerobotics.” B. Siciliano and O. Khatib, editors, *Springer Handbook of Robotics* pages 741–757. Springer Berlin Heidelberg. ISBN 978-3-540-23957-4 (2008).
- [97] H. Mano, K. Kon, N. Sato, M. Ito, H. Mizumoto, K. Goto, R. Chatterjee, and F. Matsuno. “Treaded control system for rescue robots in indoor environment.” *2008 IEEE International Conference on Robotics and Biomimetics* pages 1836–1843 (2009).
- [98] Q. Lin. “Virtual Tele-Operation of Underwater Robots.” (April), 1022–1027 (1997).
- [99] M. Pickett and D. Lane. “Tele-assistance task planning for dextrous underwater manipulation.” *IEEE Oceanic Engineering Society. OCEANS’98. Conference Proceedings (Cat. No.98CH36259)* **1**, 200–204 (1998).
- [100] C. Sayers, R. Paul, L. Whitcomb, and D. Yoerger. “Teleprogramming for subsea teleoperation using acoustic communication.” *IEEE Journal of Oceanic Engineering* **23**(1), 60–71. ISSN 03649059 (1998).
- [101] P. Arcara and C. Melchiorri. “Control schemes for teleoperation with time delay: A comparative study.” *Robotics and Autonomous Systems* **38**(1), 49–64. ISSN 09218890 (2002).
- [102] M. Cardone, C. Laroque, M. Sarkarati, K. Nergaard, P. Steele, and S. Martin. “The METERON Operations Environment and Robotic Services, a plug-and-play system infrastructure for Robotic experiments.” *SpaceOps 2016 Conference* American Institute of Aeronautics and Astronautics, Reston, Virginia. ISBN 978-1-62410-426-8 (2016).
- [103] C. E. Shannon. “Communication Theory of Secrecy Systems.” *Bell System Technical Journal* **28**(4), 656–715 (1949).

- [104] I. S. Mackenzie. "Fitts' Law as a Research and Design Tool in Human-Computer Interaction." **7**, 91–139 (1992).
- [105] S. K. Card, W. K. English, and B. J. Burr. "Evaluation of Mouse, Rate-Controlled Isometric Joystick, Step Keys, and Text Keys for Text Selection on a CRT." *Ergonomics* **21**(8), 601–613 (1977).
- [106] L. Rosenberg. "The use of virtual fixtures as perceptual overlays to enhance operator performance in remote environments." Technical report, ARMSTRONG LAB WRIGHT-PATTERSON AFB OH CREW SYSTEMS DIRECTORATE (1992).
- [107] I. S. Mackenzie and R. W. Soukoreff. "Card, English, and Burr (1978) 25 Years Later." pages 760–761 (2003).
- [108] T. Sheridan and W. Ferrell. "Remote Manipulative Control with Transmission Delay." *IEEE Transactions on Human Factors in Electronics* **HFE-4**(1), 25–29. ISSN 0096-249X (1963).
- [109] W. R. Ferrell. "Remote manipulation with transmission delay." *IEEE Transactions on Human Factors in Electronics* **HFE-6**(1), 24–32. ISSN 0096-249X (1965).
- [110] J. Accot and S. Zhai. "Beyond Fitts' law." *Proceedings of the SIGCHI conference on Human factors in computing systems - CHI '97* pages 295–302. ACM Press, New York, New York, USA. ISBN 0897918029 (1997).
- [111] R. Pastel, J. Champlin, M. Harper, N. Paul, and W. Helton. "The Difficulty in Remotely Negotiating Corners." *Proceedings of the Human Factors and Ergonomics Society 51st Annual Meeting* (2007).
- [112] W. S. Helton, J. Head, and B. A. Blaschke. "Cornering Law: The Difficulty of Negotiating Corners With an Unmanned Ground Vehicle." *Human Factors: The Journal of the Human Factors and Ergonomics Society* **56**(2), 392–402. ISSN 0018-7208 (2014).

- [113] S. Vozar and D. M. Tilbury. “Driver Modeling for Teleoperation with Time Delay.” *19th IFAC World Congress* pages 3551–3556 (2014).
- [114] M. Souza. “IVS Integrated Vision System Operations Manual.” Technical report, Optech Incorporated (2012).
- [115] A. Howard, M. Turmon, L. Matthies, B. Tang, A. Angelova, and E. Mjolsness. “Towards learned traversability for robot navigation: From underfoot to the far field.” *Journal of Field Robotics* **23**(11-12), 1005–1017. ISSN 15564959 (2006).
- [116] Y. Brodsky, M. Cross, F. Carbognani, and E. Melotti. “Factors Affecting Human Performance as Rover Teleoperators.” *66th International Astronautical Congress* (2015).
- [117] B. S. Robinson, D. M. Boroson, D. Burianek, D. Murphy, F. Khatri, A. Biswas, Z. Sodnik, J. Burnside, J. Kansky, and D. M. Cornwell. “The NASA Lunar Laser Communication Demonstration Successful High-Rate Laser Communications To and From the Moon.” *13th International Conference on Space Operations 2014* American Institute of Aeronautics and Astronautics, Reston, Virginia. ISBN 978-1-62410-221-9 (2014).

Appendix A

Comparison of Classification Confusion Matrices

A.1 Vehicle Data Classification

A.1.1 Aggregate vs Loose Sand vs Compact Sand

Table A.1: Confusion matrix for Bayes classification of three bulk composition from vehicle data

	AGG	COM	LOO
AGG	90	26	4
COM	1	59	0
LOO	1	0	59

Table A.2: Confusion matrix for SVM classification of three bulk composition from vehicle data

	AGG	COM	LOO
AGG	120	0	0
COM	60	0	0
LOO	25	0	35

A.1.2 All 8 Classes

Table A.3: Confusion matrix for Bayes classification of all 8 terrain types from vehicle data

	CLA	DCS	DLS	GRA	PQU	WFS	WMS	WQU
CLA	26	0	0	0	1	2	0	1
DCS	0	29	0	0	0	1	0	0
DLS	0	0	30	0	0	0	0	0
GRA	1	1	0	12	2	0	0	14
PQU	1	1	0	0	27	0	0	1
WFS	0	5	0	0	0	24	0	1
WMS	0	0	0	0	0	0	30	0
WQU	4	0	0	0	0	0	0	26

Table A.4: Confusion matrix for SVM classification of all 8 terrain types from vehicle data

	CLA	DCS	DLS	GRA	PQU	WFS	WMS	WQU
CLA	21	0	0	0	3	3	0	3
DCS	0	29	0	0	0	1	0	0
DLS	0	0	30	0	0	0	0	0
GRA	9	7	2	2	2	1	1	6
PQU	4	7	0	0	15	3	0	1
WFS	1	15	0	0	0	13	0	1
WMS	0	0	2	0	0	0	28	0
WQU	10	0	2	0	0	3	0	15

A.2 Classification of Aggregate and Sand Using Wavelet Transformed Images

A.2.1 Naive Bayes Classification

Table A.5: Confusion matrix for Bayes classification of sand and aggregate types using transformed images

	AGG	SAN
AGG	395	5
SAN	31	369

Table A.6: Confusion matrix for Bayes classification of sand and aggregate types using lidar reflectance

	AGG	SAN
AGG	305	95
SAN	132	268

Table A.7: Confusion matrix for Bayes classification of sand and aggregate types using transformed images and lidar reflectance

	AGG	SAN
AGG	395	5
SAN	30	370

A.2.2 SVM Classification

Table A.8: Confusion matrix for SVM classification of sand and aggregate types using transformed images

	AGG	SAN
AGG	393	7
SAN	23	377

Table A.9: Confusion matrix for SVM classification of sand and aggregate types using lidar reflectance

	AGG	SAN
AGG	297	103
SAN	135	265

Table A.10: Confusion matrix for SVM classification of sand and aggregate types using transformed images and lidar reflectance

	AGG	SAN
AGG	393	7
SAN	6	394

A.3 Classification of Aggregate and Sand Using Image RGB Values

A.3.1 Naive Bayes Classification

Table A.11: Confusion matrix for Bayes classification of sand and aggregate types using transformed images

	AGG	SAN
AGG	102	298
SAN	100	300

Table A.12: Confusion matrix for Bayes classification of sand and aggregate types using transformed images and lidar reflectance

	AGG	SAN
AGG	320	80
SAN	76	324

A.3.2 SVM

Table A.13: Confusion matrix for SVM classification of sand and aggregate types using transformed images

	AGG	SAN
AGG	346	54
SAN	148	252

Table A.14: Confusion matrix for SVM classification of sand and aggregate types using transformed images and lidar reflectance

	AGG	SAN
AGG	349	51
SAN	138	262

A.4 Classification of Aggregate and Compact and Loose Sand Using Wavelet Transformed Images

A.4.1 Naive Bayes Classification

Table A.15: Confusion matrix for Bayes classification of three bulk composition using transformed images

	AGG	COM	LOO
AGG	394	0	6
SAN	0	200	0
LOO	15	97	88

Table A.16: Confusion matrix for Bayes classification of three bulk composition using lidar reflectance

	AGG	COM	LOO
AGG	290	4	106
SAN	46	101	53
LOO	88	39	73

Table A.17: Confusion matrix for Bayes classification of three bulk composition using transformed images and lidar reflectance

	AGG	COM	LOO
AGG	394	0	6
SAN	0	200	0
LOO	14	96	90

A.4.2 SVM Classification

Table A.18: Confusion matrix for SVM classification of three bulk composition using transformed images

	AGG	COM	LOO
AGG	394	0	6
SAN	0	200	0
LOO	15	100	85

Table A.19: Confusion matrix for SVM classification of three bulk composition using lidar reflectance

	AGG	COM	LOO
AGG	386	14	0
SAN	92	108	0
LOO	185	15	0

Table A.20: Confusion matrix for SVM classification of three bulk composition using transformed images and lidar reflectance

	AGG	COM	LOO
AGG	389	0	11
SAN	31	176	24
LOO	7	18	175

A.5 Classification of Aggregate and Compact and Loose Sand Using RGB

A.5.1 Naive Bayes Classification

Table A.21: Confusion matrix for Bayes classification of three bulk composition using RGB values

	AGG	COM	LOO
AGG	186	214	0
SAN	23	177	0
LOO	40	100	60

Table A.22: Confusion matrix for Bayes classification of three bulk composition using RGB values and lidar reflectance

	AGG	COM	LOO
AGG	333	49	18
SAN	9	182	9
LOO	69	20	111

A.5.2 SVM Classification

Table A.23: Confusion Matrix Images

	AGG	COM	LOO
AGG	392	8	0
SAN	71	129	0
LOO	111	89	0

Table A.24: Confusion Matrix Images + Lidar

	AGG	COM	LOO
AGG	371	0	29
SAN	0	196	4
LOO	124	6	70

A.6 Classification of Aggregates with Spectral Reflectance

A.6.1 Naive Bayes Classification

Table A.25: Confusion matrix for Bayes classification of aggregates using transformed images

	CLA	GRA	PQU	WQU
CLA	95	0	0	5
GRA	0	82	3	15
PQU	9	26	24	41
WQU	9	29	9	53

Table A.26: Confusion matrix for Bayes classification of aggregates using lidar reflectance

	CLA	GRA	PQU	WQU
CLA	74	4	16	6
GRA	8	81	3	8
PQU	7	2	91	0
WQU	13	24	1	62

Table A.27: Confusion matrix for Bayes classification of aggregates using spectral reflectance

	CLA	GRA	PQU	WQU
CLA	68	9	20	3
GRA	17	71	10	2
PQU	1	8	80	11
WQU	1	0	13	86

Table A.28: Confusion matrix for Bayes classification of aggregates using transformed images and lidar reflectance

	CLA	GRA	PQU	WQU
CLA	97	0	0	3
GRA	0	85	5	10
PQU	9	3	86	2
WQU	2	17	3	78

Table A.29: Confusion matrix for Bayes classification of aggregates using transformed images and spectral reflectance

	CLA	GRA	PQU	WQU
CLA	96	0	3	1
GRA	0	93	6	1
PQU	6	8	75	11
WQU	0	3	9	88

Table A.30: CConfusion matrix for Bayes classification of aggregates using lidar reflectance and spectral reflectance

	CLA	GRA	PQU	WQU
CLA	87	5	5	3
GRA	4	87	5	4
PQU	1	0	99	0
WQU	3	1	1	95

Table A.31: Confusion matrix for Bayes classification of aggregates using transformed images, lidar reflectance, and spectral reflectance

	CLA	GRA	PQU	WQU
CLA	99	0	0	1
GRA	0	95	4	1
PQU	5	3	99	1
WQU	0	4	3	93

A.6.2 SVM Classification

Table A.32: Confusion matrix for SVM classification of aggregates using transformed images

	CLA	GRA	PQU	WQU
CLA	83	0	0	17
GRA	0	72	3	25
PQU	8	49	11	32
WQU	5	34	3	58

Table A.33: Confusion matrix for SVM classification of aggregates using lidar reflectance

	CLA	GRA	PQU	WQU
CLA	79	4	13	4
GRA	8	72	3	17
PQU	10	4	86	0
WQU	12	15	1	72

Table A.34: Confusion matrix for SVM classification of aggregates using spectral reflectance

	CLA	GRA	PQU	WQU
CLA	13	14	26	47
GRA	25	37	19	19
PQU	7	8	80	13
WQU	3	0	18	79

Table A.35: Confusion matrix for SVM classification of aggregates using transformed images and lidar reflectance

	CLA	GRA	PQU	WQU
CLA	94	1	3	2
GRA	3	74	7	16
PQU	4	4	92	0
WQU	0	16	1	83

Table A.36: Confusion matrix for SVM classification of aggregates using transformed images and spectral reflectance

	CLA	GRA	PQU	WQU
CLA	96	0	3	1
GRA	0	93	6	1
PQU	6	8	75	11
WQU	0	3	9	88

Table A.37: Confusion matrix for SVM classification of aggregates using lidar reflectance and spectral reflectance

	CLA	GRA	PQU	WQU
CLA	73	15	10	2
GRA	8	86	2	4
PQU	2	2	96	0
WQU	1	1	0	98

Table A.38: Confusion matrix for SVM classification of aggregates using transformed images, lidar reflectance, and spectral reflectance

	CLA	GRA	PQU	WQU
CLA	76	20	3	1
GRA	5	85	4	6
PQU	3	6	91	1
WQU	0	5	0	95

A.7 Classification of Sands

A.7.1 Naive Bayes Classification

Table A.39: Confusion matrix for Bayes classification of sands using transformed images

	DCS	WFS	DLS	WMS
DCS	100	0	0	0
WFS	5	58	37	0
DLS	1	11	88	0
WMS	0	0	0	100

Table A.40: Confusion matrix for Bayes classification of aggregates using lidar reflectance

	DCS	WFS	DLS	WMS
DCS	57	0	15	28
WFS	0	100	0	0
DLS	17	0	77	6
WMS	12	0	0	88

Table A.41: Confusion matrix for Bayes classification of aggregates using transformed images and lidar reflectance

	DCS	WFS	DLS	WMS
DCS	100	0	0	0
WFS	0	100	0	0
DLS	1	0	99	0
WMS	0	0	0	100

A.7.2 SVM Classification

Table A.42: Confusion matrix for SVM classification of sands using transformed images

	DCS	WFS	DLS	WMS
DCS	91	9	0	0
WFS	0	23	77	0
DLS	0	8	92	0
WMS	0	0	0	100

Table A.43: Confusion matrix for SVM classification of aggregates using lidar reflectance

	DCS	WFS	DLS	WMS
DCS	70	0	15	15
WFS	0	100	0	0
DLS	20	0	78	2
WMS	24	0	0	76

Table A.44: Confusion matrix for SVM classification of aggregates using transformed images and lidar reflectance

	DCS	WFS	DLS	WMS
DCS	85	0	15	0
WFS	0	100	0	0
DLS	22	0	78	0
WMS	0	0	0	100

A.8 Classification all Eight Terrain Types

A.8.1 Naive Bayes Classification

Table A.45: Confusion matrix for Bayes classification of all 8 terrain types using transformed images

	CLA	DCS	DLS	GRA	PQU	WFS	WMS	WQU
CLA	95	0	0	0	0	0	0	5
DCS	0	100	0	0	0	0	0	0
DLS	0	1	88	0	0	11	0	0
GRA	0	0	0	81	3	0	1	15
PQU	9	0	0	26	13	0	11	41
WFS	0	5	37	0	0	58	0	0
WMS	0	0	0	11	1	0	88	0
WQU	9	0	0	29	6	0	3	53

Table A.46: Confusion matrix for Bayes classification of all 8 terrain types using lidar reflectance

	CLA	DCS	DLS	GRA	PQU	WFS	WMS	WQU
CLA	72	0	5	1	10	0	6	6
DCS	8	26	7	7	37	0	15	0
DLS	16	10	27	35	8	0	2	2
GRA	8	0	6	75	3	0	0	8
PQU	5	10	4	0	64	0	17	0
WFS	0	0	0	0	0	100	0	0
WMS	5	0	0	0	18	0	77	0
WQU	10	0	4	23	0	0	0	62

Table A.47: Confusion matrix for Bayes classification of all 8 terrain types using transformed images and lidar reflectance

	CLA	DCS	DLS	GRA	PQU	WFS	WMS	WQU
CLA	97	0	0	0	0	0	0	3
DCS	0	100	0	0	0	0	0	0
DLS	0	1	99	0	0	1	0	0
GRA	0	0	0	85	5	0	0	10
PQU	9	0	0	3	75	0	11	2
WFS	0	0	0	0	0	100	0	0
WMS	0	0	0	0	10	0	90	0
WQU	2	0	0	17	3	0	0	78

A.8.2 SVM

Table A.48: Confusion matrix for SVM classification of all 8 terrain types using transformed images

	CLA	DCS	DLS	GRA	PQU	WFS	WMS	WQU
CLA	83	0	0	0	0	0	0	17
DCS	0	94	0	0	0	6	0	0
DLS	0	0	92	0	0	8	0	0
GRA	0	0	0	72	3	0	0	25
PQU	8	0	0	42	11	0	7	32
WFS	0	2	77	0	0	21	0	0
WMS	0	0	0	19	0	0	81	0
WQU	5	0	0	33	3	0	1	58

Table A.49: Confusion matrix for SVM classification of all 8 terrain types using lidar reflectance

	CLA	DCS	DLS	GRA	PQU	WFS	WMS	WQU
CLA	76	0	6	0	12	0	2	4
DCS	9	31	7	6	37	0	10	0
DLS	16	9	31	31	9	0	1	3
GRA	8	0	12	60	3	0	0	17
PQU	6	12	9	0	66	0	7	0
WFS	0	0	0	0	0	100	0	0
WMS	5	0	0	0	29	0	66	0
WQU	10	0	6	11	1	0	0	72

Table A.50: Confusion matrix for SVM classification of all 8 terrain types using transformed images and lidar reflectance

	CLA	DCS	DLS	GRA	PQU	WFS	WMS	WQU
CLA	94	0	0	1	3	0	0	2
DCS	0	87	13	0	0	0	0	0
DLS	0	22	78	0	0	0	0	0
GRA	3	0	0	74	7	0	0	16
PQU	3	0	0	4	88	0	5	0
WFS	0	0	0	0	0	100	0	0
WMS	0	0	0	0	7	0	93	0
WQU	0	0	0	16	1	0	0	83

Appendix B

Results of Cornering

B.1 Lighting Conditions

Table B.1: Times, Errors and Scores for ambient lighting condition

Width (m)	0 s Delay			2 s Delay			4 s Delay		
	Time (s)	Error (%)	Score	Time (s)	Error (%)	Score	Time (s)	Error (%)	Score
0.85	37.0	56	0.34	74.4	53	0.39	108.4	54	0.45
0.95	29.8	28	0.19	61.4	36	0.28	80.2	26	0.26
1.05	26.5	7	0.08	60.6	0	0.10	82.4	15	0.21
1.15	27.7	7	0.08	56.9	7	0.13	73.7	10	0.17

B.2 Time Delay

Table B.2: Times, Errors and Scores for the spot light condition

	0 s Delay			2 s Delay			4 s Delay		
Width (m)	Time (s)	Error (%)	Score	Time (s)	Error (%)	Score	Time (s)	Error (%)	Score
0.85	34.9	52	0.32	78.5	58	0.42	98.1	54	0.43
0.95	27.8	21	0.15	61.6	28	0.24	83.5	23	0.25
1.05	29.3	7	0.08	62.0	13	0.17	86.2	18	0.23
1.15	27.8	7	0.08	52.2	3	0.10	72.7	0	0.12

Table B.3: Times, Errors and Scores for the dark condition

	0 s Delay			2 s Delay			4 s Delay		
Width (m)	Time (s)	Error (%)	Score	Time (s)	Error (%)	Score	Time (s)	Error (%)	Score
0.85	39.2	57	0.35	68.6	47	0.35	120.4	65	0.52
0.95	31.5	32	0.21	64.9	24	0.22	88.3	39	0.34
1.05	28.2	10	0.09	57.6	0	0.09	77.8	10	0.18
1.15	29.5	3	0.07	55.3	0	0.09	80.6	13	0.19

Table B.4: Times, Errors and Scores for 0 s time delay

	Ambient			Spot Light			Dark		
Width (m)	Time (s)	Error (%)	Score	Time (s)	Error (%)	Score	Time (s)	Error (%)	Score
0.85	37.0	56	0.34	35.0	52	0.32	39.2	57	0.35
0.95	29.8	28	0.18	27.8	21	0.15	31.5	32	0.21
1.05	26.5	7	0.08	29.3	7	0.08	28.2	10	0.09
1.15	27.7	7	0.08	27.8	7	0.08	29.5	3	0.07

Table B.5: Times, Errors and Scores for 2 s time delay

	Ambient			Spot Light			Dark		
Width (m)	Time (s)	Error (%)	Score	Time (s)	Error (%)	Score	Time (s)	Error (%)	Score
0.85	74.4	53	0.39	78.5	58	0.42	68.6	46	0.35
0.95	61.4	36	0.28	61.6	28	0.24	64.9	24	0.22
1.05	60.6	0	0.10	62.0	13	0.17	57.6	0	0.09
1.15	56.9	7	0.13	52.2	3	0.10	55.3	0	0.09

Table B.6: Times, Errors and Scores for 4 s time delay

	Ambient			Spot Light			Dark		
Width (m)	Time (s)	Error (%)	Score	Time (s)	Error (%)	Score	Time (s)	Error (%)	Score
0.85	108.4	54	0.45	98.1	54	0.43	120.4	65	0.52
0.95	80.2	26	0.26	83.5	23	0.25	88.3	39	0.34
1.05	82.4	15	0.21	86.2	18	0.23	77.8	10	0.18
1.15	73.7	10	0.17	72.7	0	0.12	80.6	13	0.19

B.3 Blocks

Table B.7: Block Scores for 0.85 cm at Ambient Lighting

Delay	Block 1			Block 2			Block 3			Block 4		
	Time (s)	Error (%)	Score	Time (s)	Error (%)	Score	Time (s)	Error (%)	Score	Time (s)	Error (%)	Score
0 s	48.2	80	0.48	34.6	30	0.21	31.2	40	0.25	29.3	62	0.36
2 s	142.5	81	0.64	59.4	55	0.37	60.4	22	0.21	53.5	36	0.27
4 s	109.2	67	0.51	129.9	45	0.44	100.0	54	0.43	70.4	45	0.34

Table B.8: Block Scores for 0.95 cm at Ambient Lighting

Delay	Block 1			Block 2			Block 3			Block 4		
	Time (s)	Error (%)	Score	Time (s)	Error (%)	Score	Time (s)	Error (%)	Score	Time (s)	Error (%)	Score
0 s	34.4	45	0.28	29.5	45	0.28	30.4	0	0.05	28.2	0	0.05
2 s	102.0	58	0.46	62.3	50	0.35	48.2	13	0.14	42.3	0	0.07
4 s	130.7	55	0.49	85.6	13	0.20	65.3	13	0.17	56.4	13	0.15

Table B.9: Block Scores for 1.05 cm at Ambient Lighting

	Block 1			Block 2			Block 3			Block 4		
Delay	Time (s)	Error (%)	Score	Time (s)	Error (%)	Score	Time (s)	Error (%)	Score	Time (s)	Error (%)	Score
0 s	28.1	22	0.16	29.7	0	0.05	25.2	0	0.04	23.2	0	0.04
2 s	84.9	0	0.14	64.5	0	0.11	47.1	0	0.08	46.0	0	0.08
4 s	132.6	30	0.37	80.1	22	0.24	62.5	0	0.10	54.4	0	0.09

Table B.10: Block Scores for 1.15 cm at Ambient Lighting

	Block 1			Block 2			Block 3			Block 4		
Delay	Time (s)	Error (%)	Score	Time (s)	Error (%)	Score	Time (s)	Error (%)	Score	Time (s)	Error (%)	Score
0 s	29.1	22	0.16	27.9	0	0.05	25.9	0	0.04	28.0	0	0.05
2 s	71.7	22	0.23	58.2	0	0.10	50.1	0	0.08	47.6	0	0.08
4 s	105.0	14	0.24	77.8	13	0.19	55.9	0	0.09	56.0	13	0.15

Table B.11: Block Scores for 0.85 cm with Bright Spot Light

	Block 1			Block 2			Block 3			Block 4		
Delay	Time (s)	Error (%)	Score	Time (s)	Error (%)	Score	Time (s)	Error (%)	Score	Time (s)	Error (%)	Score
0 s	47.3	77	0.46	35.8	45	0.29	28.3	40	0.25	28.1	40	0.25
2 s	139.1	82	0.64	67.4	50	0.36	68.7	45	0.34	54.9	45	0.32
4 s	157.1	76	0.64	94.5	54	0.42	90.5	50	0.40	77.6	13	0.19

Table B.12: Block Scores for 0.95 cm with Bright Spot Light

Delay	Block 1			Block 2			Block 3			Block 4		
	Time (s)	Error (%)	Score	Time (s)	Error (%)	Score	Time (s)	Error (%)	Score	Time (s)	Error (%)	Score
0 s	31.8	50	0.30	28.6	0	0.05	27.1	13	0.11	25.7	0	0.04
2 s	102.1	62	0.47	63.7	22	0.22	48.3	0	0.08	41.7	0	0.07
4 s	123.8	22	0.32	83.4	33	0.30	67.7	22	0.22	60.9	13	0.16

Table B.13: Block Scores for 1.05 cm with Bright Spot Light

Delay	Block 1			Block 2			Block 3			Block 4		
	Time (s)	Error (%)	Score	Time (s)	Error (%)	Score	Time (s)	Error (%)	Score	Time (s)	Error (%)	Score
0 s	34.1	13	0.12	30.3	13	0.11	26.1	0	0.04	26.9	0	0.04
2 s	94.0	33	0.32	64.1	13	0.17	47.4	0	0.08	42.6	0	0.07
4 s	119.0	22	0.31	105.7	40	0.37	69.8	0	0.11	57.2	0	0.09

Table B.14: Block Scores for 1.15 cm with Bright Spot Light

Delay	Block 1			Block 2			Block 3			Block 4		
	Time (s)	Error (%)	Score	Time (s)	Error (%)	Score	Time (s)	Error (%)	Score	Time (s)	Error (%)	Score
0 s	33.1	22	0.17	28.2	0	0.05	26.7	0	0.04	23.0	0	0.04
2 s	72.2	13	0.18	53.1	0	0.09	42.6	0	0.07	40.8	0	0.07
4 s	101.3	0	0.17	70.3	0	0.12	64.2	0	0.11	54.9	0	0.09

Table B.15: Block Scores for 0.85 cm in Darkness

Delay	Block 1			Block 2			Block 3			Block 4		
	Time (s)	Error (%)	Score	Time (s)	Error (%)	Score	Time (s)	Error (%)	Score	Time (s)	Error (%)	Score
0 s	69.6	86	0.54	34.4	0	0.06	33.3	36	0.24	28.1	58	0.34
2 s	120.2	78	0.59	74.0	45	0.35	60.7	13	0.16	45.8	13	0.14
4 s	236.5	89	0.83	88.2	42	0.35	84.4	64	0.46	89.8	55	0.42

Table B.16: Block Scores for 0.95 cm in Darkness

Delay	Block 1			Block 2			Block 3			Block 4		
	Time (s)	Error (%)	Score	Time (s)	Error (%)	Score	Time (s)	Error (%)	Score	Time (s)	Error (%)	Score
0 s	38.5	62	0.37	37.9	33	0.23	26.8	0	0.04	26.2	13	0.11
2 s	93.7	40	0.35	60.1	33	0.27	60.6	13	0.16	46.2	0	0.08
4 s	161.0	71	0.62	93.6	36	0.33	87.0	13	0.20	54.8	13	0.15

Table B.17: Block Scores for 1.05 cm in Darkness

Delay	Block 1			Block 2			Block 3			Block 4		
	Time (s)	Error (%)	Score	Time (s)	Error (%)	Score	Time (s)	Error (%)	Score	Time (s)	Error (%)	Score
0 s	30.3	13	0.11	30.7	0	0.05	26.5	22	0.15	25.2	0	0.04
2 s	77.8	0	0.13	60.7	0	0.10	48.5	0	0.08	43.4	0	0.07
4 s	107.7	30	0.33	86.5	0	0.14	61.5	0	0.10	55.6	0	0.09

Table B.18: Block Scores for 1.15 cm in Darkness

Delay	Block 1			Block 2			Block 3			Block 4		
	Time (s)	Error (%)	Score	Time (s)	Error (%)	Score	Time (s)	Error (%)	Score	Time (s)	Error (%)	Score
0 s	34.1	13	0.12	31.2	0	0.05	27.8	0	0.05	25.0	0	0.04
2 s	78.4	0	0.13	57.1	0	0.09	44.3	0	0.07	41.5	0	0.07
4 s	133.7	13	0.28	80.9	13	0.19	54.6	13	0.15	53.0	13	0.15

Curriculum Vitae

Matthew Dennis George Cross

Post-Secondary Education and Degrees:

University of Western Ontario	2012 - 2016
Ph.D. (Electrical and Computer Engineering)	London, Canada
Carleton University	2010 - 2012
M.A.Sc (Aerospace Engineering)	Ottawa, Canada
Carleton University	2004 - 2006
M.Eng (Aerospace Engineering)	Ottawa, Canada
Carleton University	2000 - 2004
B.Eng (Aerospace Engineering)	Ottawa, Canada

Honours and Awards:

NSERC PGS D	2014 - 2016
NSERC-CREATE	2012 - 2014
	2016
Lunar and Planetary Institute Career Development Award	2016
AER Global Opportunities Award for Environment and Sustainability	2015
Studies	
Ontario Graduate Policy Research Challenge Award	2014
CIFAR Astrobiology Summer School Scholar	2012
CSA Class Grant	2011 + 2012

Related Work Experience:

Limited Duties Instructor	2016
University of Western Ontario	
Teaching Assistant	2013 - 2015
University of Western Ontario	
REALM Mechatronics Developer	2013 - 2015
University of Western Ontario	
Teaching Assistant	2010 - 2012
Carleton University	
Space Systems Engineer	2007 - 2009
European Space Agency	

Publications:

Cross, M., Battler, M., Maiwald, V., Van't Woud, H., Schlacht, I., Ono, A., Orgel, C., Foing, B. H., McIsaac, K. "Operational Lessons Learnt from the 2013 ILEWG EuroMoonMars-B Analogue Campaign for Future Habitat Operations on Moon and Mars." *Acta Futura* DOI: 10.5281/zenodo.202179 (2016).

Cross, M., Ellery, A., Qadi, A. "Estimating Terrain Parameters for a Rigid Wheeled Rover Using Neural Networks." *Journal of Terramechanics* DOI:10.1016/j.jterra.2013.04.002 (2013).

Cross, M., Nicol, C., Qadi, A., Ellery, A. "Application of COTS Components for Martian Surface Exploration." *Journal of the British Interplanetary Society* 2013.66.161 (2013).

Walker, R., **Cross, M.** "The European Student Moon Orbiter (ESMO): A lunar mission for education, outreach and science." *Acta Astronautica* 66 (7-8) p. 1177-1188 DOI: 10.1016/j.actaastro.2009.10.008 (2010).